The scientific legacy of NASA's Operation IceBridge

NASA Operation IceBridge Project Science Office, Science and Instrument Teams *

* Joseph A. MacGregor [1†], Linette N. Boisvert [1], Brooke Medley [1], Alek A. Petty [1,2], Jeremy P. Harbeck [1,3], Robin E. Bell [4], J. Bryan Blair [5], Edward Blanchard-Wrigglesworth [6], Ellen M. Buckley [7], Michael S. Christoffersen [8], James. R. Cochran [4], Beáta M. Csathó [9], Eugenia L. De Marco [10,11], RoseAnne T. Dominguez [12], Mark A. Fahnestock [13], Sinéad L. Farrell [14], S. Prasad Gogineni [15], Jamin S. Greenbaum [16], Christy M. Hansen [17], Michelle A. Hofton [5,14], John W. Holt [8], Kenneth C. Jezek [18], Lora S. Koenig [19], Nathan T. Kurtz [1], Ronald Kwok [20], Christopher F. Larsen [13], Carlton J. Leuschen [21], Caitlin D. Locke [4], Serdar S. Manizade [1,22], Seelye Martin [23], Thomas A. Neumann [1], Sophie M.J. Nowicki [9], John D. Paden [21], Jacqueline A. Richter-Menge [24], Eric J. Rignot [20,25], Fernando Rodríguez-Morales [21], Matthew R. Siegfried [26], Benjamin E. Smith [27], John G. Sonntag [1,28], Michael Studinger [1], Kirsty J. Tinto [4], Martin Truffer [13], Thomas P. Wagner [29], John E. Woods [30], Duncan A. Young [31] and James K. Yungel [1,22]

[1] Cryospheric Sciences Laboratory (Code 615), NASA Goddard Space Flight Center, Greenbelt, MD, USA
[2] Earth System Science Interdisciplinary Center, University of Maryland, College Park, MD, USA
[3] ADNET Systems, Bethesda, MD, USA
[4] Lamont-Doherty Earth Observatory, Columbia University, Palisades, NY, USA
[5] Geodesy and Geophysics Laboratory (Code 61A), NASA Goddard Space Flight Center, Greenbelt, MD, USA
[6] Dept. of Atmospheric Sciences, University of Washington, Seattle, WA, USA
[7] Dept. of Atmospheric and Oceanic Science, University of Maryland, College Park, MD, USA
[8] Lunar and Planetary Laboratory, The University of Arizona, Tucson, AZ, USA
[9] Dept. of Geology, University at Buffalo, Buffalo, NY, USA
[10] Electro-mechanical Systems Branch (Code 544), NASA Goddard Space Flight Center, Greenbelt, MD, USA
[11] ATA Aerospace, Greenbelt, MD, USA
[12] Universities Space Research Association, NASA Ames Research Center, Moffett Field, CA, USA
[13] Geophysical Institute, University of Alaska Fairbanks, Fairbanks, AK, USA
[14] Dept. of Geographical Sciences, University of Maryland, College Park, MD, USA
[15] Dept. of Electrical and Computer Engineering, The University of Alabama, Tuscaloosa, AB, USA
[16] Scripps Institution of Oceanography, University of California, San Diego, La Jolla, USA
[17] Flight Projects Directorate (Code 400), NASA Goddard Space Flight Center, Greenbelt, MD, USA
[18] Byrd Polar Research Center, The Ohio State University, Columbus, OH, USA
[19] National Snow and Ice Data Center, Cooperative Institute for Research in Environmental Sciences, University of Colorado, Boulder, CO, USA
[20] Jet Propulsion Laboratory, California Institute of Technology, Pasadena, CA, USA
[21] Center for Remote Sensing of Ice Sheets, The University of Kansas, Lawrence, KS, USA
[22] Amentum, NASA Wallops Flight Facility, Wallops Island, VA, USA
[23] School of Oceanography, University of Washington, Seattle, WA, USA
[24] University of Alaska Fairbanks, Fairbanks, AK, USA
[25] Dept. of Earth System Science, University of California, Irvine, CA, USA
[26] Dept. of Geophysics, Colorado School of Mines, Golden, CO, USA
[27] Applied Physics Laboratory, University of Washington, Seattle, WA, USA
[28] Bay Area Environmental Research Institute, Moffett Field, CA, USA
[29] Science Mission Directorate, NASA Headquarters, Washington, DC, USA

[30] Office of Naval Research, Washington, DC, USA
[31] Institute for Geophysics, The University of Texas at Austin, TX, USA
† Corresponding author: joseph.a.macgregor@nasa.gov.

Abstract

NASA's Operation IceBridge (OIB) was a twelve-year (2009–2020) airborne mission to survey land and sea ice across the Arctic, Antarctic and Alaska. Here we review OIB's goals, instruments, campaigns, key scientific results and implications for future investigations of the cryosphere. OIB's primary goal was to use airborne laser altimetry to bridge the gap in fine-resolution elevation measurements of ice from space between the conclusion of NASA's Ice, Cloud, and land Elevation Satellite (ICESat; 2003–2009) and its follow-on, ICESat-2 (launched 2018). Additional scientific requirements were intended to contextualize observed elevation changes using a multi-sensor suite of radar sounders, gravimeters, magnetometers, and cameras. Using 15 different aircraft, OIB conducted 958 science flights, of which 41% were repeat surveys of land ice, 42% were surveys of previously unmapped terrain across the Greenland and Antarctic ice sheets, Arctic ice caps and Alaskan glaciers, and 17% were surveys of sea ice. The combination of an expansive instrument suite and breadth of surveys enabled numerous fundamental advances in our understanding of the Earth's cryosphere. For land ice, OIB dramatically improved knowledge of interannual outlet-glacier variability, ice-sheet and outlet-glacier thicknesses, snowfall rates on ice sheets, fjord and sub-ice-shelf bathymetry, and ice-sheet hydrology. Unanticipated discoveries included a reliable method for constraining the thickness within difficult-to-sound incised troughs beneath ice sheets, the extent of the firn aquifer within the Greenland Ice Sheet, the vulnerability of many Greenland and Antarctic outlet glaciers to ocean-driven melting at their grounding zones, and the dominance of surface-melt-driven mass loss of Alaskan glaciers. For sea ice, OIB significantly advanced our understanding of spatiotemporal variability in sea ice freeboard and its snow cover, especially through combined analysis of fine-resolution altimetry, visible imagery, and snow radar measurements of the overlying snow thickness. Such analyses led to the unanticipated discovery of an interdecadal decrease in snow thickness on Arctic sea ice and numerous opportunities to validate sea ice freeboards from satellite radar altimetry. While many of its datasets have yet to be fully explored, OIB's scientific legacy has already demonstrated the value of sustained investment in reliable airborne platforms, airborne instrument development, interagency and international collaboration, and open and rapid data access to advance our understanding of Earth's remote polar regions and their role in the Earth system.

Key points

1. NASA's Operation IceBridge surveyed fast-changing and poorly mapped regions of the polar cryosphere at unprecedented resolution.
2. Along with mapping surface-elevation change of the cryosphere, additional mission data enabled a variety of unanticipated discoveries.
3. Future polar airborne missions should seek multi-disciplinary synergies between target regions, instruments, and scientific priorities.

Table of contents

1. Introduction

The impact of global climate change on the polar cryosphere was noted as early as the 1980s but quantifying these changes and their connections to climate drivers was challenging (Arctic Climate Impact Assessment, 2004). In the 1970s, satellite photogrammetry and passive-microwave studies proved useful for mapping polar ice extent but lacked sufficient resolution to characterize the cryptic changes that were occurring. Airborne laser altimetry was developed as a research tool in the late 20th century, and by the late 1980s such instruments could achieve the sub-meter precision needed to reliably detect change in polar ice elevation (Krabill et al., 1995). In 1993, the United States' (US) National Aeronautics and Space Administration (NASA) began the first of an ambitious series of annual airborne campaigns to survey the changing elevation of Arctic land ice using laser altimetry, called Arctic Ice Mapping (AIM) (see Glossary for a list of acronyms). AIM was one component of NASA's Program for Arctic Regional Climate Assessment (PARCA), which advanced the study of changes in the mass balance of the Greenland Ice Sheet through airborne, satellite, and *in situ* observations (Thomas, 2001). The goal of AIM was to measure Greenland Ice Sheet elevation across its major drainage basins, then to t repeat these surveys five years later. These campaigns established that the Greenland Ice Sheet was losing mass (Krabill et al., 2000), but that this pattern contained significant spatial variability that was challenging to resolve from aircraft alone. Annual campaigns continued through 2008 in the Arctic and beyond, refining measurement and operational techniques for polar airborne surveys, and facilitating international collaborations (e.g., Thomas et al., 2004) and sea ice surveys, e.g., the Laser Radar Altimetry campaign in 2002 (Giles et al., 2007). These campaigns established that multi-instrument aircraft were an essential tool for validating satellite measurements while also collecting ancillary measurements of both contextual and broader geophysical value.

Radar altimetry studies of ice height and motion enabled by European Space Agency (ESA) satellites in the early-to-mid 1990s also pointed to the need for finer-precision altimetry of the polar regions (e.g., Wingham et al., 1998; Kwok et al., 1998). Combined with results from airborne surveys, these discoveries provided part of the rationale for the development and launch of the first terrestrial satellite laser altimeter, NASA's Ice, Cloud, and land Elevation Satellite (ICESat; launched 2003; Schutz et al., 2005). However, problems with ICESat's primary instrument, the Geoscience Laser Altimeter System (GLAS), limited data acquisition to short, seasonal campaigns (Abshire et al., 2005; Webb et al., 2013). Even with the unexpected performance shortfall of GLAS, analysis of ICESat observations firmly established that peripheral thinning was continuing across the Greenland and Antarctic ice sheets and that Arctic sea ice was thinning rapidly (Pritchard et al., 2009; Kwok and Rothrock, 2009). Concurrent observations also indicated increasing and non-linear loss of ice from the Arctic: satellite-gravity observations suggested an acceleration of Greenland Ice Sheet mass loss (Velicogna and Wahr, 2006) and satellite passive microwave analysis revealed a record-shattering retreat of Arctic sea ice in 2007 (Comiso et al., 2008). Key Antarctic and Alaskan glaciers were also thinning rapidly, as documented by airborne laser altimetry (Arendt et al., 2002; Thomas et al., 2004).

Consequently, the National Research Council's 2007–2017 Decadal Survey for Earth Science and Applications from Space recommended continuing ICESat's measurements in the form of ICESat-2 as a first-tier priority (Markus et al., 2017). With ICESat expected to fail before the planned ICESat-2 mission could be developed and launched, NASA investigated options for a gap-filler mission. Two potential satellite missions were considered: "ICESat-Lite", a copy of ICESat apart from repairs to GLAS, and "QuickIce", a commercial system with performance and capabilities similar to ICESat (http://www.spaceref.com/news/viewsr.html?pid=29795). In parallel, NASA considered the potential for an airborne gap-filler mission by developing flight plans and assessing available instruments. It was soon realized that ICESat-Lite and QuickIce would be both expensive and take too long to develop, whereas an airborne mission could more cost-effectively extend altimetry time series over the most critical areas of the Arctic, Antarctic and Alaska, so NASA pivoted to the latter option. These airborne campaigns ultimately became known as Operation IceBridge (OIB; Koenig et al., 2010), NASA's longest-running and most ambitious airborne mission yet, representing a total NASA investment of $181M (inflation-adjusted 2020 U.S. dollars). OIB evolved into the largest scientific airborne survey of Earth's polar regions ever undertaken, rivaling even the pioneering Operation Highjump (1946–1947; Bertrand, 1967) and NSF/SPRI/TUD campaigns (1967–1979; Robin et al., 1977; Schroeder et al., 2019), which first surveyed the Antarctic coastline and interior extensively.

Between 2009 and 2020, OIB's core campaigns included multi-week to multi-month annual boreal springtime surveys of the Arctic (Greenland Ice Sheet; Arctic ice caps; Arctic Ocean; Alaska) and austral springtime surveys of the Antarctic (Antarctic Ice Sheet; Southern Ocean), with additional regular summer/fall campaigns in Alaska and occasional ones elsewhere in the Arctic. To fulfill the mission's core scientific requirement of monitoring elevation change, several airborne laser altimeters were used in targeted campaigns on multiple platforms. These campaigns prioritized repeat surveys along identical tracks, often coincident with legacy ICESat tracks, future ICESat-2 tracks and even contemporaneous ones once ICESat-2 launched in September 2018 (Neumann et al., 2019). OIB also collaborated with multiple other USA government agencies, along with academic and international partners to survey ground stations and field sites of interest, as well as concurrent ground tracks of multiple ESA satellite and airborne missions for calibration/validation purposes.

Early in the formulation of OIB, NASA decided that – in addition to laser altimetry – deployed aircraft should also be fully exploited to make ancillary measurements relevant to cryospheric sciences, consistent with the successful antecedent NASA experience from AIM and PARCA. During most campaigns, OIB also deployed multiple radar sounders, gravimeters, magnetometers, and visible, infrared and hyperspectral cameras on a variety of aircraft to measure additional surface and subsurface geophysical properties that better contextualized the observed elevation change. In doing so, OIB continued records of elevation change across some of the vulnerable portions of the cryosphere, addressed large gaps in our understanding of several important land and sea ice processes and properties, and enabled numerous unanticipated discoveries regarding Earth's remote polar regions.

This article reviews and synthesizes the key outcomes of OIB as understood by the scientists and engineers who led the design of the mission, its scientific rationale, data collection and campaign operations. As background, we summarize the mission's scientific requirements, the instruments deployed, and the nature of its 12 years of operations. As of March 2021, OIB datasets have formed part of the basis of over 660 scientific articles (https://nsidc.org/data/icebridge/research.html; 63% focused on land ice, and 37% on sea ice) – well beyond the scope of any single review article to fully recount. Instead, here we describe key scientific results relative to the mission's scientific requirements and highlight significant discoveries. Finally, we assess what made OIB successful and what key gaps remain in our understanding of Earth's cryosphere, so as to inform the design of future polar airborne and satellite missions.

2. Science requirements

OIB was established rapidly in 2009, as ICESat's final lasers failed. Initially, OIB consisted of a NASA-directed Project Science Office (PSO) at NASA's Goddard Space Flight Center to lead campaigns onboard the NASA P-3, an instrument suite that was selected competitively via a standard NASA Research

Announcement, and two additional stand-alone campaigns led by University of Alaska Fairbanks (UAF) and The University of Texas' Institute for Geophysics (UTIG). It was initially unclear how long the mission would be maintained or what its budget would be. Initial estimates were <5 yr and part of its budget came from the American Recovery and Reinvestment Act of 2009, which ultimately set OIB's budget at ~$15M per year.

A consequence of this unusual inception was that OIB's measurement requirements were first set by the competed instrument teams, with survey priorities determined by *ad hoc* committees convened by NASA. These committees consisted of active polar cryosphere researchers and satellite remote-sensing experts supported by NASA, the National Oceanic and Atmospheric Administration (NOAA) and the Department of Defense, along with senior members of the instrument teams. In 2010, two formal Science Teams (STs) were established, one for land ice and another for sea ice. These teams and the PSO ultimately formalized the science requirements in 2013 in a manner akin to NASA spaceflight missions. These science requirements defined the measurements necessary for the mission to achieve its science goals and objectives (Appendix A), which flow down from programmatic goals (Table A1) to more specific scientific goals (Table A2), questions (Table A3), and dataset requirements. As appropriate, these elements were divided between those relevant to sea ice and land ice, which was divided between ice sheets and glaciers/ice caps. A revised version of this sequence was approved in 2018, which reflected adjustments needed in light of logistical and budget limitations, highlighted by a 2014 external review. Instruments and the ST continued to be competitively selected on three- year cycles, but to retain continuity the PSO remained a directed function.

OIB's "baseline" science requirements included well-established measurements of geophysical parameters that are essential to characterize cryospheric change, e.g., repeat measurement of ice surface elevation, elevation change, ice thickness, snow accumulation, subglacial topography, snow thickness on sea ice, and bathymetry near outlet glaciers and beneath ice shelves (Tables 1–3). These requirements considered geographic objectives that were demonstrably within reach of human-occupied aircraft within the time frames consistent with previous airborne surveys of the polar regions (e.g., Krabill et al., 2000; Thomas et al., 2004). Measurement accuracy and specific geographic targets were formulated using the ST's knowledge base, available scientific studies and consensus reports at the time. Quoted measurement accuracies represent uncertainties of one standard deviation about the mean.

Table 1: Baseline – ice sheets

OIB baseline science requirements for ice sheets.

#	**Baseline science requirements for ice sheets**
IS1	Measure surface elevation with a vertical accuracy of 10 cm.
IS2	Measure annual changes in ice sheet surface elevation with sufficient accuracy to detect 15 cm changes in un-crevassed and 100 cm changes in crevassed regions along sampled profiles over distances of 500 m.
IS3	Measure ice thickness with an accuracy of 50 m or 10% of the ice thickness, whichever is greater.
IS4	Measure free air gravity anomalies to an accuracy of 0.5 mGal and at the shortest length scale allowed by the aircraft.
IS5	Acquire sub-meter resolution, stereo color imagery covering laser altimetry swaths.
IS6	Measure repeat Antarctic and Greenland surface elevation profiles along established airborne altimetry and ICESat/ICESat-2 ground tracks, and in support of other altimetry missions (CryoSat-2, Sentinel-3).
IS7	Measure ice thickness in Greenland and Antarctica to support interpretation of the ICESat, OIB and ICESat-2 elevation records, the NISAR mission, and other cryospheric objectives.
IS8	Measure surface elevation along central flowlines of outlet glaciers constraining 80% of the ice

	discharge from the Greenland Ice Sheet.
IS9	Measure cross-transects of ice thickness, surface, and bed elevation upstream of the terminus of glaciers constraining 80% of the ice discharge from the Greenland Ice Sheet.
IS10	Measure cross-transects of ice thickness, surface elevation, gravity anomalies upstream of the grounding line of select Antarctic glaciers.
IS11	Measure surface elevation, ice thickness and sea floor bathymetry beneath select Antarctic ice shelves, adjacent continental shelves, and along select Greenland fjords.
IS12	Acquire near-surface radar data to document spatial patterns of snow accumulation with a vertical resolution of 10 cm or better.
IS13	Acquire radar-sounding data to measure changes in ice-shelf thickness with a precision of 5 m or better per time interval along select ice shelves in Antarctica and floating ice tongues in Greenland.
IS14	Collect seasonal changes (spring vs. fall) in surface elevation in Greenland to detect 15 cm changes in un-crevassed areas and 100 cm changes in crevassed regions along sampled profiles over distances of 500 m.

Table 2: Baseline – glaciers and ice caps

OIB baseline science requirements for glaciers and ice caps.

#	**Baseline science requirement for glaciers and ice caps**
IC1	Annually to semi-annually collect laser altimetry swath data along the centerlines of major Gulf of Alaska glacier and icefield systems, repeating previous ICESat measurements and airborne laser altimetry centerline profiles.
IC2	Make annual repeat measurement of surface elevation on select Alaskan glaciers.
IC3	Make ice elevation, ice thickness and gravity measurements on Canadian Arctic ice caps at least twice during OIB. Coverage should be based on previous airborne campaigns and in support of CryoSat-2 *in situ* validation activities.
IC4	Make ice elevation, ice thickness and gravity measurements on selected ice caps and alpine glaciers around the Greenland Ice Sheet. Repeat the elevation measurements at least once during OIB.

Table 3: Baseline – sea ice

OIB baseline science requirements for sea ice.

#	**Baseline requirements for sea ice**
SI1	Make surface elevation measurements of the water, ice or snow with a shot-to-shot independent error of less than 10 cm and correlated errors that contribute less than 1 cm to the mean height error in either sea surface or sea ice elevation. The spot size should be 1 m or less and spaced at 3 m or less.
SI2	Make elevation measurements of both the air–snow and the snow–ice interfaces to an uncertainty of 3 cm, which enables the determination of snow thickness to an uncertainty of 5 cm.
SI3	Provide annual acquisitions of sea ice surface elevation in the Arctic and Southern Oceans during the late winter along near-exact repeat tracks in regions of the ice pack that are undergoing rapid change. Flight lines shall be designed to ensure measurements are acquired across a range of ice types including seasonal (first-year) and perennial (multi-year) sea ice to include, as a minimum: *Arctic* 1. At least two transects to capture the thickness gradient across the perennial and seasonal ice covers between Greenland, the central Arctic, and the Alaskan Coast. 2. The perennial sea ice pack from the coasts of Ellesmere Island and Greenland north to the pole and westward across the northern Beaufort Sea.

	3. Sea ice across the Fram Strait and Nares Strait flux gates. 4. The sea ice cover of the Eastern Arctic, north of the Fram Strait. *Antarctic* 1. Sea ice in the Weddell Sea between the tip of the Antarctic Peninsula and Cape Norvegia. 2. Mixed ice cover in the western Weddell Sea between the tip of Antarctic Peninsula and Ronne Ice Shelf. 3. The ice pack of the Bellingshausen and Amundsen Seas.
SI4	Include flight lines for sampling the ground tracks of satellite laser altimeters (ICESat and ICESat-2) and radars (CryoSat-2 and Sentinel-3). In the case of CryoSat-2, both OIB and CryoSat-2 ground tracks should be temporally and spatially coincident whenever possible. At least one ground track of each satellite should be sampled per campaign.
SI5	Conduct sea ice flights as early as possible in the spring flight sequence of each campaign, prior to melt onset.
SI6	Collect coincident natural color visible imagery of sea ice conditions at a spatial resolution of at least 10 cm per pixel to enable direct interpretation of the altimetry data.
SI7	Conduct sea ice flights primarily in cloud-free conditions. However, data shall be retained under all atmospheric conditions with a flag included to indicate degradation or loss of data due to clouds.
SI8	Make full gravity vector measurements on non-repeat, low-elevation (< 1000 m) flights over sea ice to enable the determination of short-wavelength (order 10 to 100 km) geoid fluctuations along the flight track to a precision of 2 cm.
SI9	Make available to the community instrument data on sea ice surface elevation and snow thickness within 3 months of acquisition and derived products within six months of data acquisition.

These science requirements were referred to regularly by the ST when designing OIB surveys and remained key reference points for prioritization of individual surveys throughout the mission. The ST met biannually (once each for the upcoming core Arctic and Antarctic campaigns) to refine and prioritize survey designs that met or exceeded the science requirements by the end of either the individual campaign or the overall mission, depending on the requirement. The ST also solicited and considered inputs from the broader science community when determining these priorities. The ST identified a core set of surveys as "baseline" that OIB strived to repeat each year to provide altimetry time series of observations in key regions, with other surveys as high-, medium-, or low-priority depending on their overall potential contribution to OIB science goals. This prioritization balanced core requirements, typically involving altimetry, versus those that prioritized other measurements. The collective knowledge base of both the instrument and science teams, spanning several decades, was another important contributor in designing, planning and managing a responsive but feasible set of ~30–50 potential flights in each hemisphere each year. These sets were purposefully larger than the number of available flights, so that the field team would not run out of options while undertaking the campaign amid multiple operational constraints (mainly weather). For any given flight day, the list of possible surveys was first constrained by regional weather (favoring clear skies for both flight safety and laser altimetry) and often other logistical constraints, which whittled feasible surveys to a handful from which the highest priority mission was typically selected. Operational weather observations and forecasting in the polar regions improved substantially during OIB, such that only a handful of flights were substantially hindered by on-site weather. Rare, aborted flights were almost entirely due to aircraft mechanical issues.

In addition to its physically based science requirements, OIB implemented a data management plan consistent with NASA standards. Within six months of the conclusion of each OIB campaign, all data collected were intended to be processed by the instrument teams and then delivered to and released by the National Snow and Ice Data Center (NSIDC), a publicly accessible NASA Distributed Active Archive

Center. There was no period of exclusive access for any investigator or ST member. This policy constituted a substantial departure from many previous polar airborne campaigns, particularly in the Antarctic, which traditionally applied a multi-year period of exclusive access to collected data.

3. Instruments

In this section, we describe the instruments employed by OIB to survey polar ice and meet the mission's overall objectives. We focus on their measurement characteristics, accuracy and precision, and evolution over the course of OIB.

3.1. Laser altimeters

Laser altimeters were fundamental to achieving many of OIB's science requirements (Tables 1–3; Figure 1). The elevation data these instruments collected were the primary rationale for the majority of the surveys during any given campaign and in many cases the only rationale, depending on the instrument suite deployed. Hence, instrument calibration, validation, maximum range, cost and reliability were critical in their selection for OIB. Multiple versions of four different laser altimeters were deployed to meet the constraints of individual campaigns. Most OIB campaigns surveyed at a relatively low nominal elevation above ground level (AGL) of ~460 m (1,500 ft), so the maximum range of the laser altimeter was not an issue and multiple altimeters were suitable. For campaigns that only deployed a laser altimeter from high altitudes (>10,000 ft AGL), Only the LVIS instrument had sufficient ranging capabilities for those altitudes.

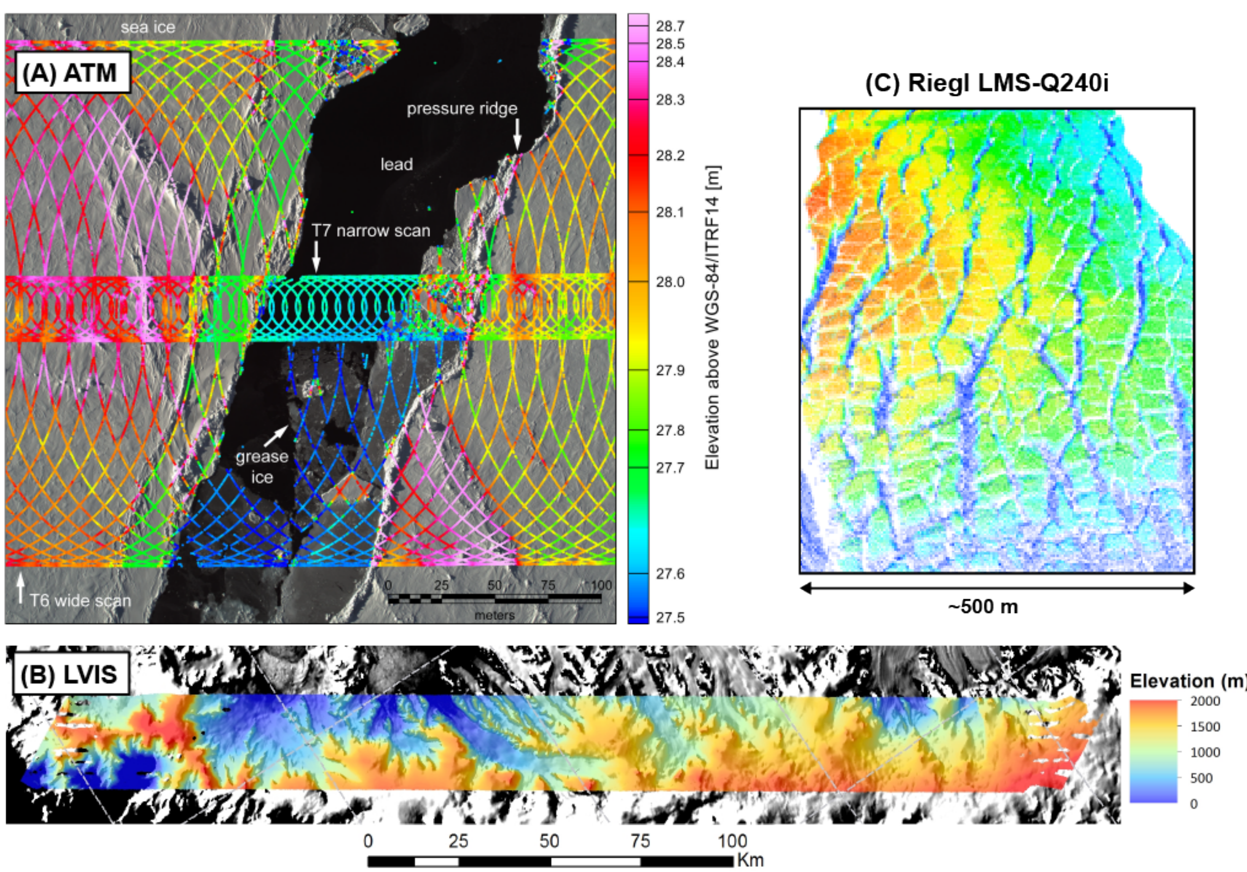

Figure 1: Laser altimeters

Example OIB laser altimetry data. (A) 2019 ATM T-6 and T-7 swaths over Arctic sea ice, overlain on a CAMBOT v2 image. (B) 2009 LVIS v1 data across the Antarctic Peninsula, comprising 16, 2.4-km-wide swaths. (C) 2009 Riegl LMS-Q240i data over a crevasse field on Malaspina Glacier, Alaska.

3.1.1. Airborne Topographic Mapper (ATM)

The ATM instrument suite has a legacy that dates to early research in the 1970s on laser altimeter designs and applications. ATM has been surveying terrestrial topography for several decades, with a primary focus on the cryosphere since 1993 (Krabill et al., 1995). As part of AIM and PARCA, ATM was deployed to conduct annual surveys of the Arctic cryosphere between 1993–2008 and occasional surveys of the Antarctic. Results from these surveys directly informed the scientific and operational rationale for OIB, including observations of peripheral ice-sheet thinning (e.g., Krabill et al. 2000; Thomas et al., 2004), demonstration of the feasibility of coincident laser and radar altimeter measurements over sea ice (Giles et al., 2007), and refinement of navigation techniques and operational practices for airborne laser altimetry of polar regions.

The main components of ATM are two conically-scanning laser altimeters that independently measure the surface elevation along the path of the aircraft at 15° and 2.5° off-nadir angle, respectively (Krabill et al., 2002). During OIB, six generations of ATM transceivers (T2 to T7) and three generations of data systems (ATM4 to ATM6) were used. At the OIB-nominal AGL altitude, the 15º and 2.5º scanners have swath widths of 245 m and 40 m, respectively, with a near-constant angle of incidence. The intersecting tracks of laser footprints from the conical scan geometry allows determination of pointing biases over any type of surface (Martin et al., 2012; Harpold et al., 2016).

Four different lasers were used over the course of OIB, whose pulse repetition frequency (PRF) ranged from 3 to 10 kHz (Table 4). The laser footprint size on the surface is a function of laser beam divergence, range and angle of incidence, and it varied in diameter between 1.2 and 0.6 m over the course of OIB at the nominal AGL.

Table 4: ATM configurations

ATM laser altimeter configurations used over the course of OIB.

Transceiver	Scan angle (°)	Period of operation	Wavelength (nm)	PRF (kHz)	Pulse width (ns)	Digitizer [1]	Sampling interval (ns)	Laser type [2]
ATM-T2	15	2009–2011 2016	532	5,3	5,6	A,B	0.50	1,2
ATM-T3	22/2.5/15	2009–2015	532	5,3	5,6	A,B	0.50	1,2
ATM-T4	15	2011–2014	532	3	6	A,B	0.50	2
ATM-T5	2.5	2015–2017	532	3	6	B,C	0.50	2
ATM-T6	15	2016–2019	532	10	1.3	C	0.25	3
ATM-T7	2.5	2017–2019	532	10	1.3	C	0.25	4
ATM-T7	2.5	2017–2019	1064	10	1.3	C	0.25	4

[1] Data systems/digitizers: (A) ATM4 single-trigger, fixed gate length; (B) ATM5 multi-trigger, variable gate length; (C) ATM6 high PRF (10 kHz), multi-trigger, variable gate length.

[2] Laser types: (1) Continuum C5000 5 kHz / 5 ns; (2) Northrop-Grumman 3 kHz / 6 ns (high power); (3) Northrop-Grumman 10 kHz / 1.3 ns fiber hybrid; (4) Northrop-Grumman dual-color 10 kHz / 1.3 ns fiber hybrid.

To derive precise surface elevations for each laser shot requires knowledge of the aircraft's position and attitude. The aircraft position is determined by Global Navigation Satellite System (GNSS) systems that incorporate NAVSTAR Global Positioning System (GPS) and, for later campaigns, the Globalnaya Navigatsionnaya Sputnikovaya Sistema (GLONASS). Carrier-phase measurements are logged by an onboard antenna and receiver. In post-flight processing, these measurements are combined with those from static ground stations to produce a kinematic differential solution of the aircraft trajectory at 2 Hz, and more recently at 10 Hz. Aircraft attitude is logged from a commercial inertial navigation system (INS). Two INSs were used for attitude determination over the course of OIB: a Litton LN-100G for 2009–2010 and an Applanix 610 for all subsequent campaigns.

Several independent assessments of the vertical accuracy and precision of ATM spot-elevation measurements were made during OIB. Martin et al. (2012) analyzed the various sources of error that affect ATM elevation accuracy. The combined effects of trajectory, range-bias and laser-pointing errors induce a total uncertainty of 6.6 ± 3.0 cm for each spot-elevation measurement. Brunt et al. (2017, 2019) compared ATM with GNSS ground measurements in the interior of the Greenland and Antarctic ice sheets and found that they agreed within 6 ± 8 cm for Greenland and 3 ± 14 cm for Antarctica. Over sea ice, precision controls freeboard accuracy, which in turn contributes to total ice-thickness uncertainty (Giles et al., 2008; Farrell et al., 2011). Assessing the standard deviation of ATM elevation measurements across level first-year sea ice (a refrozen lead), Farrell et al. (2012) estimated an ATM precision of 4.7 cm. Although not directly indicative of the accuracy or precision of ATM, Kwok et al. (2019) compared near-coincident total freeboard and surface-height retrievals from ATM and ICESat-2 over sea ice over the Arctic Ocean both elevation profiles and surface roughness were very well correlated (linear correlation coefficients of >0.95 and >0.97, respectively).

A precise navigation system was required to achieve repeat-track mapping of elevation change from overlapping laser-altimeter swaths, satellite underflights or *in situ* survey overflights. OIB used 12 different aircraft types that spanned decades of aeronautical technology (§4), and only the most modern of these aircraft could steer themselves sufficiently accurately without augmented guidance (e.g., G-V). To address this challenge, ATM developed a unique aircraft navigation capability that could be ported easily between different aircraft. This navigation system used real-time input from onboard GNSS receivers to drive cockpit displays and an electronic interface to the aircraft's autopilot via the Instrument Landing System radios, which provided the necessary commonality between aircraft. The flight crew coupled the aircraft's autopilot to this system, which would automatically and continuously steer the aircraft to within a few meters of the desired ground track. The system also had a manual mode that allowed pilots to steer complex routes (e.g., sinuous glacier centerlines) with sufficient accuracy to ensure ATM swath overlap with previous flights. Deploying this navigation system also benefited other concurrently deployed instruments by minimizing aircraft roll, keeping nadir-pointed sensors pointed at nadir, and by minimizing aircraft-induced horizontal acceleration, improving the quality of gravimetry data (§3.3).

3.1.2. Land, Vegetation and Ice Sensor (LVIS)

The LVIS instrument suite includes a wide-swath, high-altitude airborne laser altimeter and a camera producing elevation and surface structure measurements of land, water and ice surfaces. LVIS is a full waveform, 1064 nm wavelength laser altimeter that records both the outgoing and reflected laser pulse shapes, providing a three-dimensional record of the surface at centimeter-level precision (Blair et al., 1999). LVIS can operate much higher than typical commercial laser altimeters, so that it may map a wider swath at higher speeds and maximize aircraft range.

LVIS maps a 12º wide (~2 km at 10 km AGL) swath centered on nadir using several unique technologies. To achieve such a wide angular field of view (FOV) with a large-diameter telescope and maintain the precise laser-pointing knowledge required for high-altitude operations, both the transmitted laser beam and the receiver FOV are scanned mechanically. To support a range of measurement geometries, the laser footprint size and spacing are configurable using lenses and a software-generated scan pattern. Several versions of LVIS were flown for OIB, representing progressive improvements in observation strategy and system design (Table 5). For the majority of OIB, LVIS was operated onboard dedicated aircraft or during dedicated flights, for optimal data collection and to fully exploit its high-altitude survey capability.

Table 5. LVIS configurations

LVIS configurations deployed during OIB.

Version [a]	v1	v2	GH	Facility
Platform(s)	P-3, DC-8	B-200, HU-25, G-V	C-130H	B-200T
Year(s)	2009–2010	2010–2015	2013	2017
PRF (kHz)	1	1.5	2.5	4
Footprint (m)	20	20	10	10

[a] Version numbers used in Tables 13–15.

Data processing combines both sensor pointing and location with the range to the surface to compute the footprint geolocation (Hofton et al., 2000). Post-flight interpretation of the laser waveform provides the elevation of the various reflecting surfaces within each footprint and the ability to quantify the three-dimensional nature of sampled terrain. Data from IMUs (Applanix 510 or 610) co-mounted with LVIS and dual-frequency GNSS observations recorded at 20 Hz from the top of the aircraft fuselage were interpreted post-mission using precise-point positioning (PPP) within Novatel's Inertial Explorer and custom software to calculate laser pointing and positioning. Angular and translational differences between reference frames were determined either in the lab or by performing calibration maneuvers over a target surface (e.g., lake). These differences were then input into a custom measurement model to generate the geolocated laser waveform vector and surface elevation, from which automatically identified artifacts (e.g., clouds) were removed (Hofton et al., 2000).

A comparison between LVIS and a commercial fine-resolution laser altimeter showed that the horizontal geolocation accuracy of the LVIS footprint is <2 m (Blair and Hofton, 1999). An assessment of repeat tracks over the Greenland Ice Sheet that were hundreds of kilometers long showed that inter-flight elevation differences were <5 cm, with precision estimates at multiple crossover locations <7 cm (Hofton et al., 2008). A comparison of LVIS to GNSS ground measurements at Summit, Greenland found that they agreed within 4 ± 7 cm (Brunt et al., 2017).

3.1.3. UAF Riegl LMS-Q240i and VQ-580 II

The primary UAF laser altimeter was a Riegl LMS-Q240i scanner. The scanner has a 905 nm wavelength laser and a rotating mirror that sweeps the pulses linearly at a 10 kHz PRF through ±30º from nadir (perpendicular to the direction of flight). This results in a ground swath whose width is roughly equal to the survey AGL (typically 300–500 m), a shot footprint of ~20 cm and a grid spacing of ~1 m both along- and across-track. Survey altitude and flight design were typically constrained to terrain-following due to the maximum range of the LMS-Q240i (~500 m). An Oxford Technical Solutions Inertial+2 IMU was mounted to the scanner both directly and rigidly, and this IMU was also connected to a Trimble R7 GNSS receiver for trajectory and positioning data. Two-stage processing of trajectory data first used Novatel GrafNav software for a PPP solution of the R7 data, followed by blending this post-processed solution with the Inertial+2 data using RTPostProcess. The scanner data were then processed with RiProcess, resulting in georeferenced point clouds. Based on cross-over analysis of Alaskan flights, LMS-Q240i precision and repeatability is ≤20 cm (Johnson et al, 2013), and based on overlap with Antarctic GNSS ground surveys, LMS-Q240i accuracy and precision are between 0.1 ± 9.7 cm and −9.5 ± 9.8 cm (Brunt et al., 2019).

Beginning in 2020, UAF began deploying a second laser altimeter, the Riegl VQ-580 II, which was coupled rigidly to an Applanix AP60-AV IMU/GNSS. This system uses a 1064 nm laser with adjustable PRF but typically operated at 100 kHz. The Riegl VQ-580 II can range seven times farther than the LMS-Q240i, permitting simplified, safer and higher surveys over steeply sloped Alaskan glaciers that dissect rugged mountain ranges. A consequence of this upgrade is that the ground footprint and spacing varies for surveys that deployed the VQ-580 II. The beam divergence is similar between the two systems, so for the same AGLs the footprints are comparable, but the point spacing of the VQ-580 II is an order of magnitude finer due to its higher PRF. Trajectory processing was done with POSpac MMS 8.4, and scanner data were also processed with RiProcess to generate georeferenced point clouds. Crossover analysis from boresight alignments suggests VQ-580 II's accuracy and precision are both ≤10 cm, i.e., at least as good as the LMS-Q240i, but a formal comparison against independent measurements has not yet been performed.

3.1.4. UTIG Sigma Space Lidar and Riegl LD-90

Photon-counting laser altimetry was the technological breakthrough underlying ICESat-2. In conjunction with OIB, NASA promoted a number of efforts to demonstrate this technology on airborne platforms prior to ICESat-2's launch. OIB collected the first photon-counting laser altimetry data in Antarctica in collaboration with Investigating the Cryospheric Evolution of the Central Antarctic Plate (ICECAP) project. The Airborne LiDAR with Mapping Optics (ALAMO) system swath-mapped surface elevation using a Photon Counting LiDAR (PCL) with a complex, multi-prism, beam-steering unit and up to 100 range-detection green channels manufactured by Sigma Space (Young et al., 2015). Absolute calibration was provided by a Riegl LD-90 nadir-pointing, near-infrared laser altimeter with an RMS elevation accuracy of 13 cm (Young et al., 2008). Deploying both instruments was necessary due to the temperature sensitivity of ALAMO's internal clocks. Aircraft orientation was provided by an iMAR FSAS IMU integrated with a Novatel SPAN GPS. Trajectories were derived using Novatel's Waypoint Inertial Explorer software and using PPP to constrain coupled orientation/position solutions. In 2009, multiple issues on a prototype PCL prevented useful data collection, while the Riegl LD-90 worked well. In 2010, due to manufacturing delays, a Honeywell GNSS/INS was used instead of the iMAR/Novatel system for aircraft orientation and positioning. ALAMO operated with a linear scan pattern and collected data over Antarctica, including the McMurdo Dry Valleys, Victoria Land, Wilkes Land and Dronning Maud Land. In 2011 and 2012, due to mechanical issues, a circular beam pattern was used with a single prism. Approaches for filtering the solar and electronic noise photons were developed, and data subsetting was employed to manage the large data volumes. Typical range precisions for the PCL were 4 cm (Young et al., 2015).

3.2. Radar sounders

Radar sounders were also fundamental to achieving many of OIB's science requirements (Tables 1–3), and a large variety thereof were deployed. Most were designed to measure ice thickness, but several others focused on measuring near-surface layers, typically to estimate accumulation rates on land or snow thickness on sea ice. Three low-frequency radar sounders (WISE, UAF HF Radar Sounder and ARES) were deployed specifically to measure the ice thickness of temperate glaciers in Alaska. For many unrepeated land-ice surveys, new radar measurements of ice thickness formed the primary rationale for the survey. Below we group these radar sounders by their primary science targets as deployed for OIB.

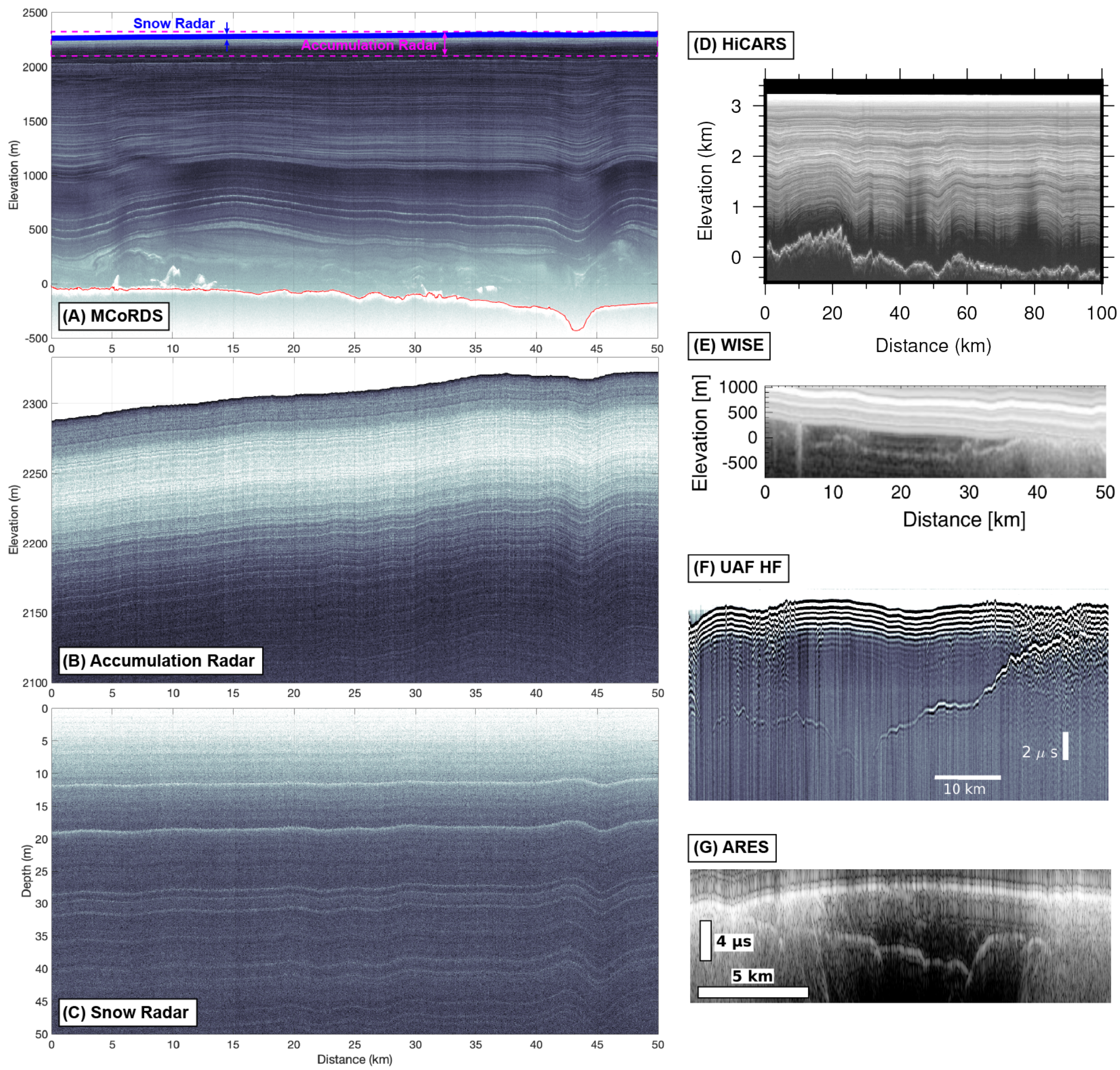

Figure 2: Radar sounders

Example OIB radar-sounder data. (A, B, C) MCoRDS v3, accumulation radar v1 and snow radar v3, respectively, from the same flight over central northern Greenland (2 May 2011). Red line in panel A indicates ice–bed reflection. (D) HiCARS v2 over Dome C, East Antarctica, from 2011. (E) WISE over Bering Glacier, Alaska; adapted from Rignot et al. (2013). (F, G) UAF HF Radar Sounder and ARES, respectively over Malaspina Glacier, Alaska.

3.2.1. Polar ice thickness and deep radiostratigraphy

3.2.1.1. Multichannel Coherent Radar Depth Sounder (MCoRDS)

MCoRDS is a multi-channel radar sounder designed to sound both the entire ice thickness of multi-kilometer-thick ice sheets and detect their internal stratigraphy at meter-scale vertical resolution. This system traces its heritage to continual improvements and refinements to previous radar depth sounders designed by The University of Kansas' Radar Systems and Remote Sensing Laboratory for use during

PARCA campaigns, and later the Center for Remote Sensing of Ice Sheets (CReSIS) at the same institution (e.g., Gogineni et al., 1998, 2001, 2007; Legarsky et al, 2001; Li et al., 2013; Rodríguez-Morales et al., 2013). The system used by OIB could support up to eight independent transmit (Tx) / receive (Rx) channels and an additional eight independent Rx-only channels. The transmitter operates over variable bandwidths with frequencies typically ranging between 150–450 MHz through the use of a synchronous eight-channel, 1.0-GHz digital waveform generator and can support peak Tx powers of 1 kW per channel. From 2009 to 2019, seven custom-made cross-track antenna arrays were developed for MCoRDS and integrated into six different aircraft for OIB (Table 6). Operating configurations depend on the aircraft and antenna array. A cross-track antenna array enables dynamic Tx and Rx beamforming. The receiver supports direct data capture on up to 16 independent channels, each with a synchronous high-speed digitizer (up to 1.6 GHz) with real-time but minimal hardware digital signal processing to reduce overall data rates.

Table 6. MCoRDS configurations

MCoRDS operating configurations during OIB campaigns.

Version [a]	v1	v2	v3	v4	v5	v6	v7
Platform	DC-8	DC-8	P-3	C-130H	WP-3D	DC-3T	G-V
Year(s)	2009–2013	2014–2018	2010–2019	2015	2016	2017	2019
Frequency range (MHz)	189–199	165–215	180–210	150–450	150–450	150–450 [b]	236–254
Vertical resolution [c] (m)	16.9	3.4	5.6	0.6	0.6	0.6	9.4
Pulse duration (μs)	1, 10, 30	1, 3, 10	1, 3, 10	1, 3, 10	1, 3, 10	1, 3, 10	1, 3, 10
PRF (kHz)	9, 12	12	10,12	12	12	12	12
Sampling frequency (MHz)	111.11	150	111.11	1600	1600	1600	142.85
ADC resolution (bit)	14	14	14	12	12	12	14
Transmit aperture size [d] (m)	2.3	2.3	5.4	0.5	0.5	3.85	1.9
Peak transmit power (kW)	0.55–1.5	6.0	1.05–3.5	2.0	2.0	2.4	2.0
Number of channels [e]	5,0	6,0	7,8 [f]	2,0	2,0	8,0	4,0

[a] Version numbers used in Tables 13–15.

[b] In 2017, MCoRDS also operated in the 180–210 MHz range during some of the flights, resulting in 5.6 m vertical resolution.

[c] In ice, assuming the values of the real part of the relative permittivity and the windowing factor are 3.15 and 2, respectively.

[d] Cross-track, fully programmable.

[e] Tx/Rx channels, Rx-only channels.

[f] In 2010, MCoRDS operated with a 16:8 RF multiplexing module to capture data from seven Tx/Rx channels and eight Rx-only channels using a digitizer bank.

Because the Tx and Rx channels were operated independently, MCoRDS had to be calibrated prior to each campaign to account for variability in cable routing and radio-frequency (RF) electronics. System calibration was accomplished by operating MCoRDS at high altitude with minimal roll over a reflective and level surface (typically open water), in which all Tx/Rx channel combinations are expected to produce equal signal delay, amplitude and phase responses. A set of near-real-time onboard algorithms were developed to generate the necessary corrections to be applied to the digital waveform generator for each channel. These corrections equalize the variations detected during the level flight. Due to non-linear transmitter behavior, this process was repeated until these corrections converged. Once the Tx channels were calibrated, a number of roll operations (±60º) were performed over open and calm ocean or fjord surfaces to collect independent Rx data and generate steering vectors for beamforming and clutter cancellation. This process was repeated during OIB campaigns whenever surface and flight conditions permitted it.

For most OIB campaigns, MCoRDS operated in a nadir-sounding mode focused on sounding the entire ice column beneath the aircraft. In this mode, Tx antennas were time- and phase-aligned to maximize nadir-directed power to detect deep internal reflections and the ice–bed reflection, while reducing energy transmitted off-nadir. This mode time-multiplexes multiple pulses to capture the large dynamic range of the backscattered signal. A low-gain Rx and short pulse measures the strong ice-surface reflection and shallow internal reflections, and one or two high-gain and longer pulses measure the deeper and weaker reflections, including ice–bed backscatter. During the 2018 and 2019 Arctic spring campaigns and on select surveys in earlier years (in particular 2014 over the Canadian Arctic Archipelago), MCoRDS was instead operated in an imaging mode. In this mode, the Tx beamwidth is purposely spread over a wider angular range so that off-nadir targets are illuminated and a wider swath beneath the radar can be measured. Synthetic aperture radar tomography is used to process the data collected in this mode (e.g., Paden et al., 2010; Jezek et al., 2011). Although the nadir-sounding mode does not illuminate a wide swath, data collected using that mode can also be processed tomographically to generate swath images, but the achievable swath is generally narrower.

3.2.1.2. High Capability Radar Sounder (HiCARS)

HiCARS is a 60 MHz coherent radar system with a technical heritage extending to the original NSF/SPRI/TUD surveys of Antarctica in the 1970s (Gudmandsen, 1975; Schroeder et al., 2019). The modern version of HiCARS was first flown in 2000 on a DHC-6T as part of the Advanced Technology Radar Sounder project (e.g., Peters et al., 2005) and then used for the AGASEA survey of Thwaites Glacier in 2004–2005 (Holt et al., 2006). HiCARS was reconfigured onto a DC-3T for OIB/ICECAP. In 2010, the initial, mostly custom-built HiCARS (v1) was largely replaced with a substantially lighter version using commercial components with similar performance (v2).

Waveforms were downconverted in analog to a 10 MHz center frequency to allow for 14 bit digitization of the coherent waveforms. Two channels allowed for both low- and high-gain recording of the same waveform across 120 dB of dynamic range, permitting high radiometric fidelity for the ice surface and bed reflections. A short 1 μs chirp with a 15 MHz bandwidth was used, limiting the depth extent of the range sidelobes but inducing high range sidelobes in the first 1 μs below the surface. With an effective coherent PRF of 200 Hz after onboard stacking and typical Doppler bandwidths of 36 Hz, HiCARS samples typical Doppler bandwidths at a factor of ≥5. For OIB, data was processed using a short coherent stack from 200 to 20 Hz (real-time) to suppress along-track surface scattering, with five incoherent stacks to suppress speckle.

3.2.1.3. Pathfinder Advanced Radar Ice Sounder (PARIS)

PARIS was a VHF radar sounder originally designed to demonstrate high-altitude radar sounding of ice using delay-Doppler processing of coherently recorded waveforms (Raney et al., 2008). As deployed by OIB, this system included a pair of orthogonal, linearly polarized antenna elements that were induced with a chirped waveform with a 6 MHz bandwidth centered at 150 MHz, mounted within the bomb bay of the P-3. Despite its design intended for operation at high altitude, PARIS was operated at the OIB nominal AGL during the first OIB Arctic campaign in 2009 only.

3.2.2. Temperate glacier thickness

3.2.2.1. Warm Ice Sounding Explorer (WISE)

WISE was based on the Mars Advanced Radar for Subsurface and Ionosphere Sounding radar (Jordan et al., 2009). It consisted of a single Tx/Rx operating on a dipole antenna deployed out the back of an aircraft. The high-power Tx had a limited duty cycle designed to produce high-amplitude, single-frequency tone bursts, which were derived from either a continuous-wave signal or externally generated. The radar-wave generator and timing were synchronized using the same clock. Instead of using a Tx/Rx switch, WISE used a diplexer so that the Rx system was always connected to the antenna but isolated from the Tx burst. The resistively loaded wire antenna was housed inside a 120 m long static rope that was both electrically coupled to the aircraft and damped to minimize ringing. This feature allowed operation between 1–5 MHz at a radiated power of 80 W. A trailing drogue and counterweight was attached to the antenna to maintain a dip of 30º relative to horizontal during flight. WISE was best suited for aircraft that are significantly smaller than the radar wavelength (120 m in air). The WISE center frequency was 2.5 MHz, with a 1 kHz pulse repetition frequency digitized at 20 MHz and 16 bits within a 50 µs window at a typical peak power of 800 W. Because of low survey AGLs (~200 m), the ice-surface reflection was clipped, but that also limited Rx saturation and increased ice–bed reflection signal-to-noise ratio (SNR). Geolocation came from a GNSS receiver with a precision of 10 m sampling at 20 Hz.

Initial radar data processing included incoherent along-track averaging, followed by range migration. Ranges to the glacier surface and bed were digitized semi-automatically, but absolute surface elevation was determined either from contemporaneous laser altimetry (Greenland) or existing near-contemporaneous digital elevation models (DEMs). The theoretical vertical resolution of the 2.5 MHz WISE data was ~67 m in ice, and its measured thicknesses compared well with MCoRDS (195 MHz; §3.2.1) in Greenland (mean difference of 28 ± 55 m) and HiCARS (60 MHz; §3.2.2) in East Antarctica (12 ± 25 m) during other non-OIB surveys.

3.2.2.2. UAF HF Radar Sounder

The UAF high-frequency (HF) Radar Sounder was essentially identical to that described by Conway et al. (2009) and Truffer (2014), which successfully measured ice thicknesses exceeding 1200 m. The Tx is a center-fed dipole antenna towed behind the aircraft. A half-dipole Rx antenna terminates in the aircraft, where the received signal is digitized. The antennas are all resistively loaded to avoid ringing. The dipole antenna is 80 m long, producing a 2 MHz pulse. A 4 kV monopulse is generated with a Kentech Instruments impulse generator and is typically operated at 1 kHz PRF to increase SNR. Shorter antennas can be substituted to produce higher-frequency signals and better resolution, but experience showed that thick, temperate ice requires a low frequency for successful detection of the ice–bed reflection.

The signal was digitized and stored on a National Instruments (NI) controller. An embedded computer runs a high-speed digitizer and GNSS Rx. Data acquisition is triggered with the airwave, sampled at 200 MHz and digitized across 12 bits, corresponding to a dynamic range of 66 dB. The NI Reliance file system guarantees data storage even in the event of an abrupt power failure. The Tx/battery enclosure is deployed through the aircraft's belly port adjacent to the UAF Riegl, so that simultaneous measurements can be achieved. The stacked radargrams have an along-track spacing of 0.5 m at a typical aircraft speed of 100 kt (~51 m s^{-1}). Cross-over analysis of ice-thickness measurements between ground-based deployments of the UAF HF Radar Sounder on the Harding Icefield and WISE on Malaspina Glacier agree to within 20 m (Truffer, 2014).

3.2.2.3. Arizona Radio Echo Sounder (ARES)

ARES is a low-HF, chirped radar system that operates at a center frequency of either 2.5 or 5 MHz, with either 2.5 or 5 MHz bandwidth, respectively. Range resolution at these frequencies is 60 m at 2.5 MHz and 30 m at 5 MHz. As for WISE and the UAF HF Radar Sounder, using this frequency range improves radio-wave penetration through the thick, temperate glaciers of southern and southeastern Alaska. ARES uses a single, resistively loaded antenna element towed behind the aircraft for both Tx and Rx. This resistive loading permits a good antenna response over a wide bandwidth but reduces antenna efficiency. A 2 kW peak power signal is fed into the antenna, but the radiated power is much less due to the resistive loading. The towed element is 60 m long at 2.5 MHz and 30 m for 5 MHz.

ARES hardware and software both evolved over the course of OIB. ARES initially used NI hardware with custom LabView software to generate and digitize the radar signal. In 2019, ARES transitioned to an Ettus X310 software-defined radio. After the Tx signal is generated by the X310, it is amplified by a Tomco BT02000-AlphaS power amplifier and then fed to the antenna. An antenna coupler performs impedance matching and isolates the Rx hardware from the outgoing signal. The Rx signal is filtered and amplified by a Ritec BR640A broadband receiver and then digitized by the X310 at 100 MHz across 14 bits.

Data processing consists of pulse compression with either a synthetic chirp or a reflected chirp from the ocean surface and removal of a windowed along-track mean. Due to the low-altitude operation required by the UAF Riegl LMS-Q240i (<500 m AGL; §3.1.3), the air–ice reflection returns while ARES is still transmitting and is not recoverable. Contemporaneous laser altimetry is instead used to estimate the traveltime of the unobserved surface reflection, and ice thickness is measured based on the traveltime difference between the inferred surface and the observed bed reflections. Final geolocation is provided by the same GNSS receiver used by the UAF Riegl.

ARES was deployed in Alaska for the 2015–2020 OIB campaigns and successfully sounded ice more than 1200 m thick within the western Bagley Icefield. Surface clutter, i.e., reflections from off-nadir topography like valley walls, is a significant obstacle to successful radar sounding of mountain glaciers (Holt et al., 2006). Surface clutter can return to the antenna at the same time as bed reflections, making it a significant confounding factor in interpretation. Because of this challenge, an integral component of ARES post-processing is comparison of its radargrams against a surface-clutter simulator, which prevents the incorrect interpretation of predicted surface clutter as the ice–bed reflection instead.

3.2.3. Shallow radiostratigraphy and snow thickness

3.2.3.1. Accumulation radar

The accumulation radar is an ultra-high frequency radar sounder designed to measure ice-sheet internal layering at sub-meter vertical resolution and to sound thinner (1–2 km) polar ice. Prior to OIB, this system concept was demonstrated using a 170–2000 MHz frequency-modulated continuous-wave (FMCW) signal to perform an *in situ* survey of the North Greenland Ice Core Project site (e.g., Kanagaratnam et al., 2001). The system was then modified for airborne operation to the current 600–900 MHz band (Kanagaratnam et al., 2004). Early versions were also operated as a FMCW system. This configuration permitted large bandwidths but transmitted continuously, so Tx power was limited to ~1 W to prevent degradation of Rx sensitivity. During the early years of OIB, the accumulation radar was operated as a step-frequency chirped pulse radar with low-speed data converters (Table 7). It was later upgraded to operate as a chirped pulsed radar using high-speed data converters at a 50 kHz PRF (Lewis et al., 2015), followed by the current system, which directly generates and samples the signal's entire bandwidth. A pulsed chirp permits much higher peak Tx powers (400 W) and overall improved performance. Due to limited availability of nadir ports capable of supporting the accumulation radar on most aircraft, it was deployed on the P-3 only.

Table 7: Accumulation radar configurations

Key characteristics of accumulation radar configurations operated during OIB.

Version [a]	v1	v2	v3
Years	2010–2011	2012–2014	2017–2018
Vertical resolution (cm) [b]	53 (43)	53 (43)	53 (43)
Pulse duration (μs)	2.048	2.048	2
Sampling frequency (MHz)	125	1000	1600
ADC resolution (bit)	14	8	12
Peak transmit power (W)	1.25	5	400

[a] Version numbers used in Tables 13–15.

[b] Best-case scenario assuming the windowing factor is 1.5 and the real part of the relative permittivity is 2.1 for firn (3.15 for ice).

3.2.3.2. Snow, Ku- and Ka-band Radars

The CReSIS ultra-wideband FMCW radars include the snow radar (2–8 GHz), the Ku-band Radar (12–18 GHz) and more recently the Snow/Ku Radar covering the entire bandwidth of those first two systems (2–18 GHz). Combined, we simply refer to these as "snow radar". A millimeter-wave front-end was also developed for Ka-band (32–38 GHz) operation during one OIB campaign (2015 Arctic spring). These systems provide large-scale measurements of near-surface snow layering over land ice and snow thickness over sea ice at centimeter-scale vertical resolution. The multiple operating bands also permit investigation of frequency-dependent extinction rates in the upper firn.

The snow radar concept was originally demonstrated in 2003 during *in situ* surveys on Antarctic sea ice (Kanagaratnam et al., 2003), and later in 2006 on the NASA P-3. The transition to airborne operation was challenged by the need to generate a sub-millisecond ultra-linear chirp over multi-gigahertz bandwidths (Patel, 2009). By leveraging advances in solid-state electronics, an airborne configuration with 2 GHz bandwidth was successfully demonstrated in 2009 as part of the first OIB campaign (Farrell et al., 2012; Panzer et al., 2013). The Snow and Ku-band radars were operated as separate systems until 2017. Subsequent system improvements included enhancing the frequency linearity of the Tx chirp while expanding its bandwidth, increasing the average Tx power from ~0.1 to ~1 W and sampling the radar's output signal at increasingly higher rates (Gomez-Garcia et al., 2014, Yan et al., 2017, Rodríguez-Morales et al., 2020; Table 8). These improvements resulted in a system that operated over 2–18 GHz and eliminated the need for separate Snow and Ku-band radars.

Table 8: Snow radars

Key characteristics of snow radars operated during OIB.

Version [a]	v1	v2	v3	v4	v5	v6
Platform(s)	DC-8	DC-8, P-3	DC-8, P-3	DC-8, P-3, C-130H, WP-3D	DHC-3T	P-3, DC-8, G-V
Year(s)	2009	2010	2011	2012–2016	2018	2017–2019
Snow frequency range [b] (GHz)	4–6	2–6.5	2–6, 2–6.5	2–8	2–8	2–18

Ku frequency range [c] (GHz)	14–16	12.5–13.5, 13–17	13–17	12–18	N/A	N/A
Vertical resolution (cm) [d]	12	5.4	5.4	4	4	1.5
Pulse duration (μs)	100–240	250	250–255	250, 240	250	240
PRF (kHz)	2, 3	2	2	2, 4	2	4
IF sampling frequency (MHz)	62.5	62.5	62.5	62.5, 125	125	250
ADC resolution (bit)	14	14	14	14	14	14

[a] Version numbers used in Tables 13–15.
[b] Snow radar operating at full bandwidth.
[c] Ku-band altimeter operating at full bandwidth.
[d] Best-case scenario assuming full-bandwidth operation, a windowing factor of 2, and a value of 1.53 for the real part of the relative permittivity of near-surface snow.

3.3. Gravimeters

Airborne measurements of Earth's gravity were collected intermittently by OIB but were essential to addressing key requirements regarding fjord and sub-ice-shelf bathymetry. Because of the unique challenge of collecting gravity data onboard fast-moving aircraft subject to turbulence, particular attention was paid to gravimeter accuracy and data filtering. The commercial AIRGrav system was the primary gravimeter deployed by OIB, but due to its cost and size, other gravimeters were also deployed.

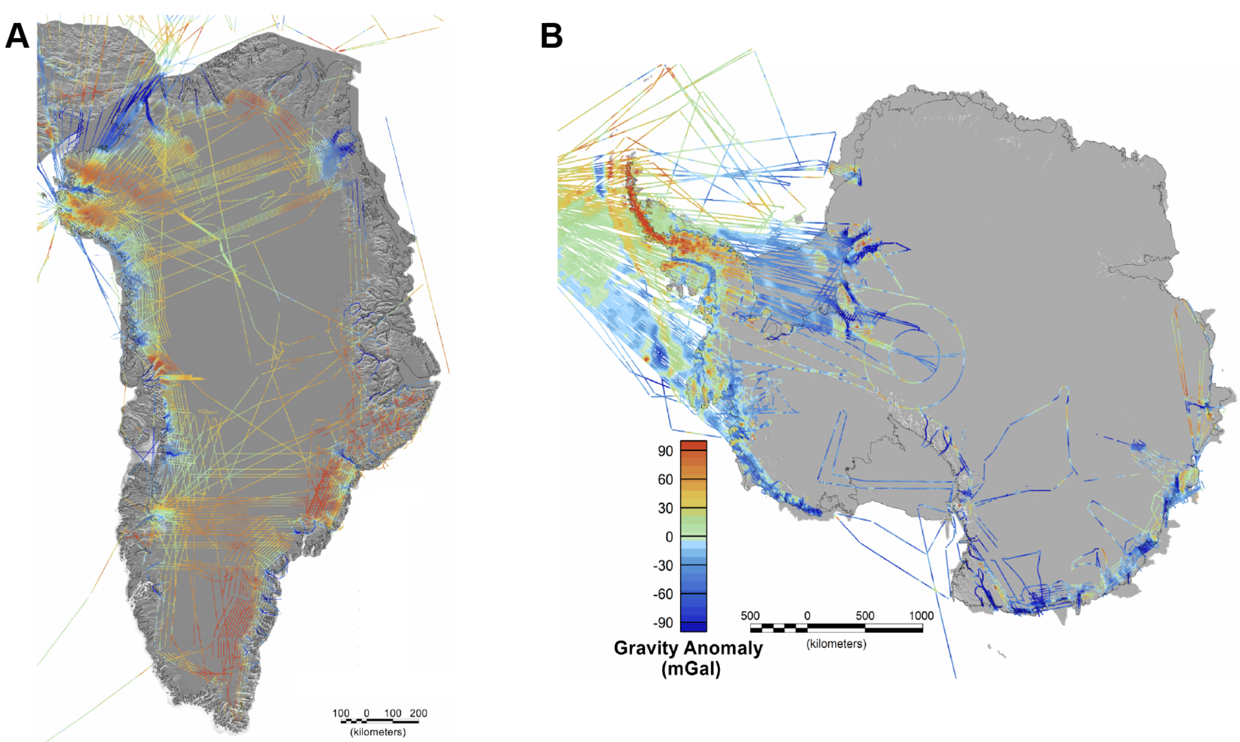

Figure 3: Gravimeters
Free-air gravity anomaly from OIB surveys of (A) Greenland and (B) Antarctica. Greenland data are AIRGrav only, whereas Antarctic data include AIRGrav (mostly West Antarctica), and iMAR/DgS, BGM and GT-1A data across Wilkes Land, East Antarctica.

3.3.1. Airborne Inertially Referenced Gravimeter (AIRGrav)

Sander Geophysics' AIRGrav is a Schuler-tuned inertial platform that supports three orthogonal accelerometers (Argyle et al., 2000; Studinger et al., 2008). The accelerometers remain fixed in inertial space, independent of aircraft maneuvers, allowing precise correction for those maneuvers. Accelerometer data were recorded at 128 Hz. Ground-based GNSS reference stations used a Novatel DL-4 receiver. The Novatel Millennium, 12-channel GPS Satellites, 12-channel GLONASS Satellites, two-channel SBAS, single-channel L-Band multi-frequency receiver was an integral part of the DL-4 system. Flight trajectory and gravity anomaly were processed using the manufacturer's in-house processing software. Noise in the survey data was reduced by applying a cosine-tapered lowpass filter in survey time. The shortest filter used was 70 s, which at typical flight speeds of ~240 kt (120 m s^{-1}) provided full-amplitude recovery of gravity anomalies with half-wavelengths greater than ~4.2 km. The full dataset was leveled to minimize crossover differences between surveys. Under typical OIB survey conditions, AIRGrav's accuracy, calculated from the standard deviation of differences for 70 s filtered data, was 0.7 mGal for repeat surveys and 1.0 mGal at crossovers. For each campaign where AIRGrav was deployed, the same instrument model was used.

3.3.2. UTIG gravimeters (BGM-3, ZLS and GT-1A)

Three gravimeters were used by OIB/ICECAP during four campaigns: 1. A Bell Aerospace BGM-3 gravimeter (2009, 2010 and 2011 campaigns); 2. LaCoste and Romberg AirSea gravimeter modified by ZLS Corporation that operated alongside the BGM-3 during the 2011 campaign; 3. A Gravimetric Technologies GT-1A gravimeter was used during the 2012 campaign.

The BGM-3 (provided by the National Geospatial Intelligence Agency) uses a force-balance vertical accelerometer for gravity sensing mounted aboard a two-axis gyro-stabilized platform. It was originally developed for marine use and later adapted for airborne applications (Bell and Watts, 1986). UTIG used the BGM-3 throughout the 1990s in Antarctica aboard a DHC-6T, and then moved to the DC-3T for OIB/ICECAP. Aboard the DHC-6T, the BGM-3 achieved accuracies of 1.5 mGal without line-leveling corrections (Holt et al., 2006). The more challenging flight dynamics of the DC-3T and the more complex flight profiles required to achieve OIB science requirements resulted in typical accuracy estimates of about 3.7 mGal for the BGM-3 onboard the DC-3T, without line leveling or other data fitting. Final gravity solutions were smoothed using a 150-s-wide moving average filter which, at typical DC-3T speeds of 90 m s^{-1}, allowed recovery of full-amplitude gravity anomalies with half wavelengths of 5–6 km.

The ZLS gravimeter (provided by the British Antarctic Survey) uses a horizontal beam balanced with a zero-length spring integrated onto a two-axis stabilized platform. It was used as a backup only, and its data were archived but not processed into a final gravity product. Carrier-phase GNSS data for the first three OIB/ICECAP campaigns were acquired from a combination of Ashtech Z-Surveyor and Z-Extreme receivers, Topcon GB-1000 and Net-G3A receivers, and a Novatel SPAN-SE receiver connected to four aircraft antennas mounted over the center of gravity, on the tail and on each wing.

The GT-1A is a vertical scalar gravimeter with an accelerometer mounted aboard a GNSS-aided Schuler-tuned three-axis inertial platform. The primary gravity sensor is composed of a vertical accelerometer with an axial design using a reference mass on a spring suspension with a photoelectric position pickup and moving-coil force feedback transducer. The sensor's suspension design minimizes the confounding horizontal accelerations induced by aircraft motion (Gabell et al., 2004). Additional accelerometers are used to discriminate sources of noise. Accelerations, rotation rates and the orientation of the platform are measured at 300 Hz before they are filtered and recorded at 18.75 and 3.125 Hz (Gabell et al., 2004). A Javad Quattro G3D GNSS receiver provided real-time heading, velocity and latitude to aid platform leveling. For polar surveys, the system uses specific high-latitude control software. GT-1A data were processed with proprietary software including Kalman-type filtering and a moving average filter of variable width (usually 150 s), which resulted in recovery of full-amplitude gravity anomalies with half-wavelengths of 5–6 km at typical DC-3T speeds during the 2012 OIB/ICECAP campaign.

3.3.3. iMAR/DgS

The gravimeter suite developed by the Lamont-Doherty Earth Observatory combines an iMAR iNAV-RQH-0018-GUG IMU as a strapdown gravimeter with a DgS Advanced Technology Airborne Gravity Meter that uses a stabilized platform and full force-feedback zero-length spring sensor. The system was tested in Greenland during the 2017 Arctic spring campaign and was the operational gravimeter during the 2019 Antarctic G-V campaign. The iMAR sensor recovers full amplitude on gravity anomalies with half-wavelength ~5 km or more. Trajectories were processed using Novatel Inertial Explorer. The DgS sensor is used to constrain long-wavelength drift during flights. Leveled line segments have an accuracy of 1.6 mGal, based on crossover analysis.

3.4. Magnetometers

Aeromagnetic data was mostly collected early during OIB's lifetime, but it directly informed gravity inversions for bathymetry by providing an independent constraint on local geology. Magnetometers were primarily selected based on their availability and aircraft compatibility.

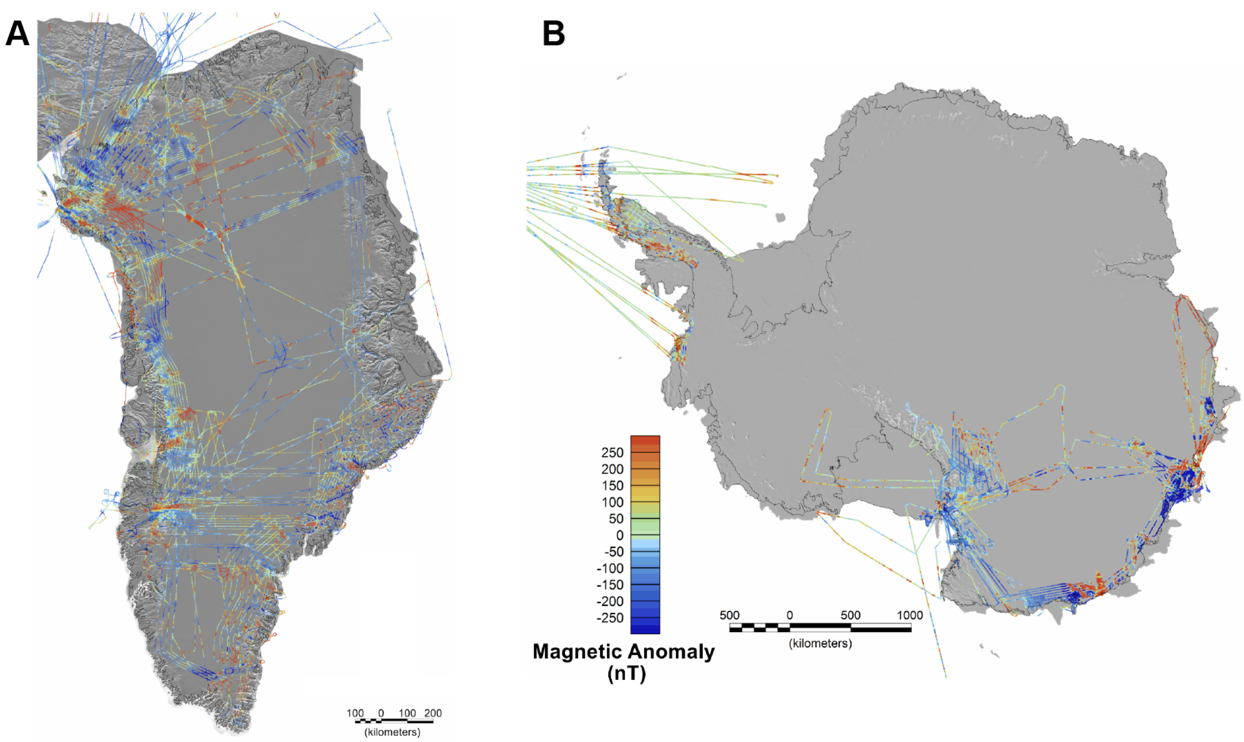

Figure 4: Magnetometers
All OIB magnetic anomaly data for (A) Greenland (Scintrex CS-3 only) and (B) Antarctica (Geometrics 823A and Scintrex CS-3).

3.4.1. Scintrex CS-3

The Scintrex CS-3 cesium-pumped vapor magnetometer was mounted inside the tail boom of the P-3 during two Arctic spring campaigns (2011, 2012) and both Antarctic ones (2013, 2017). The sensor consists of a Larmor amplifier, a lamp heater, absorption cell and a RF lamp exciter. The sensor outputs a sinusoidal wave whose frequency is proportional to the total magnetic field. In addition to this total field measurement, a Billingsley TFM100G2 three-axis fluxgate magnetometer was deployed that outputs three analog signals proportional to the flux that the aircraft traverses as it flies. This sensor records the components of the magnetic field in the direction of the current pitch, roll and yaw of the aircraft. This permits removal of the aircraft motion's contribution to the total magnetic flux in post-processing. Data were corrected for temporal (especially diurnal) variation of Earth's magnetic field using base stations, either those established specifically for each campaign or from the International Real-time Magnetic Observatory Network (INTERMAGNET) of permanent magnetic observatories. These data were logged at either 100 or 160 Hz and processed using trajectories from the AIRGrav data system. Data quality was assessed during the 2011 Arctic spring campaign by comparing the magnetic anomaly from six repeat surveys between Thule Air Base and Camp Century. The means for each survey were removed, and the standard deviation of their differences was 7 nT.

3.4.2. Geometrics 823A

A Geometrics 823A self-oscillating, split-beam Cesium vapor magnetometer was flown on all four OIB/ICECAP campaigns between 2009–2012 onboard a DC-3T. This system is composed of sensor and signal-amplifier modules mounted in a tail boom and an analog-to-digital conversion module mounted to an instrument rack in the cabin. As with the Scintrex CS-3 (§3.4.1), the magnitude of the total field is proportional to the instrument's sinusoidal output signal. The digitized output is logged to the same centralized acquisition and time-synchronization system used by other onboard instruments. A Watson FGM-301 fluxgate magnetometer was also operated during all flights to enable post-processing removal of aircraft-induced fields, but it was ultimately determined that this additional instrument was not essential (Aitken et al., 2014). Base-station data were acquired and archived with each flight to enable removal of the temporal variation of the observed field using either a Geometrics 823B or the closest INTERMAGNET station, or from both if possible.

3.5. Optical, infrared and hyperspectral cameras

Nadir imagery at a variety of wavelengths was a ubiquitous component of OIB Arctic and Antarctic campaigns. Visible imagery was particularly essential for sea ice surveys, because it enabled identification of ice-free leads needed for reliable freeboard estimates from laser altimetry. These cameras of various types were selected primarily based on their ability to fulfill OIB science requirements, the spectrum they sampled, their reliability, aircraft compatibility and cost.

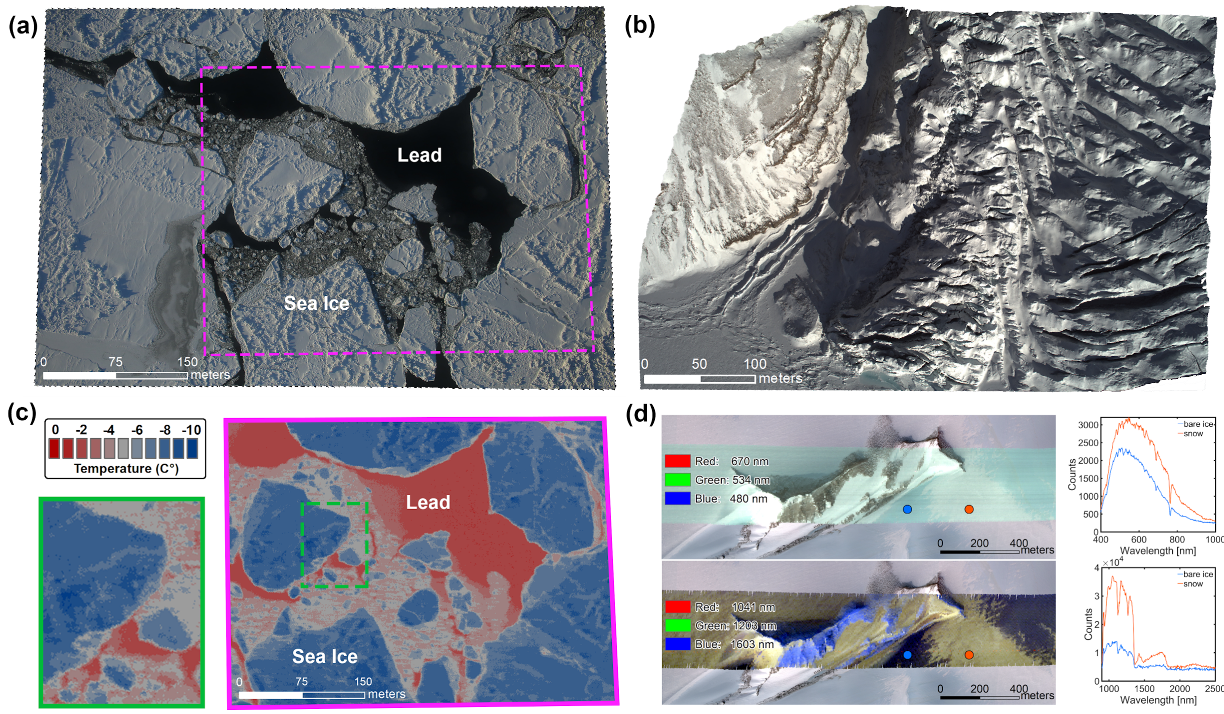

Figure 5: Imagers

Example OIB imagery. (a) DMS v2 image over deformed sea ice in the Beaufort Sea (11 March 2017). (b) CAMBOT v2 image over the south terminus of Croker Bay glacier on Devon Island, Canada (3 April 2019). (c) FLIR 655sc image of a portion of the same scene shown in panel (a) outlined in magenta. Green box shows a zoomed-in portion of the FLIR image. (d) Headwall Co-Aligned VNIR-SWIR imagery and spectra over Pioneers Escarpment, Antarctica (14 November 2018).

3.5.1. Digital Mapping System (DMS)

DMS is a nadir-viewing airborne digital camera system that produces fine-resolution georeferenced imagery, either in natural color (most OIB campaigns through 2018) or panchromatic (2009 Antarctica only). It has three primary components: a camera, navigation data system and intervalometer. The imager is a commercial digital single lens reflex camera with a rectangular complementary metal oxide semiconductor array. Over the course of OIB, two camera body types were used (Table 9). Three factors were considered to determine lens and mounting orientation: 1. To approximate the cross-track field of view of the laser altimeter; 2. Make spatial resolution as fine as possible; and 3. Produce stereoscopic coverage. Continuous imagery collection was ensured by mounting a primary and backup camera over the camera window (when permitted by aircraft configuration). An operator continually monitored camera function, focus, exposure and frame rate, and made manual adjustments as required by flight conditions.

Table 9. DMS and CAMBOT specs

Camera and survey specifications for DMS and CAMBOT.

Optical system	DMS v1	DMS v2	CAMBOT v1	CAMBOT v2
Camera body	Canon 5D Mark II	Canon 5D Mark III	Canon Rebel XTi	AVT Prosilica GT4905C
Lens	Zeiss Distagon 28 mm 2/28 ZE	Zeiss Distagon 28 mm 2/28 ZE	Canon 18–55 mm (set to 18 mm)	Zeiss Distagon 28 mm f/2 ZF.2

Acquisition rate (Hz)	1	1	0.25	2
Years operated	2009–2013	2014–2018 [a]	2009–2017	2018–2019
Cross-track FOV (°)	46	46	42	50
Along-track FOV (°)	65	65	63	35
Nadir pixel resolution (cm)	10	10	14	9
Swath width (m)	380	380	350	430
Swath length (m)	570	570	550	290
Image overlap (%) [b]	~60	~60	0	~80

[a] For the high-altitude 2015 Arctic fall campaign, DMS used an 85 mm lens (FOV 16×24°, 70 cm resolution); for the high-altitude 2015 Antarctic campaign, DMS used a 100 mm lens (FOV 14×20°; 75 cm resolution).
[b] At nominal OIB survey AGL (460 m) and ground speed (280 kt or 144 m s^{-1}).

Image processing requires referencing each frame to the navigation system, location and pointing knowledge, characterization of lens distortions and derivation of mounting angles. The internal camera clock is not accurate and drifts significantly from the navigation data system, so the camera is referenced to an Applanix 510 IMU with a custom intervalometer. The intervalometer emits a pulse triggering the camera shutter and time-tagged by the IMU. Prior to each deployment, each camera/lens pair is optically calibrated, characterizing the principal point, radial and decentering distortions and focal length. As part of the integration check flight, orthogonal lines were flown over a site whose ground-control points were surveyed with GNSS to derive camera and INS alignment angles. Georeferenced images were output as 95% compressed JPEG stored as GeoTIFFs.

3.5.2. Continuous Airborne Mapping by Optical Translator (CAMBOT)

The CAMBOT optical imaging system is part of the ATM instrument suite and was operated concurrently with ATM laser altimeters during most OIB campaigns. There were two versions of CAMBOT: the first, simpler system (v1) was used primarily as a visual quality control for ATM data processing and early derived products (e.g., 2009 sea ice freeboard), with only rough georeferencing information available; the second, improved system (v2) was upgraded substantially, with more robust, shutterless hardware, improved orthorectification and georeferencing (Table 9). Because CAMBOT v1 was a tertiary instrument, it sometimes failed during campaigns and its data were rarely examined. CAMBOT v2 replaced DMS to become the primary camera system beginning with the 2018 Antarctic campaign. For CAMBOT v2, image collection was triggered using a GNSS receiver timing pulse, with the time of image acquisition set to trigger pulse, as it was a shutterless camera that could not use flash curtain signals. CAMBOT v2 was generally operated automatically, with exposure adjusted according to histogram-based presets. During sea ice flights, CAMBOT v2 was often operated manually to avoid excessive automatic exposure adjustments due to the dynamic range in brightness of a lead-rich sea ice surface. For all campaigns, images were recorded as natural-color compressed JPEGs with a quality setting of 95%. Camera mounting biases were determined in a similar manner to DMS.

3.5.3. Heimann KT-19.85 (KT-19)

Several pyrometers were deployed during OIB to gather surface-temperature data, primarily to support sea-ice lead detection in low-light conditions. The KT-19 is a nadir-pointing infrared pyrometer for spot measurement of surface temperature (Table 10). Between 2012–2015, KT-19 was the primary thermal sensor, but it was operated throughout most of OIB. Onboard the P-3 and C-130H, it was part of the ATM instrument suite, and onboard the NASA DC-8 it was operated by the National Suborbital Education and Research Center (NSERC). KT-19's serial digital data output was combined with the aircraft position captured by a dedicated GNSS logger (P-3 and C-130H) or an aircraft data system (DC-8).

Table 10: Pyrometers

Pyrometer configurations used during OIB.

Sensor	FOV (°)	Period of operation	Data rate (Hz)	Image resolution (px)	Digitizer resolution (bit)	Accuracy (K)
Heimann KT-19	2° spot	2012–2020	10	N/A	12	0.5
FLIR A325sc [a]	45º, 15º	2015	1	320 × 240	16	2
FLIR A655sc	45º	2016–2020	1	640 × 480	14	2

[a] The FLIR A325sc was operated with a 45º lens during the 2015 Arctic spring campaigns (Table 13); a 15º lens for improved high-altitude performance was used during part of the 2015 Arctic fall campaign.

3.5.4. FLIR A325c and A655sc

Beginning in 2015, OIB deployed forward-looking infrared (FLIR) imaging pyrometers in a nadir-pointing configuration as part of the ATM instrument suite and a potential replacement for KT-19 (Table 11). Following successful evaluation of FLIR A325c data in 2015, a FLIR A655sc with improved resolution was deployed beginning in 2016 through the remainder of OIB. On smaller aircraft (e.g., HU-25, G-V), only the FLIR was deployed due to payload considerations and its greater value as an imager. FLIR A655sc images spanned a width slightly larger than that of the ATM wide-scanner swath and had a pixel size of roughly 0.6 m at 460 m AGL. FLIR data were captured by proprietary software and converted from instrument counts to spectral radiance using empirical relations and then to temperature using Planck's law. Lens-distortion corrections were applied and the images were georeferenced using ATM trajectory data.

3.5.5. Headwall imaging spectrometers

Beginning in 2017, commercial imaging spectrometers (also known as hyperspectral imagers) were deployed as part of the ATM instrument suite to better map the spectral properties of snow and ice surfaces (Table 11). These were considered experimental instruments, because the Headwall models that OIB deployed were originally designed for short-range uncrewed aerial vehicles and adapting them to the higher ground speeds and multi-hour collection of typical OIB flights proved challenging. The first instrument deployed (Nano-Hyperspec) operated only within the visible and near-infrared (VNIR) portion of the spectrum, while the second instrument deployed thereafter had two, co-aligned VNIR and short-wave infrared (SWIR) sensors. Both imagers are pushbroom sensors. Only limited processing of Headwall data was performed, and as of this writing no data from these instruments has been formally released.

Table 11: Imaging spectrometers

OIB imaging spectrometer configurations.

Headwall sensor	Period of operation	Spectral range (nm)	Spectral bands	Digitizer resolution (bit)	Across-track pixels	Nominal swath width (m) [a]	Across-track spatial resolution (m) [a]
Nano-Hyperspec	2017	400–1000	270	12	640	264	0.41

Co-Aligned VNIR-SWIR [b]	2018–2019	400–1000, 900-2500	270, 267	12, 16	640	264	0.41

[a] Assuming 460 m AGL.
[b] If two values are reported, then the first value is for VNIR spectral range and second is for SWIR.

4. Aircraft

OIB used 15 different aircraft during 12 years of campaigns, including aircraft owned and operated by NASA, by other US government agencies or commercial aircraft services (CAS; Figure 6; Table 12). This flexibility in aircraft selection was critical to achieving OIB's science requirements across the cryosphere in an ever-evolving logistics and funding environment (§2). The deployment of larger aircraft was particularly important for surveying the most remote science targets in the Arctic and Antarctic, and most aircraft were capable of supporting multiple instruments as part of their scientific payload.

High Arctic campaigns required large payloads, long endurance at low altitudes and the ability to mount large external cross-track antenna arrays for radars to successfully sound particularly challenging targets, such as the lower reaches of Jakobshavn Isbræ, Greenland. As was already well established from the earlier AIM/PARCA campaigns, the P-3 met these requirements and was most often deployed there. Antarctic operations required either a very long range aircraft based off-continent and capable of efficient high-altitude transit across the Southern Ocean (DC-8 or G-V), or a Short Takeoff and Landing (often ski-equipped) aircraft based from austere on-continent facilities (DC-3T). Alaska operations and Arctic summer campaigns usually deployed smaller, short-range platforms (e.g., DHC-3T, HU-25). Larger aircraft with longer ranges (e.g., P-3, DC-8) often required larger numbers of deployed personnel to meet crew duty rules and maximize scientific productivity. This requirement then had to be balanced against the additional cost and logistics of supporting more personnel at the available remote bases of operations suitable for efficient polar surveys. Further, limitations in aircraft availability created occasional exceptions to typically deployed aircraft for both Arctic and Antarctic campaigns.

Figure 6: Aircraft collage

Photographs of most aircraft deployed by OIB between 2009–2020. Credit: Jeremy Harbeck, except (d) Jefferson Beck, (g) Duncan Young, (h) Joseph MacGregor, (i) Nathan Kurtz, (k) Helen Cornejo, (l) Sander Geophysics and (m) Jack Holt.

Table 12: Key aircraft characteristics

Key characteristics of aircraft deployed by OIB.

Aircraft	Organization	Number of flights [a]	Median (maximum) time aloft (h) [b]	Median (maximum) range (km) [c]	Number of field personnel [d]
AS350-B3	CAS (Heli-Greenland)	8	N/A [e]	N/A [e]	8
B-200	NASA LaRC [f]	18	5.0 (6.1)	2194 (4147)	4–6
B-200T	CAS (Dynamic Aviation)	15	5.1 (7.8)	2144 (3060)	4–6
C-130H	NASA WFF [f]	42	8.0 (9.2)	3700 (4139)	20
Cessna-206	CAS (Keller Aviation)	13	5.0 (6.5)	900 (1200)	2
DC-3T	CAS (Airtec)	16	6.4 (8.2)	2010 (2575)	6–10
DC-3T	CAS (Kenn Borek)	109	6 (7)	1950 (2100)	8–9
DC-8	NASA AFRC [f]	155	11.1 (12.5)	7547 (9779)	>40
DHC-3T	CAS (Ultima Thule)	161	4.5 (6.0)	700 (1000)	4
G-V	NASA JSC [f]	30	10.0 (10.6)	7068 (8278)	20
G-V	NCAR	27	10.6 (11.8)	8334 (9310)	15
HU-25C	NASA LaRC [f]	33	3.7 (4.1)	2567 (2784)	10
HU-25A	NASA LaRC [f]	29	3.6 (4.0)	2154 (2682)	10
P-3	NASA WFF [f]	286	7.8 (10.1)	3661 (5330)	20–25
WP-3D	NOAA	16	7.8 (8.8)	3675 (4100)	25

[a] Total number of science flights during all OIB campaigns.

[b] Median time aloft with OIB payload during science flights, not including check flights or transits.

[c] Median distance traveled during OIB science flights, indicative but not definitive of maximum aircraft range when flying with typical OIB scientific payload in polar environments and a predetermined margin of safety. Note that payloads varied depending on the campaign (Tables 13–15).

[d] Approximate values only. Includes deployed air crew, instrument operators and ground-support crew.

[e] Values not available.

[f] NASA center abbreviations: Langley Research Center (LaRC); Wallops Flight Facility (WFF); Armstrong Flight Research Center (AFRC); Johnson Space Center (JSC).

5. Campaigns

5.1. Arctic

OIB flew 22 Arctic campaigns between 2009–2019 on nine different aircraft based from five different locations and using >20 instruments (Figure 7A; Table 14; Movie S1). During these campaigns, OIB flew 2,508 science flight hours, comprising 124 sea ice and 340 land ice science flights. During these campaigns, OIB flew 205,866 km of ICESat tracks, 56,912 km of ICESat-2 tracks, 30,748 km of CryoSat-2 tracks, 2,027 km of Envisat tracks and 3,776 km of Sentinel-3A/B tracks.

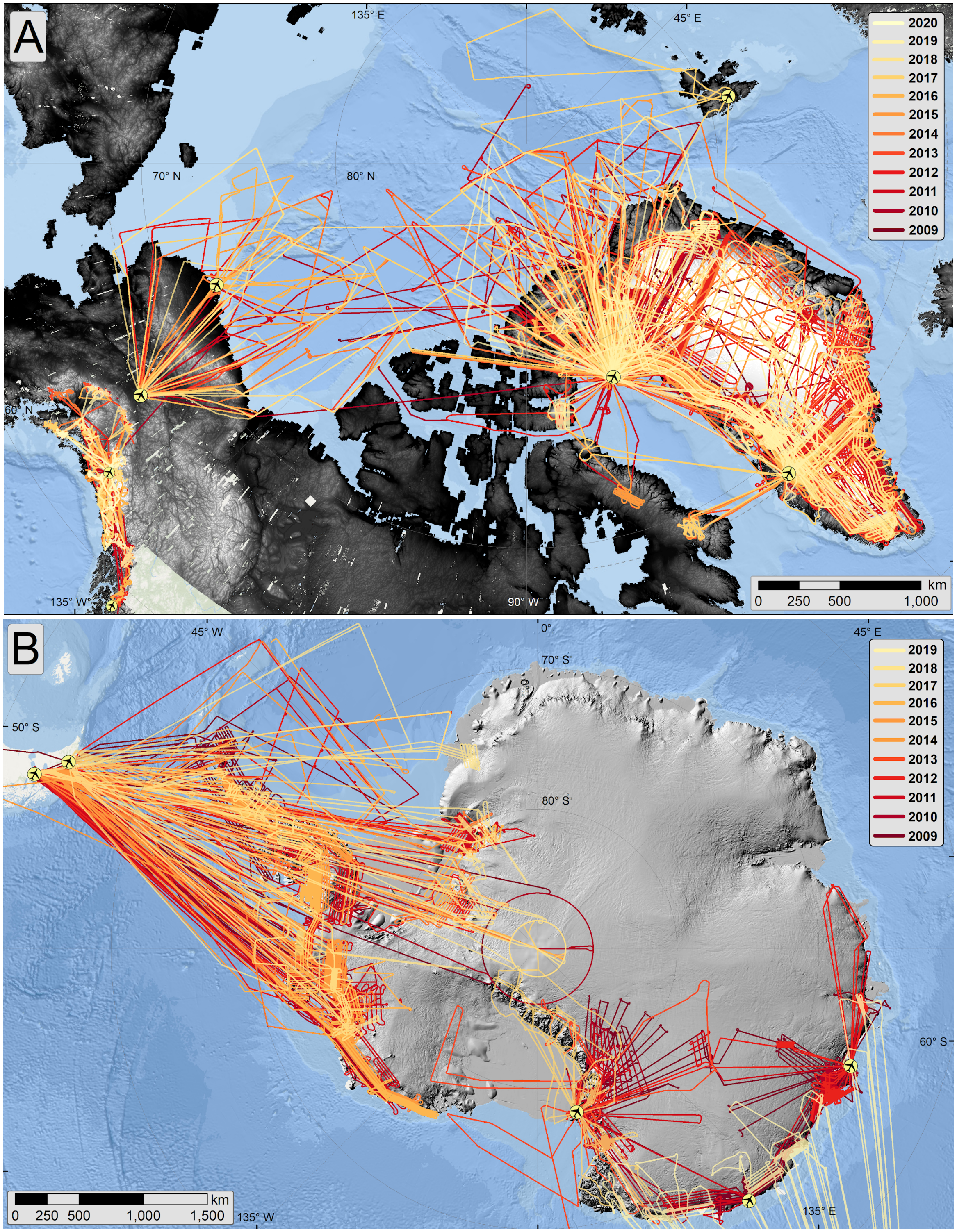

Figure 7: Flight maps

Flight lines and bases of operation for all of the OIB (A) Arctic and Alaskan campaigns and (B) Antarctic campaigns between 2009–2020, overlain on hillshaded DEMs(Porter et al., 2018; Howat et al., 2019). Panel A does not include 2016 AS350-B3 flight lines, and for clarity only shows Fairbanks, Utqiaġvik, Ultima Thule and Wrangell bases for Alaskan campaigns. Repeat flights are shown in the color of the most recent year flown. See Movies S1 and S2 for the annual evolution of each hemisphere's OIB campaigns in the same format as this figure.

Table 13: Arctic campaigns

Summary of key characteristics of OIB Arctic campaigns.

Year / Season	**Dates (MM/DD)**	**Bases [1]**	**Aircraft**	**Instruments flown [2]**	**Science flights (#) and data collection time flown (h) [3]**	**Underflight distance flown (km) [4]**
2009 / Spring	03/31–05/05	TG, KG, FA	P-3	ATM T2/T3, LVIS v1, PARIS, CAMBOT v1	*SI:* 6; *LI:* 14; *H:* 106	*IS:* 26467 *ES:* 2027
2010 / Spring	03/22–04/21	TG	DC-8	ATM T2/T3, LVIS v1, DMS v1, MCoRDS v3, AIRGrav, Snow v2, CAMBOT v1	*SI:* 8; *LI:* 6; *H:* 88	*IS:* 9365 *CS2:* 1342
	05/07–05/26	TG, KG	P-3	ATM T2/T3, MCoRDS v3, Snow v2, Accum v1, AIRGrav, DMS v1, CAMBOT v1	*LI:* 13; *H:* 67	*IS:* 3488
2011 / Spring	03/16–05/16	TG, KG, FA	P-3	ATM T3/T4, MCoRDS v3, Snow v3, Accum v1, AIRGrav, Scintrex CS-3, DMS v1, CAMBOT v1	*SI:* 10; *LI:* 27; *H:* 184	*IS:* 15040 *CS2:* 2059
	04/15–05/07	KG	B-200	LVIS v2, LVIS camera	*LI:* 18; *H:* 80	*IS:* 4934
	04/15–04/25	IL	DC-3T	Riegl LD-90	*LI:* 10; *H: 51*	N/A
2012 / Spring	03/14–05/17	TG, KG, FA	P-3	ATM T3/T4, MCoRDS v3, Accum v2, Snow v4, AIRGrav, Scintrex CS-3, DMS v1, CAMBOT v1, KT-19	*SI:* 14; *LI:* 29; *H:* 252	*IS:* 25372 *CS2:* 7752
	04/28–05/10	TG, KG	HU-25C	LVIS v2, LVIS camera	*SI:* 1; *LI:* 10; *H:* 51	*IS:* 5711
2013 / Spring	03/20–04/26	TG, KG, FA	P-3	ATM T3/T4, MCoRDS v3, Accum v2, Snow v4, DMS v1, CAMBOT v1, KT-19	*SI:* 11; *LI:* 15; *H:* 147	*IS:* 14966 *CS2:* 3462
2013 / Fall	10/31–11/14	TG, KG	C-130	LVIS v2, LVIS-GH, LVIS Camera	*SI:* 2; *LI:* 7; *H:* 52	*IS:* 2896 *CS2:* 2900
2014 / Spring	03/12–05/21	TG, KG, FA	P-3	ATM T3/T4, MCoRDS v3, Accum v2, Snow v4, DMS v2, CAMBOT v1, KT-19	*SI:* 13; *LI:* 33; *H:* 299	*IS:* 21767 *IS2:* 4266 *CS2:* 3175
2015 / Spring	03/19–05/15	TG, KG, FA	C-130H	ATM T3/T5, MCoRDS v4, Snow v4, DMS v2, CAMBOT v1, FLIR A325sc	*SI:* 10; *LI:* 23; *H:* 228	*IS:* 13332 *IS2:* 2365 *CS2:* 1292
2015 / Fall	09/23–10/22	TG, KG	HU-25C	ATM T5, DMS v2, FLIR A325sc	*SI:* 3; *LI:* 19; *H:* 72	*IS:* 6799 *IS2:* 1501 *CS2:* 215
2016 / Spring	04/19–05/19	TG, KG, FA	WP-3D	ATM T2, MCoRDS v5, Snow v4, DMS v2, FLIR	*SI:* 6; *LI:* 10; *H:* 102	*IS:* 7174 *IS2:* 1844 *CS2:* 699 *S3:* 738

2016 / Summer	07/13–09/15	UT, KG	HU-25A	ATM T5, DMS v2, CAMBOT v1, FLIR	*SI:* 6; *LI:* 17; *H:* 61	*IS:* 4613 *IS2:* 1518 *CS2:* 864
	07/26–08/09	NA, KU	AS350-B3	AIRGrav, Riegl LD-90	*LI:* 8; *H:* 70	N/A
2017 / Spring	03/09–05/12	TG, KG, FA, LS	P-3	ATM T5/T6, MCoRDS v3, Accum v3, Snow v6, iMAR/DgS, DMS v2, CAMBOT v1, FLIR, KT-19	*SI:* 13; *LI:* 27; *H:* 261	*IS:* 16580 *IS2:* 11545 *CS2:* 3225 *S3:* 2027
2017 / Summer	07/17–07/25	TG	HU-25A	ATM T5, DMS v2, FLIR	*SI:* 5; *LI:* 1; *H:* 14	N/A
	08/25–09/20	TG, KG	B-200T	LVIS-F	*LI:* 15; *H:* 87	*IS:* 5320 *IS2:* 5174
2018 / Spring	03/22–05/01	TG, KG, FA	P-3	ATM T6/T7, MCoRDS v3, Accum v3, Snow v6, DMS v2, CAMBOT v2, FLIR, KT-19, HW-Nano	*SI:* 8; *LI:* 12; *H:* 129	*IS:* 10595 *IS2:* 7324 *CS2:* 432 *S3:* 639
2019 / Spring	04/03–05/16	TG, KG	P-3	ATM T6/T7, MCoRDS v3, Snow v6, CAMBOT v2, FLIR, KT-19, HW-Co	*SI:* 6; *LI:* 18; *H:* 146	*IS:* 4909 *IS2:* 21054 *CS2:* 860 *S3:* 372
2019 / Summer	09/04–09/14	TG	G-V	ATM T6/T7, Snow v6, CAMBOT v2, FLIR, HW-Co	*SI:* 2; *LI:* 8; *H:* 46	*IS:* 2607 *IS2:* 5495

[1] Basing abbreviations: Thule Air Base, Greenland (TG), Kangerlussuaq, Greenland (KG), Ilulissat, Greenland (IL), Narsarsuaq, Greenland (NA), Kulusuk, Greenland (KU), Fairbanks, Alaska, United States (FA), Utqiagvik, Alaska, United States (UT), Longyearbyen, Svalbard, Norway (LS).
[2] Instrument abbreviations: snow radar (Snow), accumulation radar (Accum), FLIR A655sc (FLIR), Headwall Nano-Hyperspec (HW-Nano) and Co-Aligned VNIR-SWIR (HW-Co).
[3] Sea ice flights (SI), land ice flights (LI), science flight hours (H).
[4] ICESat (IS), ICESat-2 (IS2), EnviSat (ES), CryoSat-2 (CS2), Sentinel-3A/B (S3).

5.2. Antarctic

OIB flew 17 Antarctic campaigns between 2009–2019 on six different aircraft based from four different locations and using >25 different instruments (Figure 7B; Table 14; Movie S2). During these campaigns, OIB flew 1397 science flight hours, comprising 34 sea ice and 286 land ice science flights. This resulted in 80,254 km of ICESat tracks, 35,897 km of ICESat-2 tracks, 16,599 km of CryoSat-2 tracks, 532 km of Sentinel-3A/B tracks, and 3,710 km of TanDEM-X tracks.

Table 14: Antarctic campaigns
Summary of key characteristics of OIB Antarctic campaigns.

Year / Season	Dates [1] (MM/DD)	Bases [2]	Aircraft	Instruments flown [3]	Science flights (#) and data-collection time flown (h) [4]	Underflight distance flown (km) [5]
2009 / Fall	10/16–11/18	PA	DC-8	ATM T2/T3, LVIS v1, MCoRDS v1, Snow v1, AIRGrav, DMS v1, CAMBOT v1	*SI:* 3; *LI:* 18; *H:* 93	*IS:* 7952
	11/02–	MC, CS,	DC-3T	HiCARS v1, WISE, Riegl LD-	*LI:* 19; *H:* 101	*IS*: 12538

	02/16	DU, RO		90, BGM-3, Geometrics 823A		
2010 / Fall	10/26–11/20	PA	DC-8	ATM T2/T3, LVIS v2, MCoRDS v1, Snow v2, AIRGrav, DMS v1, CAMBOT v1	*SI:* 3; *LI:* 7; *H:* 35	*IS:* 3723 *CS2:* 2263
	10/20–02/26	MC, CS, DDU, RO, TL, MZ	DC-3T	HiCARS v1/v2, PCL, Riegl LD-90, Geometrics 823A	*LI:* 36; *H:* 62	*IS*: 19076 *CS2*: 729
2011 / Fall	10/12–11/19	PA	DC-8	ATM T3/T4, MCoRDS v1, Snow v3, AIRGrav, DMS v1, CAMBOT v1	*SI:* 5; *LI:* 19; *H:* 127	*IS:* 7820 *CS2:* 2417
	11/10–12/23	MC, CY, DU, CO	DC-3T	HiCARS v2, PCL, Riegl LD-90, BGM-3, ZLS, Geometrics 823A	*LI:* 20; *H:* 65	IS: 4959
	10/07–10/27	PA	G-V	LVIS v2, LVIS camera	*LI:* 11; *H:* 62	*IS:* 1352
2012 / Fall	10/12–11/07	PA	DC-8	ATM T3/T4, DMS v1, Snow v4, MCoRDS v1, AIRGrav, DMS v1, CAMBOT v1, KT-19	*SI:* 4; *LI:* 12; *H:* 64	*IS:* 1496 *CS2:* 2027
	11/10–01/26	MC, CS, BY	DC-3T	HiCARS v2, PCL, Riegl LD-90, GT-1A, Geometrics 823A	*LI:* 24; *H:* 127	*IS:* 1094
2013 / Fall	11/19–11/28	MC	P-3	ATM T3/T4, MCoRDS v1, Snow v4, Accum v2, AIRGrav, Scintrex CS-3, DMS v1, CAMBOT v1, KT-19	*SI:* 2; *LI:* 4; *H:* 43	*IS:* 2730 *IS2:* 134 *CS2:* 1768
2014 / Fall	10/16–11/22	PA	DC-8	ATM T3/T4, MCoRDS v2, Snow v4, AIRGrav, DMS v2, CAMBOT v1, KT-19	*SI:* 3; *LI:* 19; *H:* 105	*IS:* 6951 *IS2:* 1412 *CS2:* 3213
2015 / Fall	09/22–10/29	PA	G-V	LVIS v2, DMS v2	*SI:* 2; *LI:* 14; *H:* 142	*IS:* 5220 *CS2:* 854
2016 / Fall	10/14–11/18	PA	DC-8	ATM T5/T6, MCoRDS v2, Snow v4, AIRGrav, DMS v2, CAMBOT v1, FLIR	*SI:* 3; *LI:* 21; *H:* 107	*IS:* 4129 *IS2:* 5445 *CS2:* 3328
2017 / Fall	10/29–11/25	UA	P-3	ATM T6/T7, MCoRDS v3 Accum v3, Snow v6, AIRGrav, Scintrex CS-3, DMS v2, CAMBOT v1, FLIR, KT-19	*SI:* 4; *LI:* 7; *H:* 29	*IS2:* 2858 *TDX:* 3710
	11/29–12/16	MC	DC-3T	MCoRDS v6, Riegl LMS-Q240i	*LI:* 16; *H:* 99	*IS: 1158* *IS2: 533*
2018 / Fall	10/10–11/16	PA, UA	DC-8	ATM T6/T7, MCoRDS v2, Snow v6, AIRGrav, KT-19, CAMBOT v2, FLIR, HW-Nano	*SI:* 3; *LI:* 21; *H:* 87	*IS:* 56 *IS2:* 20991 *S3:* 532
2019 / Fall	10/23–11/20	HT	G-V	ATM T6/T7, MCoRDS v7, Snow v6, iMAR/DgS, CAMBOT v2, KT-19, HW-Co	*SI:* 2; *LI:* 18; *H:* 49	*IS2:* 4524

[1] Date range for science flights only.

[2] Punta Arenas, Chile (PA), Ushuaia, Argentina (UA), Hobart, Australia (HT), McMurdo Station (MC), Casey Station (CS), Dumont d'Urville Station (DU), Mario Zucchelli Station (MZ), Troll Station (TS), Concordia Station (CO), Rothera Station (RO), Byrd Surface Camp (BY).
[3] Instrument abbreviations: accumulation radar (Accum), snow radar (Snow), Headwall Nano-Hyperspec (HW-Nano) and Co-Aligned VNIR-SWIR (HW-Co).
[4] Sea ice flights (SI), land ice flights (LI), science flight hours (H).
[5] ICESat (IS), ICESat-2 (IS2), CryoSat-2 (CS2), EnviSat (ES), Sentinel-3A/B (S3), TanDEM-X (TDX).

5.3. Alaska

OIB flew 25 Alaskan campaigns between 2009–2020, mostly on single aircraft based from 14 different locations and using six different instruments (Figure 7A; Table 15; Movie S1). During a typical year, two separate campaigns were flown in May and then August to capture both interannual and melt-season elevation change across major Alaskan glaciers. During these campaigns, OIB flew 847 science flight hours, comprising 174 glacier flights, with no satellite underflights.

Table 15: Alaska campaigns
Summary of key characteristics of OIB Alaska campaigns.

Year	**Dates (MM/DD)**	**Bases** [1]	**Platform**	**Instruments flown** [2]	**Science flights (#) and time flown (h)** [3]
2009	05/22–06/02 08/19–09/06	CH, UL	DHC-3T	UAF Riegl	*LI*: 12; *H*: 54
2010	05/16–05/26 08/21–08/29	WR, MC, DE, UL, GS	DHC-3T	UAF Riegl	*LI*: 8; *H*: 59
2011	05/15–05/30 08/16–08/12	UL, YA, HA,	DHC-3T	UAF Riegl	*LI*: 18; *H*: 73
2012	03/16–03/25 05/24 08/14–08/30	PA, GU, UL, YA, MC, HA	DHC-3T	UAF Riegl, WISE	*LI*: 17; *H*: 87
2013	05/20–05/28 06/17–08/30	MC, YA, UL, PE, HA, PA, GU, CH	DHC-3T	UAF Riegl, UAF HF	*LI*: 15; *H*: 82
2014	05/13–05/24 08/19–08/23	UL, MC, CH, YA, HA, PA, SE	DHC-3T	UAF Riegl, UAF HF	*LI*: 12; *H*: 76
2015	05/15–05/22 08/20–08/29	MC, YA, UL, HA	DHC-3T	UAF Riegl, ARES, UAF HF	*LI*: 15; *H*: 72
2016	05/14–05/28 08/04–08/21	UL, PE, YA, MC, PA, SK, VA	DHC-3T	UAF Riegl, ARES, UAF HF	*LI*: 14; *H*: 67
2017	05/16–05/31 08/15–08/28	MC, YA, UL, SE, GU	DHC-3T	UAF Riegl, ARES, UAF HF	*LI*: 7; *H*: 39
2018	05/16–05/30 08/17–08/29	MC, UL, YA, GU, PA	DHC-3T	UAF Riegl, Snow v5, ARES	*LI*: 24; *H*: 64
2019	09/22–09/28	PA, VA, UL, MC, HA	DHC-3T	UAF Riegl, ARES	*LI*: 11; *H*: 35
2020	05/21–06/13	UL	DHC-3T	UAF Riegl, ARES	*LI*: 8; *H*: 48
	05/29–06/13	MC, PA, YA, PE, GS	Cessna-206	Riegl VQ-580ii	*LI*: 13; *H*: 91

[1] Basing abbreviations (all locations within Alaska, United States): Palmer (PA), Valdez (VA), Ultima Thule Lodge (UL), McCarthy (MC), Haines (HA), Yakutat (YA), Gulkana (GU), Seward (SE), Petersburg (PE), Skwentna (SK), Chitina (CH), Wrangell (WR), Denali National Park (DE), Gustavus (GS).
[2] Instrument abbreviations: Riegl LMS-Q240i (UAF Riegl), UAF HF Radar Sounder (UAF HF).

[3] Land ice flights (LI), science flight hours (H).

6. Outcomes

6.1. Land ice

6.1.1. Elevation change

6.1.1.1. Arctic

Mapping ongoing elevation change of land ice in the Arctic – especially along the margins of Greenland Ice Sheet – formed a primary element of NASA's airborne studies of the cryosphere prior to OIB (e.g., AIM/PARCA). Collecting such observations remained a core scientific requirement for OIB (Table 1) that the mission met by measuring surface elevation with laser altimetry during 247 repeat or near-repeat flights over Arctic land ice in 11 years (231 over Greenland Ice Sheet and peripheral Greenlandic glaciers and ice caps, 16 over ice caps in the Canadian Arctic Archipelago). Numerous studies either made use of OIB surface-elevation data alone, combined them with pre-OIB NASA airborne data, or combined them with surface-elevation measurements from ICESat or other satellite altimeters (e.g., CryoSat-2).

Csatho et al. (2014) produced the most comprehensive assessment of early OIB (through 2012) elevation-change measurements across Greenland Ice Sheet (Figure 8). They combined OIB data with pre-OIB airborne (1993–2008) and satellite observations (2003–2009) and found a complex pattern of outlet-glacier retreat that defied binary categorization (e.g., thinning or thickening) as these records lengthened. Although many glaciers only experienced thinning, particularly along the northwestern coast, others experienced dramatic inter- or multi-annual thinning/thickening cycles, particularly along the southeastern coast of Greenland. Northern Greenland outlet glaciers were either stable or thinning slowly prior to 2012, but this pattern soon changed and northeastern glaciers began to thin rapidly, likely in response to ocean forcings, as partly documented by OIB elevation measurements (Khan et al., 2014; Mouginot et al., 2015, 2018, Kehrl et al., 2017). In the early 2010s, overall Greenland Ice Sheet mass loss accelerated, reaching more than 400 Gt yr^{-1} by some estimates that leveraged OIB surface-elevation measurements directly (e.g., Mouginot et al., 2019; IMBIE Team, 2020), but this rate then moderated by about one third. Greenland's peripheral glaciers and ice caps have received somewhat less attention, but OIB observations also directly informed assessments that their mass balance is significantly negative, likely due to a markedly negative surface mass balance at their lower elevations as compared to Greenland Ice Sheet proper (Colgan et al., 2015; Noël et al., 2017). OIB observations of Canadian ice caps demonstrated that rates of mass loss there are accelerating, attributed mostly to a rapidly warming Arctic atmosphere (e.g., Gardner et al., 2012; Colgan et al., 2015; Schaffer et al., 2020).

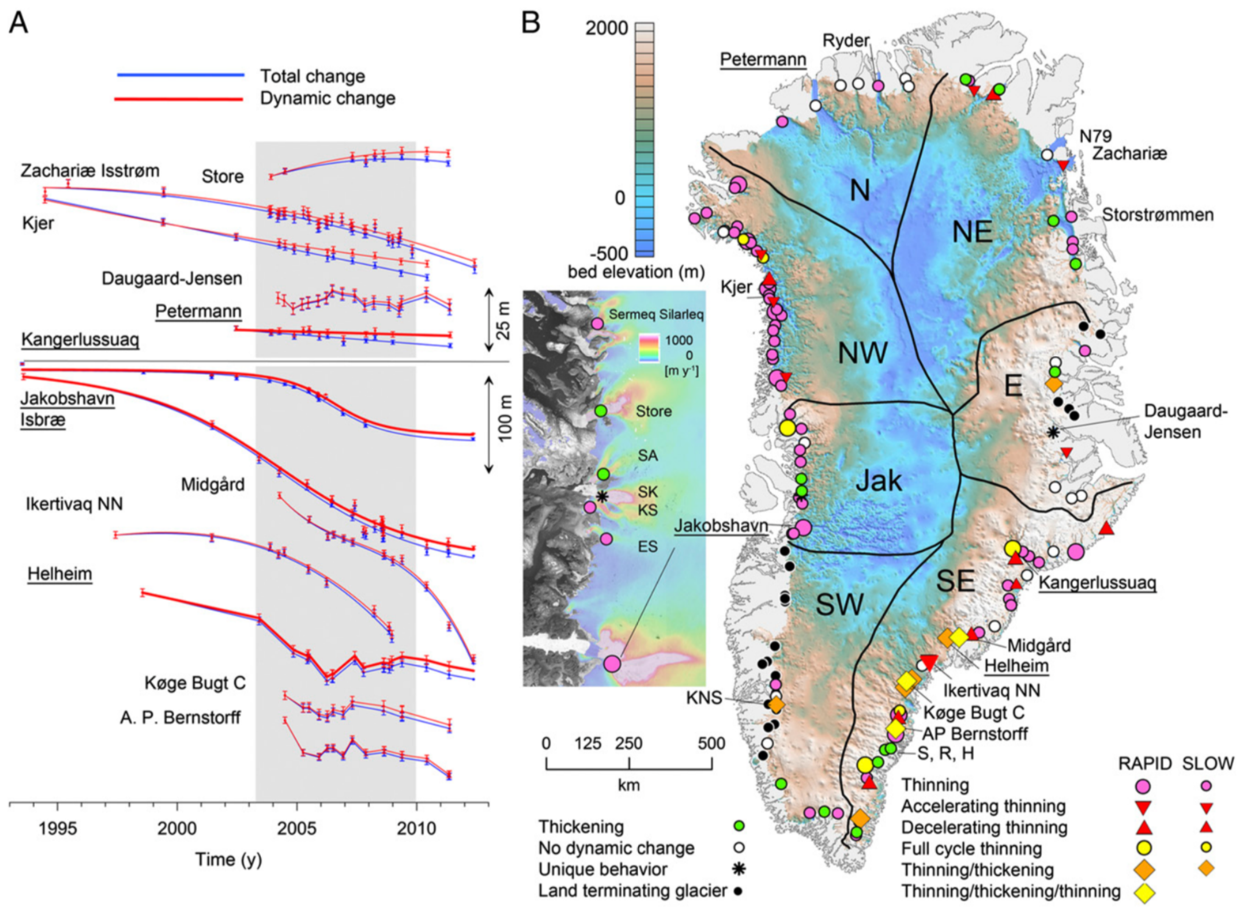

Figure 8: Greenland elevation change

Classification of outlet glaciers based on pattern of dynamic elevation change. (A) Elevation change from the combined ICESat, ATM and LVIS altimetry record (1993−2012) illustrating different outlet glacier behaviors. Gray box marks ICESat mission duration, and glacier locations are shown in B. (B) Distribution of different outlet glacier behavior types overlain on bed topography. Inset shows the detailed pattern north of Jakobshavn Isbræ overlain on ice velocity. Adapted from Csatho et al. (2014).

Multiple studies focused on the surface-elevation change of individual large outlet glaciers using OIB data (e.g., Kehrl et al., 2017; Khazendar et al., 2019; Joughin et al., 2020). Beyond large-scale interannual thickness changes, OIB measurements of surface-elevation change enabled a wider variety of analyses that improved our understanding of the Earth system in the Arctic. Sutterley et al. (2014a) and Khan et al. (2016) used ATM data to improve understanding of glacial isostatic rebound in Greenland, which is essential to constrain so that ice-sheet mass-balance estimates from satellite gravimetry can be reconciled with other methods. Sutterley et al. (2018) demonstrated that OIB's occasional repeat measurements of surface elevation during the Arctic summer campaigns enable direct evaluation of regional climate model (RCM) outputs. Because detailed ground-truth data from the summer ablation season remains limited, this novel use of intra-year OIB surveys filled a critical gap by informing how RCMs could be improved to better capture seasonal surface mass balance. Finally, OIB altimetry data also helped identify the first evidence of recharge of a subglacial lake from surface meltwater (Willis et al., 2015).

6.1.1.2. Antarctic

Because of its size and difficulty of access, the Antarctic Ice Sheet posed a greater challenge for OIB than the Greenland Ice Sheet. Rather than taking a gap-filling approach – as was done for the Greenland Ice Sheet – the more achievable aim was to repeat both new and legacy survey tracks primarily targeted at rapidly changing glaciers and ice shelves across the Amundsen Sea Embayment and the Antarctic Peninsula, with additional repeat observations at Totten Glacier, Denman Glacier and Cook Ice Shelf in East Antarctica. OIB's laser altimeter observations, often used in conjunction with satellite-observed elevations, enabled detailed mass-balance estimates of specific sectors of Antarctica, insight into newly discovered processes and validation for other elevation products. The latter includes products such as CryoSat-2 DEMs (e.g., Helm et al., 2014; Slater et al., 2018) and the Reference Elevation Model of Antarctica (Howat et al., 2019). The fine precision and spatial resolution of OIB repeat measurements were also crucial in confirming elevation changes inferred from CryoSat-2 measurements on Thwaites Glacier that were likely associated with the drainage of a network of subglacial lakes (Smith et al., 2017).

Because of an initial survey focus on the Amundsen Sea Embayment, the earliest OIB altimetry results focused on that region's glaciers. Medley et al. (2014) and Sutterley et al. (2014b) used ATM and LVIS data, in conjunction with altimetry from the ICESat mission, to develop a time series of mass change. Both studies found that – by the early 2010s – mass loss from this sector had tripled since the mid-1990s. These results demonstrated that OIB surveys were sufficient to fill the altimetry gap following ICESat, which was further supported by the clear consistency of the results using several independent techniques (input–output, altimetry and gravity; Sutterley et al., 2014b).

For the Larsen C ice shelf, analysis of ice-shelf thickness changes derived from both OIB and pre-OIB ATM data (typically spanning the mid-2000s to mid-2010s) found that it was relatively stable and that atmospheric processes drove a significant portion of the observed changes there (Sutterley et al., 2019; Figure 9). In contrast, other West Antarctic ice shelves are thinning rapidly due to oceanic forcing (e.g., Wilkins, Pine Island, Dotson and Crosson). Walker and Gardner (2017) and Friedl et al. (2018) used related data and techniques to investigate the dynamics of the Fleming Glacier after the retreat and disintegration of Wordie Ice Shelf, finding increased dynamic thinning and ocean-driven grounding-line retreat. In East Antarctica, satellite-observed glacier thinning of Totten and Denman glaciers was confirmed by OIB measurements, as was the relative stability of the ice streams draining into Cook Ice Shelf (Young et al., 2015). ATM data was also critical for confirming the fastest drainage of an Antarctic subglacial lake observed to date, which occurred in 2014 beneath Slessor Glacier, East Antarctica (Siegfried and Fricker, 2018).

Multiannual compilations of elevation-change data derived from OIB laser altimetry, combined with ICESat data and pre-OIB ATM measurements, have been an important validation dataset for modeling studies, particularly in the Amundsen Sea Embayment. Such studies have explored the sensitivity of Pine Island Glacier models to submarine melt or the choice of basal friction model (Joughin et al., 2010, 2019), and demonstrated that Thwaites Glacier has likely started to collapse through the marine ice-sheet instability (Joughin et al., 2014). In each case, the similarity of modeled and observed elevation change was used to argue that the model could predict glacier evolution during the observation period, increasing confidence in its prognostic capabilities. Similarly, studies of the Dotson and Crosson ice shelves have demonstrated that present ice-shelf acceleration and grounding-line retreat is likely a consequence of ocean-driven ice-shelf thinning (Lilien et al., 2018). Gridded elevation-change data from OIB were also used to investigate the sensitivity of post-glacial rebound in the Amundsen Sea Embayment to the thinning history of its glaciers, finding an unusually weak crust that rebounds faster might slow retreat there in the coming decades (Barletta et al., 2018).

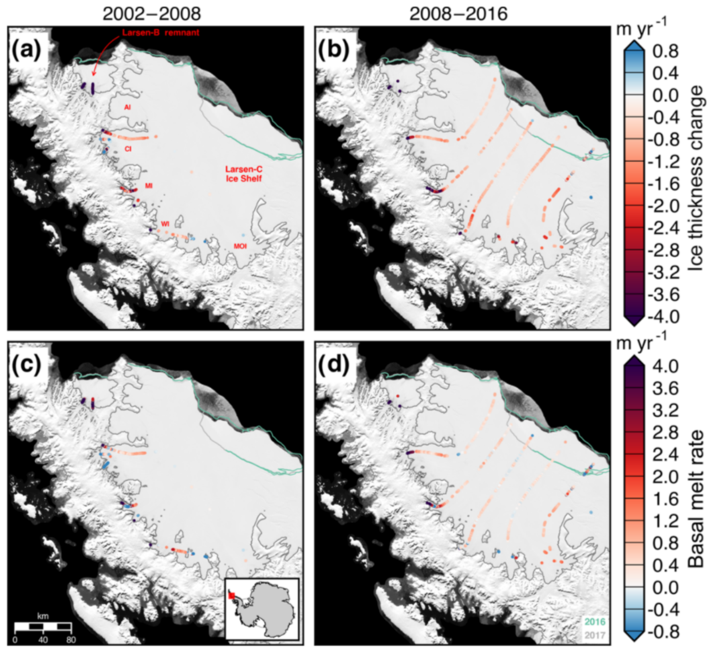

Figure 9: Larsen C thickness change

(a,b) Ice-thickness change and (c,d) and estimated basal melt rates of the Larsen B (remnant) and Larsen C ice shelves for 2002–2008 and 2008–2016, respectively. AI, CI, MI, WI, and MOI denote the Adie, Cabinet, Mill, Whirlwind, and Mobiloil inlets, respectively. Grounding line denoted in gray. Adapted from Sutterley et al. (2019).

Several studies leveraged the nature of the ATM elevation measurement itself, which does not penetrate significantly through snow, to account for the variable signal penetration of satellite radar altimeters. Groh et al. (2014) used the along-track height changes derived from ATM data over Thwaites Glacier to estimate that radar altimeters typically penetrate ~5 m into firn. This estimate permitted the development of a longer, multi-mission time series of volume change using both ICESat and TanDEM-X, which indicated increased mass loss from Thwaites Glacier during the 2000s. However, Rott et al. (2018) compared ATM data and TanDEM-X DEMs and found that radar penetration into the snow was negligible within their study area across the outlet glaciers that drain into the former Larsen A and B embayments. This spatially variable radar-altimeter penetration suggests that further analysis of OIB laser-altimetry measurements is essential to synthesize radar- and laser-altimetry data. This need was further emphasized by Schröder et al. (2019), who produced multi-mission estimates of Antarctic ice-sheet surface-elevation change from ICESat and six different satellite radar altimeters. Adusumilli et al. (2018) similarly benefitted from the independent validation made possible by the OIB altimetry record when deriving a 23-yr record of elevation change for Antarctic Peninsula ice shelves using four radar altimeters. By comparing the radar-altimetry elevation-change time series with that derived from four separate OIB surveys over the Larsen C Ice Shelf, they confirmed that the results were not affected by inter-mission biases. These multi-mission studies, combining both satellite and airborne altimetry, were the first to document that the nearly decade-long increase in surface elevation of that ice shelf at the beginning of OIB's lifetime was driven by atmospheric processes (i.e., cooler conditions, less melt, increased firn air content).

Separately, LVIS elevation measurements circumnavigating the South Pole were used to estimate inter-campaign biases for ICESat (Hofton et al., 2013). These biases were applied to the ICESat elevation data to improve elevation accuracy and then estimate ice-sheet mass balance (e.g., Nilsson et al, 2015; Martin-Español et al., 2017; Ciraci et at., 2018), glacial isostatic adjustment (Sasgen et al., 2018), and snow accumulation (Shu et al., 2018).

6.1.1.3. Alaska

During the OIB era, Alaskan glaciers continued to thin rapidly and lose mass, a further indication of their persistent imbalance with the present climate. Larsen and others (2015) conducted repeat surveys of the surface elevations of over one hundred Alaskan glaciers between 1994–2013 and found that most land-terminating glaciers were thinning across most of their elevation range, and their mass loss accounted for most of the ongoing Alaskan glacier mass loss (75 ± 11 Gt yr^{-1}; Figure 10). In contrast, elevation change across dynamic tidewater glaciers was significantly more variable and accounted for only ~6% of the mass loss during this period. This straightforward apportionment of elevation-change hypsometries by glacier type enabled the clear conclusion that a strongly negative surface mass balance is primarily responsible for the ongoing retreat of Alaskan glaciers. The airborne laser altimetry data collected by Larsen et al. (2015) also permitted assessment of DEM quality in challenging mountainous regions (Trüssel et al., 2017; Berthier et al., 2018).

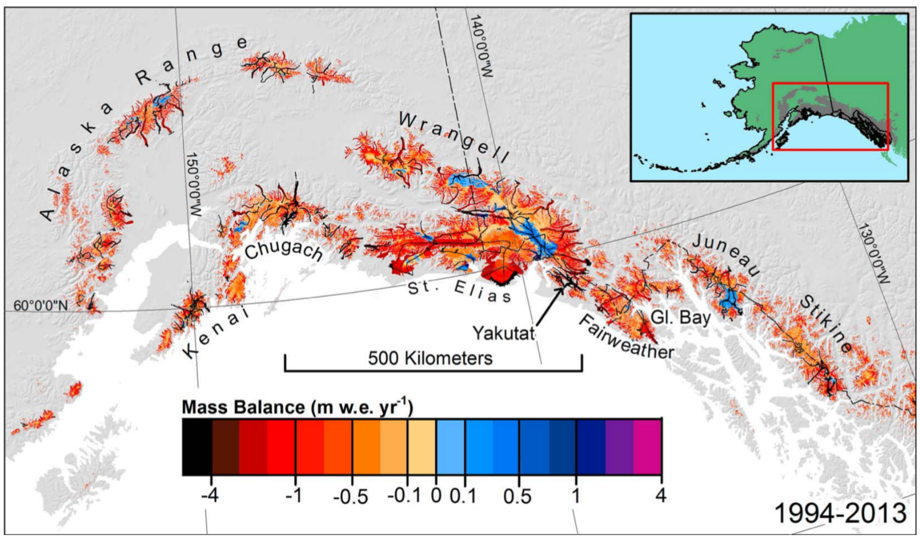

Figure 10: Alaska mass balance
Estimated mass balance for surveyed and unsurveyed glaciers between 1994–2013 in the most densely glacierized region of Alaska. Black lines indicate survey flights. Adapted from Larsen et al. (2015).

6.1.2. Ice thickness and bed topography

Measurements of glacier and ice-sheet thickness are essential for estimates of total ice volume and for reliable interpretation of their flow because their driving stress depends strongly on ice thickness and their bed topography influences their response to downstream dynamic perturbations (Cuffey and Paterson, 2010; Felikson et al., 2020). As such, a major component of most of OIB's Arctic, Antarctic and Alaskan campaigns over land ice included ice-thickness measurements of previously unsurveyed terrain using radar sounders (Table 1; §3.2). Such surveys were sometimes designed as stand-alone flights, but most were designed to meet multiple science requirements, e.g., to also measure surface elevation along historic ICESat or future ICESat-2 ground tracks or to measure across snow accumulation rates where RCMs disagreed (e.g., southeastern Greenland).

Similar to airborne measurements of surface-elevation change, the primary utility of ice-thickness measurements lies not in the data collected during any single flight, but through the compilation of the measurements made during each campaign's individual flights, each mission's campaigns spanning multiple years, and each institution's missions – often spanning decades. These compilations result in comprehensive views of the bed topography beneath Earth's two remaining ice sheets that directly inform our understanding of both their history and models of their future (e.g., Bamber et al., 2013a; Fretwell et al., 2013). For both the Greenland interior and some of the most vulnerable portions of the Antarctic ice sheet, OIB substantially increased the quantity and coverage of ice-thickness measurements, with contributions from nearly all of the deployed deep radar sounders (Figure 11). Similar benefits were realized with OIB surveys of Alaskan glaciers and the Canadian Arctic Archipelago (e.g., Van Wychen et al., 2013, 2015; Rignot et al., 2013; Soso et al., 2021).

Early during the lifetime of OIB, it was recognized that commonly applied geostatistical techniques for these compilations (e.g., ordinary kriging) were inadequate to model ice flow at high resolution, because they could induce non-physical artifacts within model domains (Seroussi et al., 2011). Morlighem et al. (2011) introduced a mass-conservation method that reconciled satellite-mapped surface speeds with inherently sparser ice-thickness measurements from airborne radar sounding. Combined with OIB data, this method directly addressed concerns with interpretation of ongoing rapid changes in Greenland and Antarctic outlet glaciers, where ice thickness is hardest to measure but of greatest importance to the ice sheets' future (Morlighem et al., 2014; Rignot et al., 2014). Recent compilations leverage a great deal of OIB data and reveal – at unprecedented resolution – the many subglacial troughs that extend into the interiors of the Greenland and Antarctic ice sheets from their grounding zones (Morlighem et al., 2017; 2019; Figure 11). For the Greenland Ice Sheet, this improved bed topography translated directly into improved representation of its present flow and more reliable projections of its present and future mass balance under continued anthropogenic warming (Aschwanden et al., 2016, 2019; Mouginot et al., 2019). With the first-order geometry now better constrained, OIB radar-sounding data continue to provide new insight into smaller topographic features that could impact future projections of ice-sheet evolution (e.g., Parizek et al., 2013; MacKie et al., 2020).

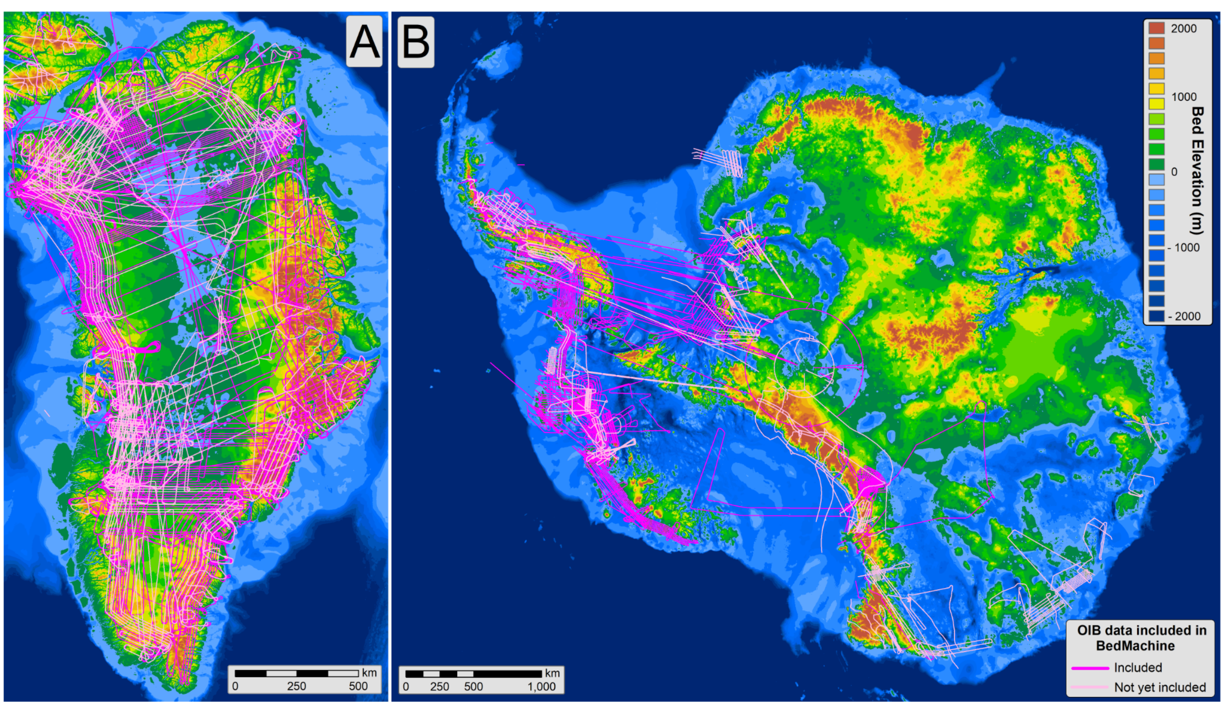

Figure 11: Ice-sheet bed topography

Bed topography beneath the (A) Greenland and (B) Antarctic ice sheets, overlain with OIB flights where deep radar sounder data were collected. Grids shown are BedMachine Greenland v3 and BedMachine Antarctica v2, respectively (Morlighem et al., 2017, 2019), and line colors denote whether these OIB measurements have already been incorporated in those data products. For panel A, note that OIB surveys of Svalbard and part of the Canadian Arctic Archipelago are not shown.

OIB VHF radar-sounding data also advanced investigations into the potential for swath mapping of the bed topography beneath polar ice (also known as radar tomography). The years immediately prior to OIB saw several investigations using airborne campaigns to evaluate the feasibility of ground-based and airborne swath radar sounding of ice sheets (e.g., Paden et al., 2010; Jezek et al., 2011). Jezek et al. (2013) further advanced this possibility using a fine-resolution OIB survey from near the ice margin of southwestern Greenland Ice Sheet, which showed that even data not collected using techniques more ideal for swath mapping (e.g., beam steering) could still be used to produce swath images of the bed that were compatible with ice thickness inferred purely from nadir-sounding measurements. In 2014, OIB surveyed glaciers and ice caps in the Canadian Arctic Archipelago more extensively using swath mapping to better interpret their boundary conditions and dynamics (Hamilton, 2016; Medrzycka et al., 2019; Van Wychen et al., 2020). Later, in both 2018 and 2019, MCoRDS data collected over Arctic land ice (mostly the Greenland Ice Sheet) steered the transmitted beam across-track and are expected to further advance investigations of fine-scale bed topography in a manner similar to other recent airborne surveys (e.g., Holschuh et al., 2020).

Despite the challenges of flying low-frequency radars on fixed-wing aircraft, such systems emerged as a valuable complement to higher-frequency radars, because they are better suited to temperate and high-scatter (water-rich) ice masses. Rignot et al. (2013) found that with WISE, temperate Alaskan glaciers up to 1200 m thick can be sounded with low-frequency radar sounders, and that bed reflections can be detected in both the ablation and accumulation zones of all surveyed glaciers. The interpretation of airborne radar data in mountainous topography remains challenging due to substantial surface clutter. However, comparison against clutter simulations can enable unambiguous identification of the ice–bed reflection (e.g., Enderlin et al., 2016; Holt et al., 2006, 2019). Some larger Alaskan glaciers are less susceptible to surface clutter, e.g., a number of deep channels were identified beneath Malaspina Glacier (Truffer et al., 2016), which will be important for projecting its retreat.

6.1.3. Fjord and sub-ice-shelf bathymetry

In the years immediately prior to OIB, the bathymetry of ice-sheet-adjacent fjords in Greenland and sub-ice-shelf cavities in Antarctica was increasingly recognized as a critical factor modulating access of warmer ocean masses to ice fronts or grounding zones (e.g., Rignot and Jacobs, 2002; Holland et al., 2008). In both Greenland and Antarctica, glacially eroded submarine troughs enable rapid delivery of deep water from the continental shelf into fjords or ice-shelf cavities, whereas sills can limit those intrusions. In Greenland, intrusions of warmer deep Atlantic water masses into fjords are the primary concern (e.g., Straneo et al., 2011; Mortensen et al., 2013; Rignot et al., 2016; Catania et al., 2018, 2020; Porter al., 2014, 2018; Schaffer et al., 2020), whereas in Antarctica modified circumpolar deep water within sub-ice-shelf troughs that reach the grounding zone is the greater concern (e.g., Morlighem et al., 2019; Millan et al., 2020).

Mapping this bathymetry at large scales is challenging due to the presence of ice mélange in Greenlandic fjords and thick (tens of meters to more than a kilometer) ice shelves in Antarctica, combined with the present operational limits of underwater autonomous vehicles in ice-covered seas. To address this challenge, OIB regularly collected high-accuracy airborne gravity data to infer both fjord and sub-ice-shelf bathymetry (Tinto and Bell, 2011; Cochran and Bell, 2012; Schodlok et al., 2012; Muto et al., 2013; Cochran et al., 2015, 2020; Boghosian et al., 2015; Tinto et al., 2015; Greenbaum et al., 2015; An et al., 2017, 2019; Millan et al., 2017, 2018, 2020; Wei et al., 2020, Constantino et al., 2020). These studies variously combined OIB gravity data from airborne (both fixed-wing and helicopter) surveys with information from other sources because bathymetric inferences from gravity data alone are non-unique. The primary additional dataset that was employed was radar-sounding measurements of ice thickness collected concurrently with the gravity data by OIB. Other ancillary datasets included direct measurements from ship-borne multi-beam echo sounding surveys (e.g., An et al., 2017; Millan et al., 2017, 2018), syntheses of ice thickness and bed topography on grounded ice, especially near the grounding zone (e.g., Morlighem et al., 2019), aeromagnetic data to constrain geologic effects on the gravity signal (e.g., Tinto and Bell, 2011; Greenbaum et al., 2015; Boghosian et al., 2015), and ground-based seismic surveys (e.g., Muto et al., 2013).

During the course of OIB, gravity inversion evolved from two-dimensional inversions with limited constraints into three-dimensional inversions with multiple independent constraints. This advance resulted in the first syntheses of bed topography that are both continuous and reliable within grounding zones, which is particularly important for ice-sheet models. Many fjords and ice-shelf cavities were mapped for the first time with OIB, replacing either geostatistical interpolation within glacially carved fjords or an arbitrarily set fixed water-column thickness beneath ice shelves, respectively. Improved bathymetry enabled greater fidelity for simulations of ocean circulation in these environments, providing new insights into the impact of ocean thermal forcing on glaciers and ice shelves, and their impact on ice-sheet evolution (e.g., Schodlok et al., 2012; Millan et al., 2020).

OIB bathymetric inferences were combined with other international efforts into regional and subsequently continental compilations of subglacial and submarine bed topography (e.g., Rignot et al., 2014, 2015, 2016; Morlighem et al., 2017, 2019; Figure 11). In particular, in Greenland OIB data were merged with bathymetry and gravity data acquired by Oceans Melting Greenland (OMG), a companion NASA airborne mission that surveyed many Greenland fjords and the surrounding continental shelf using multibeam echo sounding and airborne gravity (e.g., An et al., 2018). Corrections to prior compilations often resulted in water hundreds of meters deeper than previously assumed. In several cases, these corrections transformed previously inferred shallow fjords into deep ones (southeastern Greenland), or ice shelves overlying subglacial ridges into ones floating over deep submarine troughs (parts of the Amundsen Sea Embayment).

OIB data enabled a generational change in our understanding of the topography both beneath and adjacent to ice sheets for the regions surveyed. That included all major Greenland fjords and dozens of minor ones from the combination with OMG, nearly all West Antarctic ice shelves east of the Ross Ice Shelf, and several East Antarctic ice shelves along Wilkes Land. Combining both instruments and analyses that simultaneously enable on- and off-ice topographic mapping is now well recognized as essential to interpreting the effect of ocean-forced changes along the vulnerable margins of both ice sheets (e.g., Morlighem et al., 2017, 2019).

6.1.4. *Snow accumulation and firn compaction*

Measuring ice-sheet mass balance requires knowledge of both snow accumulation and firn compaction, yet our understanding of them is limited because satellite-based remote sensing of these processes remains challenging. Thus, *in situ* measurements of both processes form the large majority of our knowledge base, despite their limited coverage in both space and time (Benson, 1996; Favier et al., 2013; Montgomery et al., 2018). Ground-based radar sounding expanded our ability to map modern snow accumulation rates across hundreds of kilometers (e.g., Spikes et al., 2004; Hawley et al., 2014), providing more representative values for mass-balance studies (Richardson et al., 1997), but the higher-frequency radar sounders deployed by OIB ultimately resulted in a generational leap in measuring snow-accumulation rates (§3.2.3).

Because of its wide bandwidth, the snow radar detected subsurface horizons at sub-decimeter vertical resolution (Table 9), enabling mapping of annual accumulation rates across both Antarctica and Greenland (Medley et al., 2013; Koenig et al., 2016; Dattler et al., 2019; Montgomery et al., 2020; Figure 12). These studies mapped horizons that reflect seasonal changes in firn density, effectively eliminating the costly need for auxiliary depth–age information from snow pits or ice cores once validated. In regions of significant surface melting, where the subsurface stratigraphy is altered after snow deposition, Kuipers

Munneke et al. (2017) and de la Peña et al. (2015) were still able to map wintertime snow-accumulation rates across the Larsen C Ice Shelf and the western Greenland Ice Sheet ablation zone, respectively. At more coarsely resolved periods (tens of years), investigations of OIB accumulation radar data provide a centennial-scale perspective on snow-accumulation trends and variability across the Greenland Ice Sheet (e.g., Karlsson et al., 2016; Lewis et al., 2017).

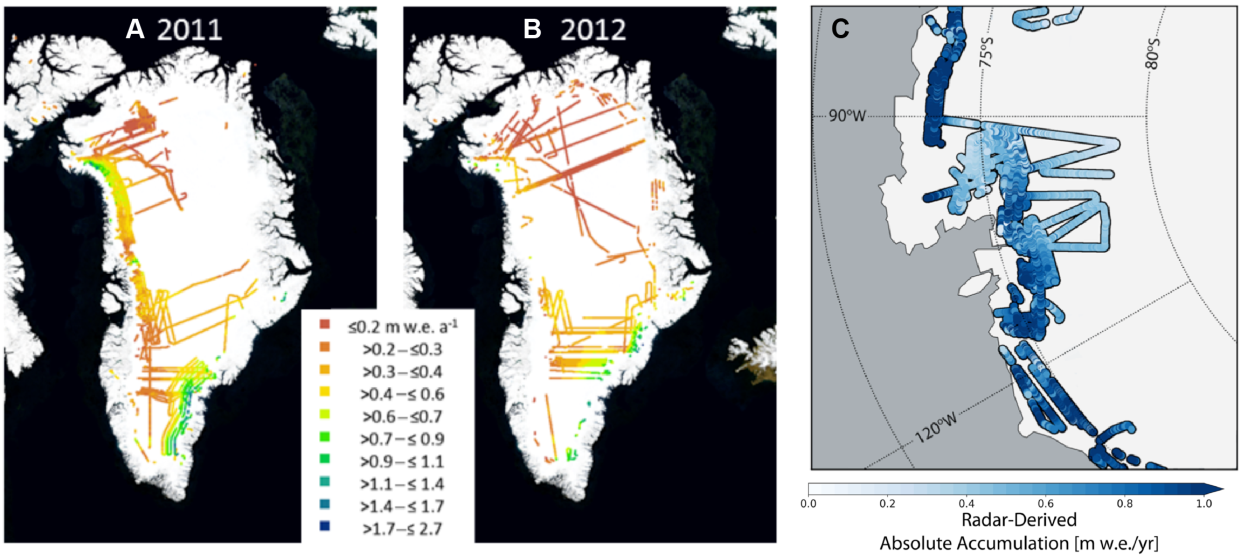

Figure 12: Ice-sheet snow accumulation

(A,B) Annual snow-accumulation rate across the Greenland Ice Sheet derived from OIB snow radar for 2011 and 2012, respectively. (C) Multi-annual mean snow-accumulation rate across the West Antarctic Ice Sheet derived from 2010–2017 OIB snow radar. Adapted from Koenig et al. (2016) and Dattler et al. (2019), respectively.

The shallow (snow) or intermediate-depth (accumulation) radar sounders were used extensively to evaluate and improve the ability of both global climate models and RCMs to reproduce spatiotemporal variability in ice-sheet snow-accumulation rates. Prior to OIB, such evaluations were limited to *in situ*, static observations (e.g., Lenaerts et al., 2012). Since then, several OIB datasets have become critical and common evaluators for these models (e.g., Lenaerts et al., 2018; van Wessem et al., 2018; Agosta et al., 2019). Van de Berg and Medley (2016) determined that one RCM could better represent observed interannual variability in snow accumulation rates by applying an upper-atmospheric relaxation. A comparison with the results from Medley et al. (2013) revealed this limitation, for which van de Berg and Medley (2016) developed a standard to evaluate possible improvements and ultimately changed model implementation in subsequent runs of that RCM, with others ultimately also implementing this relaxation (Mottram et al., in press).

Although not yet as robustly studied, firn-compaction rates are arguably more challenging to measure remotely, and so few observations exist at scales relevant to present RCMs (tens of kilometers). OIB shallow radar sounders provided a unique opportunity to evaluate the use of repeat airborne measurements to measure firn-compaction rates. Medley et al. (2015) determined that repeat-track OIB snow radar data were of sufficient quality (especially after 2010) to estimate firn-compaction rates across Thwaites Glacier and that these rates varied substantially at small length (<6 km) and time scales (annually). A tandem study by Ligtenberg et al. (2015) provided the first large-scale evaluation of a firn-densification model using those radar-derived compaction rates, which indicated overall good model performance at RCM-relevant scales. Those pilot studies suggest that future firn-modeling efforts would benefit from further refinement and investigation of OIB snow radar data.

6.1.5. Ice-sheet hydrology

OIB data generated top-to-bottom insights into ice-sheet hydrology via remote inferences of the presence of liquid water, subsequent refreezing, and improved accuracy and coverage of surface and basal topography for subglacial hydrology models. Detection of changes in brightness temperature or backscatter from passive microwave satellites provide reliable, spatiotemporally dense observations of meltwater presence or production (e.g., Tedesco et al., 2007; Trusel et al., 2013). However, those measurements do not readily indicate the fate of that meltwater, which can infiltrate and refreeze within a permeable firn column, remain liquid as an aquifer or run off an impermeable ice surface. The importance of those processes to ice-sheet mass balance only increased during OIB's lifetime. By sensing just below the surface, OIB data provided the basis for several discoveries regarding the fate and consequences of surface meltwater.

Surface meltwater on the Greenland Ice Sheet often forms supraglacial lakes, particularly along the southwestern coast in the percolation zone (e.g., Echelmeyer et al., 1991; Box and Ski, 2007). These lakes are readily detected by satellites, and some drain rapidly and modulate ice flow (e.g., Selmes et al., 2011; Andrews et al., 2018). It was generally assumed that most supraglacial lakes either froze or drained englacially during the wintertime. However, using OIB snow radar data, Koenig et al. (2015) found that some supraglacial lakes are buried by snow and remain liquid throughout the winter. While the volume of water in buried supraglacial lakes is insignificant compared to the present total mass loss of the Greenland Ice Sheet, this water can influence local englacial temperature, the development of englacial channels, and ice dynamics (e.g., Law et al., 2020).

Using accumulation radar data collected across the Greenland Ice Sheet, Forster et al. (2014) discovered a perennial firn aquifer in ~800 km of 40,000 km of 2011 OIB flights along flight lines originally designed to improve upon poor knowledge of the bed topography in low-elevation regions (Figure 13A). This facies had never been identified at such a large scale before, but when combined with RCM outputs and *in situ* observations, they determined that substantial summer snowfall (>0.8 m water-equivalent yr^{-1}) was necessary to insulate this meltwater from colder winter temperatures. As for radar observations of snow accumulation, these firn-aquifer observations constituted an opportunity for novel evaluation of RCMs, especially their snow and firn models. Forster et al. (2014) and Miège et al. (2016) only reported the depth to the top of the firn aquifer, because the accumulation radar signal is significantly attenuated by the presence of liquid water, limiting penetration to the water table. Chu et al. (2018) used lower-frequency MCoRDS data to constrain the thickness of firn aquifer by evaluating the difference between the observed bed-echo power and that modeled assuming no firn aquifer was present, which was assumed to be due to the additional attenuation of the radar signal due to the thickness of the firn aquifer. They inferred that the firn-aquifer thickness was typically 4–25 m and changes significantly interannually due to variability in surface melt rates. Coincident ATM observations demonstrated that there may be an observable surface-elevation change associated with variability in firn-aquifer thickness, suggesting spaceborne monitoring of this thickness (and not only extent) may be possible.

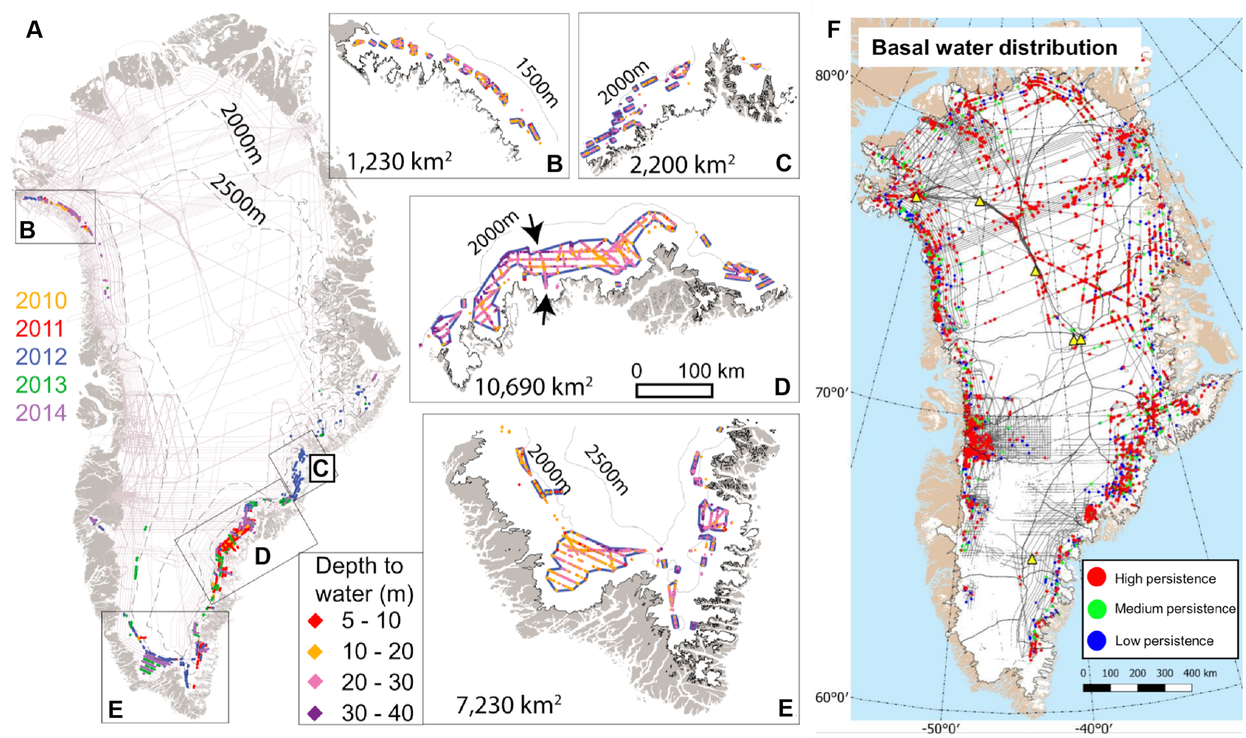

Figure 13: Greenland firn aquifer and basal water extent

(A) Extent of perennial firn aquifer and (B–E) depth to the top of the aquifer inferred from OIB accumulation radar data. Adapted from Miège et al. (2016). (F) Extent and persistence of basal water beneath the Greenland Ice Sheet inferred from MCoRDS data. Adapted from Jordan et al. (2018).

Most of the liquid water that infiltrates the firn column refreezes, because local climate conditions do not support aquifer formation (i.e., lower accumulation and melt rates). OIB accumulation radar observations of refrozen layers within the firn column, in conjunction with Earth system models, indicate that ice slabs within the firm column of the Greenland Ice Sheet are becoming more prevalent and moving farther inland (MacFerrin et al., 2019). Firn models will need to incorporate this discovery, as the increased spread of near-surface slabs will increase the volume of surface meltwater production that becomes runoff.

Improved accuracy and coverage of ice-sheet surface and bed elevation from OIB data also resulted in improved understanding of the connection between subglacial hydrology and ice-shelf processes. Dow et al. (2018) combined ATM and other data with a global DEM to build a new DEM of the Nansen Ice Shelf in Antarctica. They then used this hybrid DEM to determine how surface meltwater is routed over the ice shelf and the nature of basal channels at the ice–ocean interface. Schroeder et al. (2019) used OIB radar sounding from Filchner-Ronne Ice Shelf with context from historical radar-sounding data to infer multi-decadal stability of Möller Ice Stream's subglacial hydrologic system. Alley et al. (2016) also investigated ice-shelf basal channels with OIB radar sounding, suggesting they are prone to fracture and significant structural weakening of the ice shelf. By leveraging OIB data with other datasets, these studies were able to illuminate new processes that govern overall ice-shelf (in)stability.

OIB also enabled numerous investigations of the nature of the subglacial hydrologic system, in particular the nature and distribution of subglacial water detected primarily via surface-elevation change and radar sounding. Fricker et al. (2014) extended the ICESat record of active subglacial lakes beneath the Recovery Ice Stream using ATM and evaluated the subglacial hydropotential using ice thickness measurements from MCoRDS. They found that the subglacial hydrologic system there is driven largely by bedrock topography and is relatively stable, which is a substantially different configuration from that beneath the ice streams that feed the Ross Ice Shelf. OIB/ICECAP radar data from East Antarctica highlighted the paradoxical reflectivity and specularity differences between stable radar-identified lakes in the ice-sheet interior and the altimetry-identified active lakes toward its periphery, which are typically unremarkable in radar-sounding data (Wright et al. 2014; Young et al. 2016). For the Greenland Ice Sheet, multiple distinct analyses of the reflectivity of the ice–bed reflection detected by MCoRDS variously revealed its large-scale distribution of basal water and the seasonality thereof (Jordan and et al., 2017, 2018; Livingstone et al., 2017; Chu et al., 2016, 2018; Oswald et al., 2018; Bowling et al., 2019; Figure 13F).

6.1.6. Ice-sheet internal structure and history

Since the 1970s, it has been well recognized that radar sounders can not only measure ice thickness efficiently, but that they can also detect internal reflections hundreds of meters to kilometers deep within ice sheets (e.g., Gudmandsen, 1975; Whillans, 1976). NASA airborne surveys of Greenland Ice Sheet prior to OIB also detected such reflections, which directly informed our understanding of the ice sheet's millennial-scale accumulation-rate, basal melt and ice-flow history (e.g., Fahnestock et al., 2001a,b; Baldwin et al., 2003; Legarsky and Gao, 2006). OIB continued and significantly expanded upon this legacy by virtue of its extensive coverage across both the Greenland and Antarctic ice sheets with more advanced radar sounders.

OIB's extensive radar sounding of the Greenland Ice Sheet made it possible to quantitatively assess and directly trace the nature of deep internal layering of the majority of a terrestrial ice sheet for the first time (Karlsson et al., 2013; Sime et al., 2014; MacGregor et al., 2015a; Figure 14). Direct tracing was done primarily using MCoRDS data and similar data from predecessor instruments (§3.2.1), which was possible due to the overall dataset quality and consistency in processing, coupled with extensive surveying of new terrain. The quality of these data has also motivated further investigation into automated layer-tracing methods (e.g., Panton and Karlsson, 2015). Shallower internal reflections detected in both OIB MCoRDS and accumulation radar data were used by multiple studies to infer centennial- to millennial-scale accumulation-rate and ice-flow patterns in ever-finer detail, particularly across central and northern Greenland, where internal reflections tend to be easier to detect (Nielsen et al. 2015; Karlsson et al., 2016; MacGregor et al., 2016a; Lewis et al., 2017; Florentine et al., 2018). Also using MCoRDS data, Bell et al. (2014) revealed the detection of widespread complex bed-emanating reflections and inferred that they were due to basal freeze-on of subglacial water or internal deformation, but their origin remains debated based on evaluation of similar and newer data (Dahl-Jensen et al., 2013; Wolovick et al., 2014; MacGregor et al., 2015a; Bons et al., 2016; Leysinger-Vieli et al., 2019;). MacGregor et al. (2015b, 2016a,b) showed that MCoRDS data can also be used to constrain ice-sheet temperature and Holocene flow history, and to locate regions of high apparent basal melting.

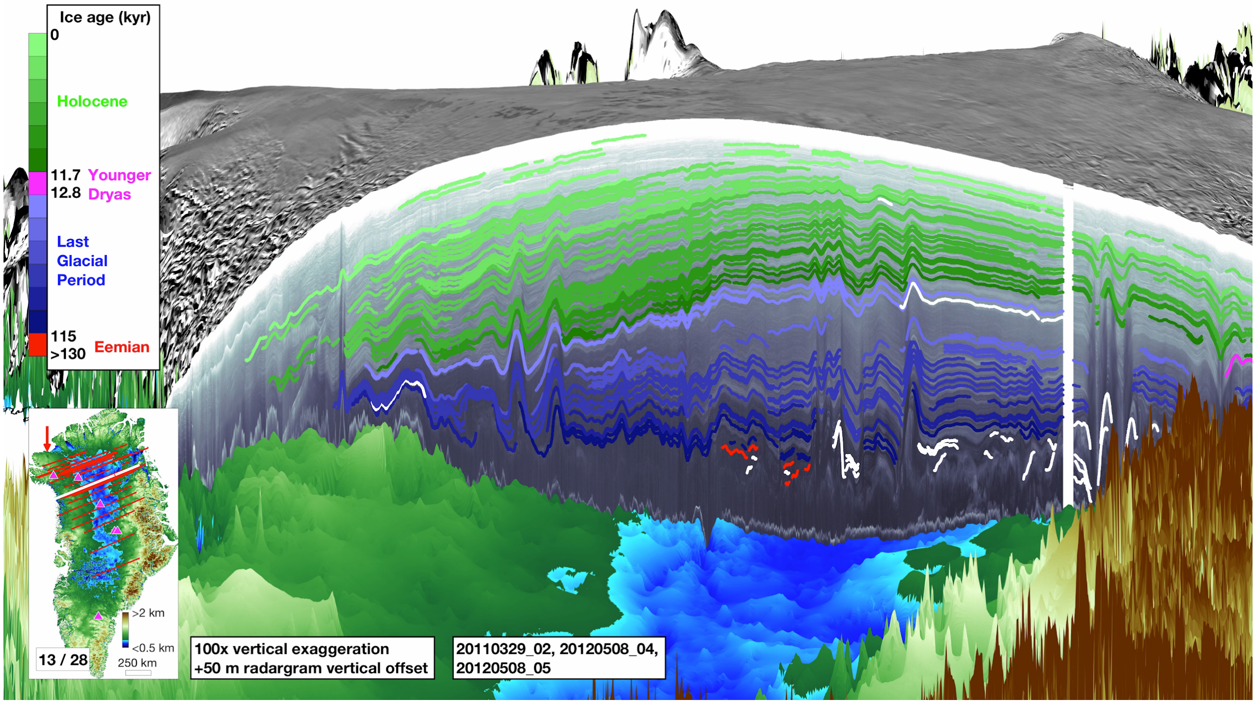

Figure 14: Greenland age structure

Age structure of the northern Greenland Ice Sheet, based on MCoRDS data, overlain on BedMachine v3 bed topography. The cross-section is the white line on the inset map. Traced layers are colored by their age following the color bar on the left. Adapted from Kjær et al. (2018) and distributed under a CC BY-NC 4.0 License (https://creativecommons.org/licenses/by-nc/4.0/).

OIB surveys of the Antarctic ice sheet are inherently more limited compared to those of the Greenland Ice Sheet, due to the sparser relative coverage of the former. However, a handful of studies made use of MCoRDS and HiCARS data to both map and interpret East Antarctic radiostratigraphy, whether between ice cores or families of radar sounders (e.g., Cavitte et al., 2016; Winter et al., 2017), and more recently West Antarctic radiostratigraphy observed by MCoRDS has been combined with earlier surveys (Bodart et al., in press).

6.1.7. Unanticipated discoveries

As with all polar airborne missions flying across uncharted terrain with new or upgraded instruments, numerous unanticipated discoveries were made with OIB data that went well beyond the original science goals of the mission or its specific science requirements (Table 1, Table 2, Table A2). For land ice, the majority of these discoveries pertained to the subsurface, typically either the top few tens of meters or the bedrock topography.

In Greenland, multiple fundamental discoveries concerning the nature of firn and the percolation zone were enabled by OIB's shallow radar sounders (snow and accumulation radars). Water-saturated firn aquifers were discovered in southeastern Greenland early during OIB's lifetime, and their extent and thickness along the margin of Greenland Ice Sheet were subsequently mapped (e.g., Forster et al., 2014; Miège et al., 2016; Chu et al., 2018; Miller et al., 2020; §6.1.5). At higher elevations, MacFerrin et al. (2019) mapped the surprisingly rapid evolution of the extent of ice "slabs" in the percolation zone from OIB accumulation radar data, which limit the ability of firn to buffer sea-level rise due to increasing meltwater runoff. OIB data also helped detect the current location and depth of the long-abandoned ice-sheet base at Camp Century in northwestern Greenland (Colgan et al., 2016).

Because the introduction of MCoRDS onboard the P-3 at the beginning of OIB represented a generational improvement in the quality of deep radar sounders (§3.2.1.1), several unanticipated discoveries were made concerning the nature of deep ice within the Greenland Ice Sheet. Highlights include the discovery of widespread, disturbed basal layers by Bell et al. (2014), which motivated substantial additional research into the processes controlling their formation (e.g., Wolovick et al., 2014; Leysinger-Vieli et al., 2018), and evidence for widespread Holocene flow deceleration (MacGregor et al., 2016a). Multiple unexpected subglacial and submarine features in Greenland were also discovered thanks to OIB and earlier NASA data, including a subglacial canyon rivaling the Grand Canyon in length and depth (Bamber et al. 2013b), two large subglacial impact craters beneath the northwestern Greenland Ice Sheet (Kjær et al., 2018; MacGregor et al., 2019), numerous subglacial lakes where few were previously known (Palmer et al., 2013; Bowling et al., 2019), a paleolake basin near Camp Century (Paxman et al., 2021), the asymmetry of the Petermann fjord (Tinto et al., 2015), and that many fjords into which major outlet glaciers discharge were several hundred meters deeper than previously assumed (e.g., An et al., 2017; Morlighem et al., 2017; Millan et al., 2018). An unusual hypersaline subglacial lake beneath the Devon Ice Cap was also identified in part via OIB surveys (Rutishauser et al., 2018). For Greenland's few remaining ice shelves, MCoRDS even proved capable of mapping large-magnitude changes in ice-shelf thickness, an unanticipated capability indicative of the rapid changes ongoing in the cryosphere, particularly at ice–ocean interfaces (e.g., Mouginot et al., 2015; Münchow et al., 2016).

In Antarctica, unanticipated instrument capabilities were similarly recognized, including measuring ice-shelf thickness changes using MCoRDS in the Amundsen Sea Embayment (Khazendar et al., 2016) and the ability to measure firn-compaction rates using snow radar (Medley et al., 2015). An early finding in under-surveyed regions was the presence of large inland subglacial fjords in the Aurora Subglacial Basin, indicating a dynamic phase for the early East Antarctic Ice Sheet (Young et al., 2011). Complementary gravity and magnetic data constrained the long-term erosional behavior of this margin and constrained the deep-time geologic assembly of Antarctica (Aitken et al., 2014, 2016a,b; Frederick et al., 2016). OIB data also played a key role in identifying a massive subglacial valley network that hosts one of Antarctica's largest subglacial lakes in Princess Elizabeth Land (Jamieson et al., 2016), and one of the deepest trenches in the world beneath the Denman Glacier (Brancato et al., 2020; Morlighem et al., 2019), where important glacier changes are ongoing in a basin that hosts a sea-level-equivalent volume of 1.5 m. Generally speaking, OIB revealed that the subglacial channels beneath major glaciers were often hundreds of meters deeper than previously known from sparse surveys and simple interpolation across data gaps. These gaps were essential to fill, because the deep bedrock often discovered in them rendered the glaciers far more sensitive to climate forcing and more prone to rapid retreat than otherwise assumed. Conversely, OIB data revealed sectors protected from a strong oceanic influence by shallow ridges, e.g., across the Transantarctic Mountains (Morlighem et al., 2019).

6.2. Sea ice

OIB sea ice flights generally surveyed the western Arctic Ocean north of Greenland and the Canadian Arctic Archipelago (within the Canada Basin, and the Chukchi and Beaufort seas) and the southwestern Southern Ocean (primarily the Weddell and Amundsen/Bellingshausen seas) (Figure 7). Sea ice flights typically occurred at or soon after the end of each hemisphere's respective winter growth season, when sea ice is near its maximum thickness, i.e., March or April in the Arctic (Table 13) and October or November in the Antarctic (Table 14). These focus areas balanced aircraft range, base accessibility, regional coverage, *in situ* overflights and satellite underflights. In 2017, OIB also surveyed sea ice in the eastern Nansen Basin, north of Svalbard, and in 2019 sea ice off the coast of Wilkes Land, East Antarctica. The first fall campaign over sea ice occurred in October and November of 2013 with a t high altitude survey over the Lincoln Sea using LVIS. In later years, summer/fall melt season campaigns in the Arctic were also conducted at the OIB-nominal AGL over both the Lincoln Sea and the Chukchi/Beaufort seas with ATM

(Table 14). In September 2019, ATM and snow radar were flown together for the first time during a summer campaign.

Planning of sea ice flights considered both near-real-time CryoSat-2 sea ice thickness data (http://www.cpom.ucl.ac.uk/csopr/seaice.html) and fine-resolution sea ice forecasts provided by the Naval Research Laboratory's Arctic Nowcast/Forecast System to ensure that OIB surveyed ice of varying age, thickness and surface roughness. Whenever possible, OIB surveys over sea ice included near-coincident satellite underflights (mostly CryoSat-2), coordinated flights with ESA's CryoSat-2 Validation Experiment (CryoVEx) airborne campaigns, and overflights of related *in situ* surveys (e.g., snow-thickness measurements).

These annual surveys enabled continued monitoring of the state of Arctic sea ice following a decade of rapid declines in sea ice extent and thickness (Comiso et al., 2008; Haas et al., 2008; Kwok and Rothrock, 2009). In particular, OIB measurements (especially freeboard and snow thickness) were valuable in monitoring sea ice thickness and for validating satellite retrievals thereof (Figure 15). OIB's snow thickness measurements from snow radar constituted a major advance as they allowed large-scale mapping of both first-year and multi-year snow and ice thickness over sea ice for the first time. This combination made it possible to monitor sea ice thickness annually across large portions of the western Arctic Ocean (e.g., Farrell et al., 2012; Kurtz and Farrell, 2011; Kurtz et al., 2013; Richter-Menge and Farrell, 2013), and to produce the first multi-year examination of variability in the Weddell Sea ice cover (Kwok and Kacimi, 2018).

6.2.1. Freeboard

Sea ice freeboard is the elevation of the sea ice surface above the local sea level. Freeboard measurements can be used to infer sea ice thickness assuming hydrostatic balance and local estimates of sea ice density, snow thickness and snow density (e.g., Giles et al., 2007; Kurtz et al., 2009; Kwok et al., 2009; Figure 15). The elevation of the air–snow interface above the local sea level is commonly referred to as the snow freeboard (also known as the total freeboard), while the elevation of the snow–ice interface above the local sea surface is the ice freeboard.

Several methods for determining sea ice freeboard from OIB data have been developed (Connor et al., 2013; Farrell et al., 2011, 2015; Kurtz et al., 2009, 2013; Kwok et al., 2009; Yi et al., 2014; Wang et al., 2013, 2016). All generally involved differencing the local sea-surface elevation from the sea ice elevation determined from ATM measurements. The ATM returns over sea ice are expected to track the air–snow interface with minimal penetration into any snow cover, meaning that the derived freeboards represent the snow freeboard, typical of laser altimetry (Giles et al., 2007). Lead locations were identified primarily with coincident visible imagery. Specifically, Kurtz et al. (2013) used the Sea-Ice Lead Detection Algorithm using Minimal Signal (SILDAMS) algorithm applied to DMS imagery to classify and locate leads and co-locate these with ATM elevation data (Onana et al., 2013). Leads are used to determine local sea surface elevation for calculating freeboard. The SILDAMS algorithm was applied to several campaigns and its results were distributed together with snow and sea ice thickness estimates (Kurtz et al., 2014). Other lead-classification methods used a combination of ATM elevation, reflectivity and waveform parameters on a shot-by-shot basis (Yi et al., 2014), or using ATM elevation and reflectivity histograms (e.g., Kwok et al. 2012; Kwok and Maksym, 2014). These alternative methods for locating leads were also assessed using contemporaneous visible imagery (DMS or CAMBOT).

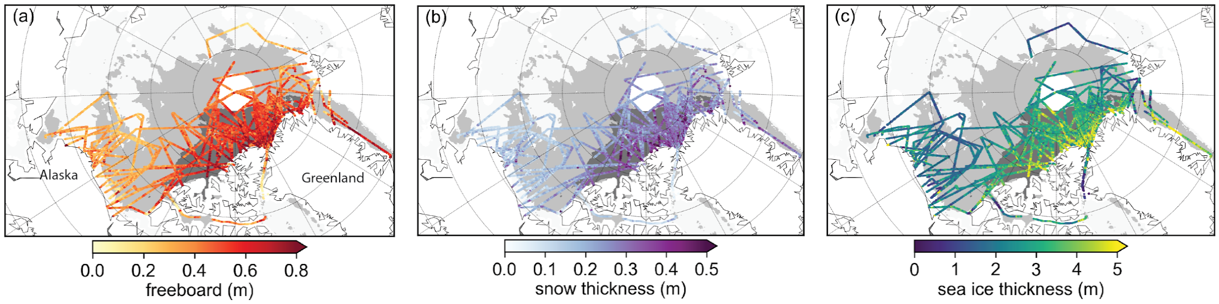

Figure 15. Arctic sea ice climatology

Mean snow freeboard, snow thickness and ice thickness of Arctic sea ice from the 2009–2019 Spring OIB campaigns using a combination of final (2009–2012, IDCSI4) and quicklook data (2013–2019) data. Background shading shows the persistent multi-year (dark gray), mixed multi-year/first-year (gray) and persistent first-year (light gray) ice regimes from the 2009–2019 1 April Ocean and Sea Ice Satellite Application Facility (OSI SAF) ice type product.

The spatial patterns of Arctic snow (total) freeboard mapped by OIB confirmed previous studies: higher freeboards are generally found over the deformed multi-year sea ice north of Greenland and lower freeboard are found over first-year ice in the Beaufort and Chukchi seas (Richter-Menge and Farrell, 2013; Kwok et al., 2012). Antarctic surveys showed higher freeboards in the western Weddell Sea and lower freeboards in the seasonal ice farther from the coasts in both the eastern Weddell and Bellingshausen seas (Kwok and Makysm, 2014; Wang et al., 2016; Kwok and Kacimi, 2018).

Arctic sea ice freeboard measured by OIB was used extensively to assess trends in and the quality of freeboards from satellite laser and radar altimeters, including ICESat (Connor et al., 2013; Kwok et al., 2012), ICESat-2 (Kwok et al., 2019), CryoSat-2 (Laxon et al., 2013, Kurtz et al., 2014; Kwok and Cunningham, 2015; Sallila et al., 2019; Yi et al., 2019) and AltiKa (Armitage et al., 2015). ATM-derived freeboards have also been compared with freeboards generated by less commonly used OIB instruments, including LVIS (Yi et al., 2014).

6.2.2. Snow thickness

Snow on sea ice modulates the growth and melt of sea ice because of its insulating and reflective properties, so that it plays an important role in modulating polar climate (Maykut and Untersteiner, 1971; Webster et al., 2018). Knowledge of the snow thickness on sea ice is also essential for inferring the thickness of sea ice from freeboard observations (e.g., Laxon et al., 2013). Prior to OIB, knowledge of the regional distribution and interannual variability of snow thickness was poor across both the Arctic and Southern Oceans. Between 2009–2019, OIB repeatedly flew a snow radar during its campaigns, enabling the first contemporary basin-scale estimates of snow thickness on sea ice (Farrell et al., 2012; Kurtz and Farrell, 2011; Kwok et al., 2011, 2017).

Multiple algorithms were developed to infer snow thickness from OIB snow radar data (Kwok et al., 2017). Each takes a different approach to determining the range to the air–snow and snow–sea-ice interfaces, to addressing inherent challenges associated with variability of the snow layer, and to compensating for system limitations (e.g., noise and resolution). These algorithms included: 1. The original reference algorithm developed by the OIB PSO for the 2009–2013 Arctic spring campaigns (Kurtz et al., 2013, 2015). This algorithm accounted empirically for inter-campaign differences in snow radar SNR but did not account for the effect of sidelobes, so it was replaced in 2015 with a waveform-fitting algorithm (Kwok et al., 2017). 2. A "quicklook" algorithm also generated by the OIB PSO for the 2012–2019 Arctic spring campaigns (Kurtz et al., 2014); 3. The snow radar layer detection algorithm (Koenig et al., 2016); 4. A wavelet-based algorithm (Newman et al., 2014); 5. An algorithm developed at the Jet Propulsion

Laboratory (Kwok and Maksym, 2014); and 6. The Support Vector Machine supervised learning algorithm (Holt et al., 2015).

These products tend to show good agreement in the regional snow-thickness distribution but can exhibit large inter-product differences at more local scales (Kwok et al., 2017; Figure 16). In general, all products produce the thickest snow on thick, multiyear ice north of Greenland and in the Lincoln Sea, with thinner snow over thinner, first year ice (e.g., in the Chukchi and Beaufort seas). The derived snow thicknesses compare favorably against in-situ field observations from various campaigns (e.g., Farrell et al., 2012; Webster et al., 2014; Newman et al., 2014; King et al. 2015).

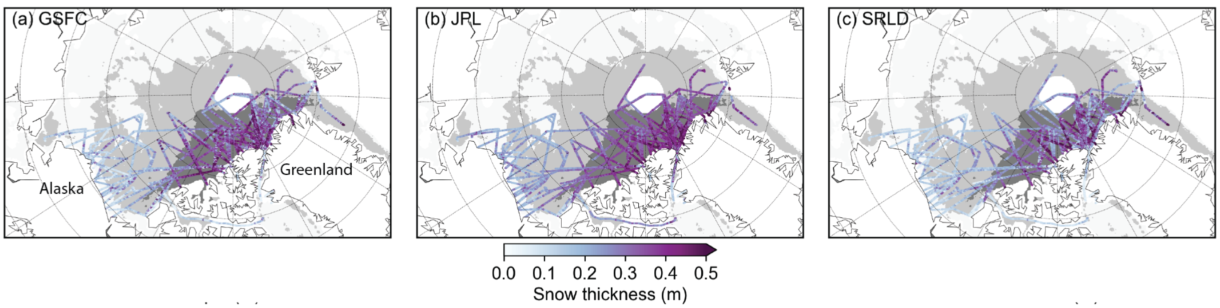

Figure 16. Snow thickness on Arctic sea ice
Arctic snow thickness inferred from snow radar data collected during OIB's 2009–2015 spring campaigns produced by three different algorithms (Kwok et al., 2017). Map format follows Figure 15.

OIB-derived snow thicknesses have been used extensively to assess snow-thickness reconstructions and models (Blanchard-Wrigglesworth et al., 2015, 2018; Petty et al., 2018). The efficacy of algorithms developed to estimate snow thickness on sea ice, based on, for example, differences between CryoSat-2 and SARAL/AltiKa altimeter returns (Guerreiro et al., 2016), or passive microwave radiometer retrievals (Brucker and Markus, 2013; Maaß et al., 2013; Rostosky et al., 2018) have been tested using a range of coincident OIB snow thickness observations. Compared to the existing climatology for the 1950s–1980s (Warren et al., 1999), both OIB and *in situ* observations indicate that snow thickness has decreased overall in the western Arctic at the end of winter, potentially due to later sea ice formation in the autumn and the shift from multi-year to first-year ice (Webster et al., 2014). OIB observations also confirmed that during the same period, snow on first-year ice is thinner than that on multi-year ice (Kurtz and Farrell, 2011; Blanchard-Wrigglesworth et al., 2015; Kwok et al., 2017).

Arctic OIB snow-thickness products were included in the State of the Arctic Report, which was initiated by NOAA's Climate Program Office in 2006, to establish an annual baseline of Arctic environmental conditions. The sea ice chapter relies on a suite of remote-sensing data to assess the state of the Arctic sea ice at the end of winter, and a compilation of OIB snow thickness measurements collected between 2009–2015 (not including 2013) were included in the 2017 Arctic Report Card (Perovich et al., 2017). These observations showed that mean snow thickness on Arctic sea ice range between 5–55 cm.

OIB snow radar data were also collected across the Southern Ocean, mainly in the Weddell and Bellingshausen seas, resulting in the first large-scale assessment of Antarctic snow and sea ice thickness. However, inferring snow thickness over Antarctic sea ice is generally considered more challenging, due to unique conditions including extensive ice deformation, seawater flooding, snow–ice formation and meltwater refreezing (e.g., Kwok and Maksym, 2014; Massom et al., 2001; Stammerjohn and Maksym, 2017). These processes conspire to challenge identification of the two key interfaces of interest (air–snow and snow–ice), resulting in larger uncertainties in derived snow thicknesses (Kwok and Maksym, 2014). Despite these challenges, Kwok and Maksym (2014) and Kwok and Kacimi (2018) produced snow-thickness estimates in the Weddell and Bellingshausen seas and found thicker snow along the western

Weddell Sea, where the thickest and most deformed sea ice is also present, consistent with *in situ* observations.

Differences in the various OIB-related snow-thickness products persist, especially given progressive improvements to the snow radar itself over the mission lifetime (Table 8). However, without these data our understanding of the regional and interannual variations of the snowpack on both Arctic and Antarctic sea ice would be substantially more limited.

6.2.3. Sea ice thickness

Arctic sea ice thickness was derived from OIB data by multiple studies (e.g., Farrell et al., 2012; Kurtz et al., 2013; Richter-Menge & Farrell, 2013). Although their results differ somewhat, their spatial patterns and interannual variability are both similar to and consistent with prior understanding of sea ice thickness distribution in the Arctic Ocean (e.g., Kwok & Rothrock, 2009). Specifically, the thickest sea ice is the multi-year ice north of Greenland, in the Lincoln Sea, and also just north of the Canadian Arctic Archipelago (e.g., Figure 17). Thinner, first-year ice is predominant in the Chukchi and Beaufort seas. OIB sea ice thickness timeseries have served as an important tool to assess those derived from satellites, including ICESat (Connor et al., 2013), CryoSat-2 (Laxon et al., 2013; Kurtz et al. 2014; Kwok & Cunningham, 2015; Tilling et al., 2018; Sallila et al., 2019), ICESat-2 (Kwok et al., 2019) and multi-sensor thickness assessments (e.g., Lindsay and Schweiger, 2015; Stroeve et al., 2014; Chen et al., 2017). These studies typically found that uncertainty in snow thickness is likely the primary source of uncertainty in Arctic sea ice thickness (e.g., Kwok et al., 2017).

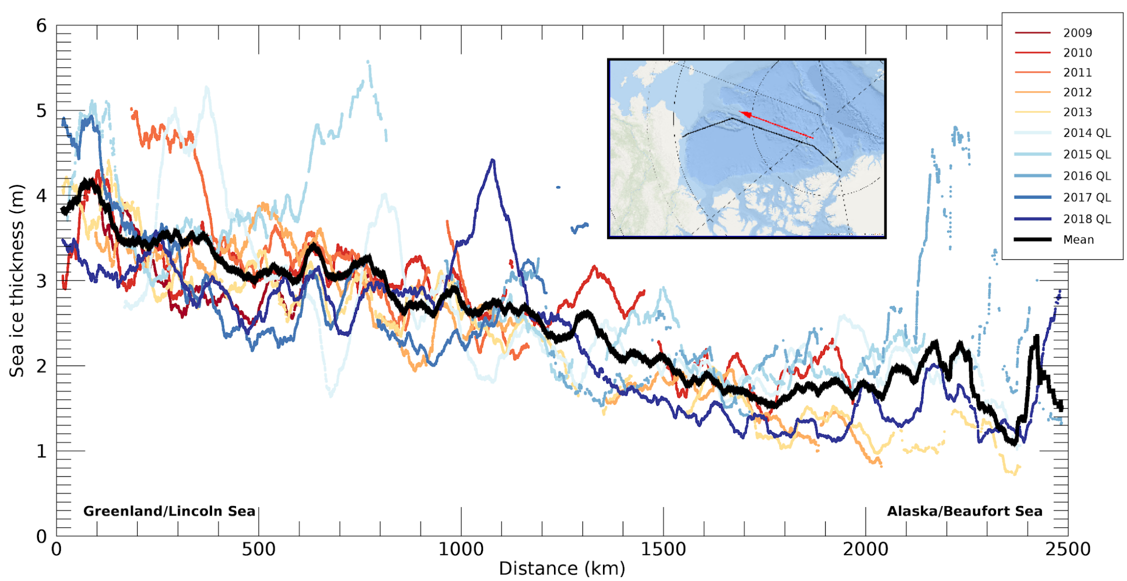

Figure 17. Laxon Line thickness

OIB PSO product sea ice thickness, smoothed with a 50 km boxcar average, for Laxon Line surveyed during 2009–2018 Arctic Spring campaigns. QL: Quicklook product.

The OIB quicklook sea ice thickness product was used alongside near-real-time observations from CryoSat-2 to assess Arctic sea ice thickness at the end of the 2015 winter season and was included in the 2015 Arctic Report Card (Perovich et al., 2015). At that time, the oldest sea ice north of Greenland and the Canadian Arctic Archipelago had a mean thickness of 3.5 m, with a strong zonal gradient toward thinner, seasonal ice in the Canada Basin and the eastern Arctic Ocean, where mean ice thickness was 2.4 m. A seven-year time series of OIB observations, spanning April 2009–2015, revealed that sea ice in the central

Arctic Ocean was predominantly multi-year, where mean and modal ice thickness were stable at ~3.2 m and 2.5 m, respectively. During that same period, sea ice in the Beaufort and Chukchi Seas was generally thinner, with mean and modal ice thickness of ~2.1 m and 1.8 m, respectively, with higher interannual variability. These results were consistent with an earlier study that used a five-year time series of OIB observations between 2009–2013 (Richter-Menge and Farrell, 2013).

Antarctic sea ice thickness has also been estimated from OIB campaigns. Considering the lack of basin-scale Antarctic snow thickness, previous studies using ICESat data assumed Antarctic freeboards are entirely snow, because Antarctic sea ice is generally thought to be thinner but overlain by thicker snow than in the Arctic, which can depress the snow–ice interface towards sea level (Kurtz and Markus, 2012). However, Kwok and Kacimi (2018) challenged this assumption using OIB data, finding that the snow thickness was often less than the snow freeboard. Deriving Antarctic snow thickness from OIB data and other remote-sensing methods is still an active area of research (§6.2.2), but Antarctic OIB data have provided crucial information to help develop and test new algorithms for satellite retrievals of freeboard and thickness of Antarctic sea ice (e.g., Fons and Kurtz, 2019; Kwok and Kacimi, 2018), along with iceberg topography and volume (e.g., Dammann et al., 2019).

6.2.4. Surface roughness

Sea ice is a heterogeneous medium, composed of sea ice floes of varying thickness and size, rubble fields, pressure ridges and eolian snow features (e.g., sastrugi and dunes). Studies of sea ice surface roughness consider the height variability introduced by the type and density of these morphological features. The presence and variability of snow grains or frost flowers also contributes to smaller-scale roughness at the micrometer to centimeter scale. A rougher ice pack increases the turbulent fluxes of momentum (e.g., form drag) and heat at the subaerial ice surface (Arya et al., 1973; Tsamados et al., 2014; Cole et al., 2017; Petty et al., 2017). Sea ice roughness is also thought to strongly influence both the formation and evolution of melt ponds (Polashenski et al., 2012; Webster et al., 2015; Landy et al., 2015).

ATM elevation data were used to produce roughness estimates over both Arctic and Antarctic sea ice (Kurtz et al., 2015; Kwok, 2015), and to calibrate roughness estimates from the Multi-angle Imaging SpectroRadiometer satellite (Nolin and Mar, 2019). The fine-resolution footprint and vertical accuracy of ATM data (§3.1.1) enabled detection of discrete surface features in the ice cover, e.g., the sails of pressure ridges, that are typically decimeters to meters tall and meters to kilometers wide. Sea ice pressure ridges are difficult to observe with satellite radar altimeters and likely pose a potential measurement bias in historical radar-altimeter ice-thickness data. Petty et al. (2016, 2017) used ATM data to produce feature-height estimates across the western Arctic Ocean and showed that these surface features are generally higher (>1 m) and more closely spaced in the multi-year ice pack ice of the Central Arctic Ocean, as compared to the first-year ice that dominates the Beaufort/Chukchi seas farther west. These feature heights generally follow a negative exponential distribution, confirming previous studies based on more limited data (e.g., Wadhams and Horne, 1980). Surface feature heights have also been estimated by measuring the lengths of shadows in visible imagery (e.g., DMS) and combining this with information regarding solar zenith angle (Kwok, 2014; Duncan et al., 2018). Fine-resolution DMS imagery were analyzed to derive the full sail-height distribution of sea ice pressure ridges in the Arctic (Duncan et al., 2018). OIB springtime surveys between 2010 and 2018 revealed that pressure-ridge sail heights both varied interannually and differed between the central Arctic and the Beaufort/Chukchi Seas regions (Duncan et al., 2020). These analyses will ultimately help improve the parameterization of surface roughness in sea ice models.

Analysis of the entire Arctic sea ice height record from OIB ATM data – within sections of hundreds of meters to kilometers long and including both flat and deformed ice – has demonstrated that sea ice heights exhibit more lognormal, as opposed to Gaussian, height distributions (Landy et al., 2020; Figure 18). This result directly informed the development of an improved re-tracking algorithm for ESA's CryoSat-2 radar altimeter (Landy et al., 2020). OIB Ku-band radar data was also used to profile the snow–ice interface height distribution and confirm that they were better represented by a lognormal distribution, suggesting that snow redistribution is only a second-order control on sea ice surface roughness.

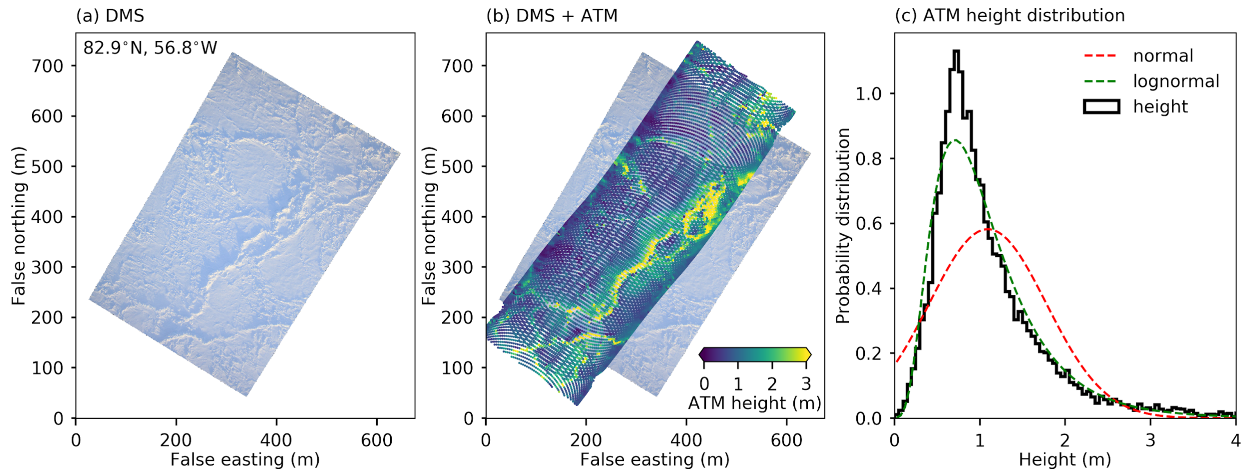

Figure 18: Sea ice roughness
Arctic sea ice topography observed by OIB on 21 March 2013. (a) DMS image. (b) DMS image overlaid with a ~700 × 250 m section of sea ice surface heights obtained from the ATM T4 wide scanner (c) Probability distribution of ATM surface heights, and normal/lognormal fits to that distribution.

6.2.5. Unanticipated discoveries

Analysis of OIB data further clarified the value of coincident laser and radar altimetry for deriving snow thickness from snow and ice freeboard differencing (e.g., Giles et al., 2007). Flying the snow radar along coincident CryoSat-2 tracks proved essential to assessing the accuracy of the snow thicknesses inferred by differencing ATM freeboards from CryoSat-2-derived ice freeboards (Kwok and Markus, 2018). These differenced thicknesses were comparable to the derived snow thickness, providing a framework for more recent ICESat-2-/CryoSat-2-derived snow and ice thicknesses (Kwok et al., 2020). These results highlighted the benefits of increased coincidence between ICESat-2 and CryoSat-2 orbits and supported ESA's decision to modify the CryoSat-2 orbit in the summer of 2020 (Kwok et al., 2020).

OIB quicklook sea ice data helped to improve sea ice forecasts. In 2012, OIB began producing a new quicklook sea ice product using field-processed ATM, DMS, CAMBOT and snow radar data (Kurtz et al., 2013). Rapid processing inevitably led to a lower quality dataset, but it was nonetheless found to be useful for sea ice forecasting and other comparison studies. For example, results from the first quicklook dataset were assimilated into a sea ice model and shown to improve the forecast of the September 2012 sea ice minimum (Lindsay et al., 2012). The quicklook data were also used for comparison studies of the thickness of sea ice and overlying snow with satellite and *in situ* data, and as a comparison dataset (rather than assimilated) for studies of seasonal sea ice forecasting (e.g., Allard et al., 2018).

OIB spring campaigns were sufficiently predictable in their cadence and instrument suite to produce both fundamental new knowledge about the state of Earth's sea ice cover and – for the Arctic surveys – quick-look data that were operationally valuable to other institutions monitoring that component of the cryosphere. The genesis and nature of the semi-regular OIB Arctic summer/fall campaigns was more varied, because of their shorter durations (typically less than a month) and the greater challenge in surveying the Arctic Ocean in the summer due to persistent cloud cover. Despite these challenges, both laser altimetry and visible imagery were acquired to improve our understanding of summer sea ice conditions and overlying melt ponds. Understanding the statistical distribution of melt-pond properties is valuable, because they have a lower albedo than snow or bare sea ice, absorbing more incoming solar radiation and altering the surface energy balance. Wright and Polashenski (2018) developed the Open Source Sea-ice Processing machine-learning toolkit to classify DMS imagery collected during the 2016 Arctic summer campaign and discriminated imaged surfaces between sea ice, open water and melt ponds. More recently, Buckley et al. (2020) developed a new algorithm to identify melt ponds using DMS visible imagery for the 2016 and 2017 Arctic summer campaigns and extended the classification to dark and light melt ponds (Figure 19). They determined that there was a higher mean melt-pond fraction (MPF) and darker melt ponds on thinner, first-year sea ice located in the Chukchi and Beaufort seas, whereas lower mean MPF and lighter melt ponds were present over thicker, multi-year ice located north of Greenland. Summer freeboards, snow and ice thickness have yet to be estimated from these data.

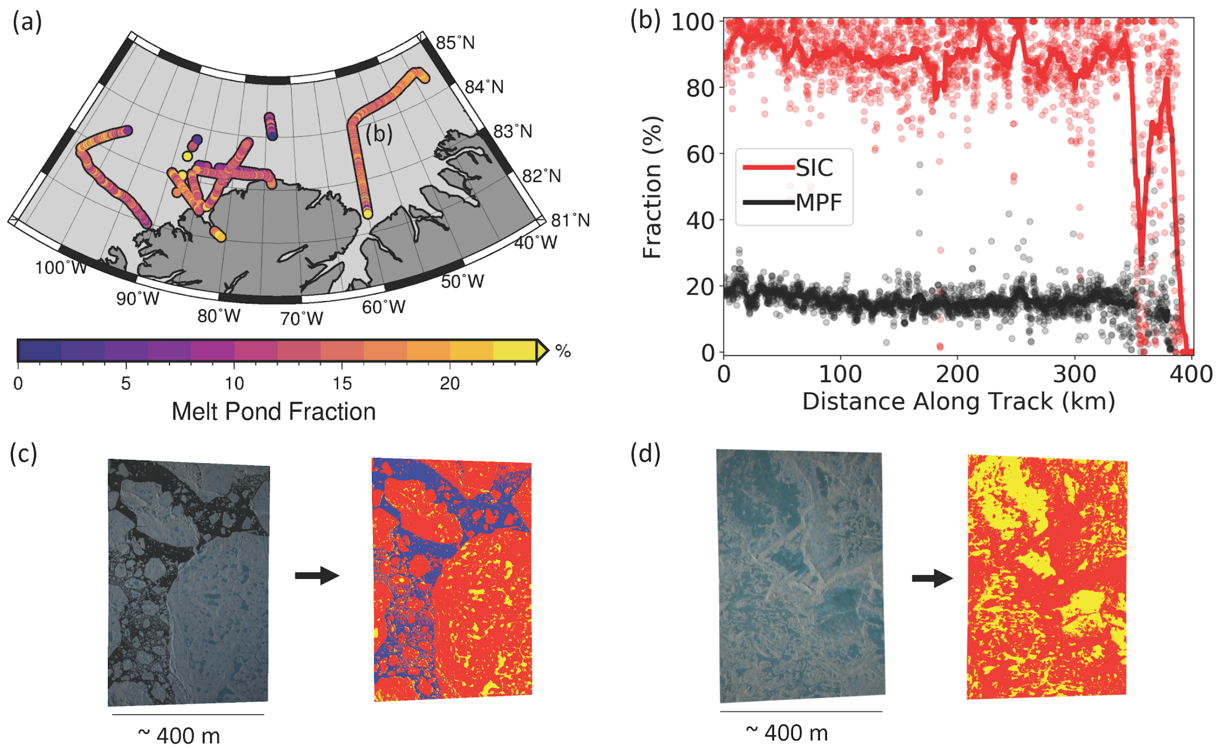

Figure 19. Melt ponds

(a) MPF calculated from DMS images collected over the Lincoln Sea during 2017 Arctic summer flights, where (b) marks the flight on 24 July 2017. (b) MPF and sea ice concentration (SIC) for each image (circles), overlain by 50-image running means (solid lines) for the flight on 24 July 2017. (c,d) Example DMS images from the same flight and classification results with sea ice (red), melt pond (yellow), and open water (blue) classified at (c) 83.3ºN 59.6ºW with low MPF (17%) and (d) 82.6ºN 59.9ºW, with high MPF (50%). Adapted from Buckley et al. (2020).

While anticipated (Table 3), OIB gravity data (§3.3) also helped to validate the ARCtic Satellite-only altimetric marine gravity field (McAdoo et al., 2013). This comparison highlighted the observation that short-wavelength errors in Arctic geoid/gravity models are widespread in areas lacking accurate surface gravity data.

7. Conclusions

7.1. Key contributions to advancing the state of knowledge in cryospheric science

Table 16. Key contributions

Before-and-after assessment of OIB's key contributions to advancing the state of knowledge in cryospheric science, and their implications for our understanding of the Earth system.

Topic	**Before OIB (2009)**	**After OIB (2020)**	
	State of knowledge	**State of knowledge**	**Implications for the Earth system**
Land ice			
Greenland Ice Sheet mass balance	Portions of the periphery of Greenland Ice Sheet were thinning, including some of its largest outlet glaciers (e.g., Jakobshavn Isbræ). While the ice sheet's overall mass balance was clearly negative, the interior appeared to be in balance and it was unclear how quickly losses at the periphery would advance upstream.	Regional increases in thinning could be observed and documented over time for nearly all large outlet glaciers. A few glaciers re-advanced, thickened, then retreated and thinned again in multi-annual cycles. Contiguous thinning has spread deeper into the interior.	The behavior and variability of Greenland's outlet glaciers can now be better modeled, connected to the interior, and included in sea-level rise projections and freshwater contributions to adjacent seas. Oceanic forcing can now be better distinguished from other forcings and its impacts better assessed.
Greenland subglacial topography	The large-scale setting was approximately known primarily from earlier surveys, but many large gaps existed. Many outlet glaciers flowed through channels that were essentially unrepresented in compilations of subglacial topography, and those compilations were not compatible with limited or entirely lacking knowledge of fjord or sub-ice-shelf bathymetry. These factors substantially limited interpretation of observed changes.	Mass conservation is now widely applied to reconcile sparse radar measurements with satellite-measured surface velocity and shipborne sonar measurements. All major gaps in our knowledge were filled in, especially along the periphery and within deeply incised fjords that drain most of Greenland's ice. Some channels have not yet been successfully sounded, and several interior gaps remain. Previously unimagined major subglacial geologic structures were found.	The cause of existing fundamental inconsistencies in ice-sheet models are now mostly corrected for the Greenland Ice Sheet. These corrections directly enable better representation of ice flow and projections of future mass loss. The need for extensive mapping of bed topography near ice fronts was clearly demonstrated, so that interannual glacier retreats and readvances can be reliably reproduced and interpreted.
Greenland Ice Sheet near-	Surface-to-bed connections lead to summertime acceleration of marginal, land-terminating ice.	A firn aquifer of variable depth and thickness is widespread beneath the periphery of the	A wide variety of forms and fates for meltwater generated at the surface of the Greenland Ice Sheet have been identified. Several are dynamically

surface hydrology	Seasonal supraglacial lakes could drain rapidly and lead to similar, temporary accelerations.	southern Greenland Ice Sheet, supraglacial lakes can be buried by snow but remain thawed through the wintertime, and near-continuous ice slabs can form within the percolation zone and limit runoff infiltration. The total melt estimated by regional climate models is compatible with that measured by repeat intra-annual surveys of elevation differences.	significant, and all are coupled with the atmosphere, so coupled models are essential to represent these processes accurately. However, their representation in ice-sheet models remains limited.
Greenland Ice Sheet internal structure	Internal radiostratigraphy was regularly observed, but how well ice age information could be extended beyond and between ice cores was unclear. The basic age structure of the Greenland Ice Sheet was poorly constrained and whether it was compatible with modern boundary conditions was unknown.	The gross age structure of the ice sheet is now known, and a variety of disturbed basal layers have now been identified, which can induce large folds in the stratigraphy that occupy up to half the ice column. Multi-millennial averages of key boundary conditions (basal melt, surface accumulation and velocity) have been generated from this age structure.	We can now connect multi-millennial changes within and across the Greenland Ice Sheet itself to related records of climate and sea-level change. These records help us understand the potential long-term magnitude of ice-sheet change in response to climate change and its coupling to the ocean and atmosphere.
Antarctic outlet-glacier behavior	Peripheral thinning was significant within the Amundsen Sea Embayment, but other areas of Antarctica were either stable or too steep to be resolved by satellite altimetry. Most outlet glaciers had either not yet surveyed by aircraft or had not been surveyed in several decades.	Most of the periphery of the West Antarctic Ice Sheet is thinning, and dramatic thinning of some ice shelves in the Amundsen Sea Embayment has occurred. In several locations, variability in interannual elevation change has been attributed to changes in ocean heat delivery.	Airborne data directly inform assessments of mass balance by mapping the pattern of surface-elevation change, particularly across major Antarctic outlet glaciers. These data constrain projections of sea-level rise and improve models of ice–ocean–atmosphere coupling.

Antarctic subglacial topography	The West Antarctic Ice Sheet was known to be grounded mostly below sea level, but only a few airborne radar-sounding surveys existed and many of those were focused on ice-core site selection rather than their potential vulnerability to ongoing climate forcing.	All of West Antarctica's major outlet-glacier systems have been surveyed more extensively, particularly those that are thinning rapidly in the Amundsen Sea Embayment. Most fast flow is concentrated in deep submarine troughs. Most remaining gaps in coverage are in areas out of reach by aircraft based off-continent.	Portions of the Antarctic ice sheet large enough to raise sea level by several meters have now been definitively shown to be vulnerable to ocean warming, a fundamental realization for projections of future sea-level change. Future investigations of small-scale basal roughness will help constrain retreat timescales.
Antarctic sub-ice-shelf bathymetry	Other than shipborne measurements of open-water bathymetry and on-ice seismic measurements, no large-scale method for constraining sub-ice-shelf bathymetry existed and our knowledge thereof was very limited.	The bathymetry of most of the ice shelves in West Antarctica and the Antarctic Peninsula has been constrained by multi-kilometer grids of fine-precision aerogravity close to the grounding zone, typically where fast-flowing outlet glaciers discharge. Constraining airborne gravity data with shipborne multibeam data offshore and radar data onshore was essential to constrain cavity thickness from gravity.	These difficult-to-reach cavities are among the most critical areas for understanding the potential for rapid sea-level rise. Our ability to assess their vulnerability is now greatly improved, but the fine-resolution bathymetry beneath many Antarctic ice shelves remains underexplored, especially in East Antarctica.
Snowfall on ice sheets	Knowledge of snow accumulation over ice sheets was from either *in situ* point measurements, with limited spatiotemporal coverage, or a handful of ground-based traverses. There was little consensus on the interannual variability of satellite-era accumulation rates at large scales.	Regional-to-local-scale accumulation rates up to the past several decades can now be mapped efficiently across both ice-sheet and glacier accumulation zones using airborne snow radar, although most regions remain undersampled, especially interior East Antarctica. These	Knowledge of snow accumulation is essential to assess mass change across the vast interiors of the Antarctic and Greenland ice sheets. Better ways of measuring snowfall narrow mass-balance estimates and sea-level contributions, improve our knowledge of ice–atmosphere coupling, and directly improve our interpretation of satellite altimetry records and their integration with other long records of change, such as ice cores.

		measurements often agree well with ground-based measurements and regional climate models, and they indicate the breadth of interannual variability in snow accumulation and its dependence on surface slope.	
Alaskan glacier mass balance	Most Alaskan glaciers were thinning, and the rate of mass loss in the early 2000s was greater than that of the Greenland Ice Sheet at the time.	Decreasing surface mass balance is the primary cause of Alaskan glacier mass loss. Fewer than a dozen major tidewater glaciers still terminate into the ocean and their dynamics are decreasing in significance to total mass loss as warming persists.	Mountain glaciers are critical water reserves worldwide and contribute about one third of current sea level rise; Alaskan glaciers are a major portion of that loss. In Alaska, glacier mass loss is primarily driven by surface melting, which guides future observation and modeling efforts.
Alaskan glacier thickness	Few Alaskan glaciers had been sounded, and most of those surveys were relatively small and ground-based.	The central flowlines of many large Alaskan glaciers have been sounded by low-frequency airborne radar, and several cross-flow profiles have also been collected.	Improved knowledge of Alaskan glacier thickness advances understanding glacier dynamics both there and elsewhere, including the coastal outlet glaciers of Greenland and Antarctica. The poorly known ice volume of most Alaskan glaciers is now better constrained.
Sea ice			
Arctic snow thickness on sea ice	Knowledge of snow thickness on Arctic sea ice was based mainly on a synthesis of in-situ measurements taken on drifting ice camps collected prior to the 1980s.	New fine-resolution, estimates of snow thickness on sea ice across hundreds of kilometers in the western Arctic Ocean. Confirmed thinner snow on first-year sea ice compared to multi-year ice. Snow thickness on western Arctic sea ice has thinned since the 1980s, commensurate with delayed sea ice freeze-up and an overall	Snow on sea ice insulates sea ice and modulates sea ice growth and melt. The impact of snow on sea ice formation and evolution can now be assessed quantitatively and sea ice thickness can be derived more accurately from satellite observations. A fundamental snow-thickness dataset to assess and improve precipitation outputs from satellite reanalyses of the Arctic Ocean now exists.

		younger ice pack.	
Arctic sea ice thickness	Though previous satellite-altimetry missions (ERS-1/2, Envisat, ICESat) provided information on the distribution of sea ice freeboard and thickness across the Arctic Ocean, knowledge of this variability at a regional scale was limited.	Detailed understanding of springtime western Arctic sea ice thickness distribution and its interannual variability, including thinner new ice and thicker ridged ice. Validation of springtime sea ice thickness retrievals from satellite altimeters (CryoSat-2, Sentinel-1, AltiKa and ICESat-2).	Knowledge of sea ice thickness is critical for better understanding the changing state of sea ice and its tight coupling between the ocean and atmosphere in the polar regions. Seasonal and multi-year records of sea ice thickness from OIB continue to be used for validation of satellite-based retrievals and to directly assess sea ice variability in the Arctic.
Arctic sea ice topography	Sparse on-ice and airborne measurements of the height distribution, roughness and pressure-ridge height and spacing distributions.	New fine-resolution estimates of sea ice topography and roughness at ridge-resolving (meter) scales for the western Arctic Ocean in springtime. Sail height distributions exhibit a negative exponential distribution. Both the snow and ice height distributions exhibit a lognormal distribution at the kilometer scales sampled by satellite radar altimeters.	Sea ice topography controls the strength of wind and ocean drag on the ice cover and the distribution of melt ponds. The detailed measurements now available provide a potential pathway for improving the representation of sea ice in Earth system models and refining satellite-based sea ice retrievals.
Arctic sea ice forecasting	Near-real-time sea ice thicknesses at basin scales were not available.	Quicklook products from springtime airborne campaigns were shown to improve summer sea ice forecasts significantly.	Seasonal forecasts of summer sea ice and long-term projections of sea ice can be improved with more accurate estimates of current sea ice thickness. Improved forecasts and long-term projections will help improve our understanding of the climate drivers of ongoing sea ice retreat, which are poorly constrained.
Antarctic sea ice properties	ICESat and ship-based climatology provided regional sea ice thickness estimates. ICESat assumed that the snow–ice interface was at sea level. Passive microwave snow-	New springtime estimates of Antarctic sea ice freeboard, thickness and snow thickness challenge previous assumptions and suggest thicker ice	Antarctic sea ice growth and melt has a significant influence on the properties and circulation of the Southern Ocean. Sea ice thickness can now be better estimated from satellite altimetry, which will help address outstanding questions

	thickness estimates provided data over first-year ice only.	closer to the Antarctic coastline, especially in the western Weddell Sea. Multiple Antarctic-specific behaviors (e.g., flooding), undersampling and fundamental measurement challenges leave many questions unanswered, in particular the key processes that control Antarctic sea ice thickness.	regarding the controls on sea ice in the Southern Ocean and the lack of decline in its extent as compared to sea ice in the Arctic.

Although much was learned from OIB datasets, many remain ripe for reprocessing and further investigation. For example, these possibilities include additional synthesis of ice-thickness and sub-ice-shelf cavity thickness measurements into existing compilations, tomographic mapping of subglacial topography from radar sounding, inference of density from the shallow radar sounding, geology-aware inferences of sub-ice-shelf bathymetry from gravimetry, and unified analyses of sea ice properties using laser altimetry and multiple imagers to better understand floe-size distributions and Antarctic sea ice characteristics. The combination of multiple types of observations collected concurrently on a single airborne platform enabled several OIB-related discoveries (e.g., the firn aquifer), and as scientists continue to explore multiple combinations of these unique datasets, new discoveries and understanding of polar processes are likely.

OIB's success relied partly on the unique attributes of airborne platforms that complement larger scale spaceborne observations. By including multiple instruments on a single platform and possessing the flexibility to upgrade instruments between campaigns, OIB could more rapidly integrate maturing remote-sensing technologies, e.g., the ATM T-7 dual-color laser altimeter, the 2–18 GHz Snow/Ku Radar and the iMAR/DgS hybrid gravimeter. Further, airborne mission design is more adaptable to evolving science requirements, targets of opportunity and logistical constraints, e.g., the evolution of OIB's scientific priorities for Antarctic land ice missions necessitated multiple basing changes, and the 2011 observation of a new rift on Pine Island Glacier's ice shelf (Howat et al., 2012). The broader scientific imperative to map surface-elevation change of polar land and sea ice can now be well met with satellites such as ICESat-2, but while fine-resolution spaceborne observations can now resolve elevation change within ever-narrower cryospheric targets, airborne surveys remain best suited to measure changes in the reference frame most relevant to process-based studies (e.g., along the flowlines of sinuous outlet glaciers).

OIB's data management plan, which aimed to release data quickly without restrictions, was certainly a major contributor to the scientific impact and success of OIB. This policy ensured that the data were made quickly available to interested scientists who otherwise had no direct association with OIB campaigns, putting OIB-unassociated early career scientists and established ST members on a level playing field. As the mission progressed, the latency in informing both the broader scientific community and the public of ongoing changes in the cryosphere decreased, and the fraction of publications using OIB data by scientists who were not formally associated with the mission increased. Relatively rapid data release also enabled efficient and timely feedback following regular campaigns for the PSO and ST to adjust survey and measurement priorities. A drawback was that this process made data assessment more challenging for ST members, because they were no longer as tightly integrated with instrument teams, but by design most OIB instruments were already fairly mature. OIB's data archive at the NSIDC set a new standard for polar airborne missions to ensure that these hard-earned datasets are both well preserved and well documented.

OIB also endeavored to share its flight operations, scientific discoveries and the natural majesty of the polar cryosphere with a broad public audience. It did so through numerous outreach activities both during and surrounding its campaigns, including dozens of short- and long-format videos and social media features developed internally by NASA, daily distribution of photography, and conversations with >10,000 primary and secondary school students from around the globe using an in-flight text chat system. Local, national, international and independent media directly interacted with OIB as guest fliers onboard larger aircraft that could accommodate them (e.g., P-3, DC-8). Particularly during the campaigns themselves, this outreach was aided by increasing availability of fast and reliable internet access at remote bases.

7.2. Outstanding challenges for future airborne investigations of the polar cryosphere

In conclusion, based on our cumulative OIB experience, we identify below outstanding challenges for future airborne investigations of the cryosphere. Our goal is not to prescribe specific mission concepts, but rather to highlight the breadth of remaining scientific questions regarding the polar cryosphere that could be addressed from aircraft and have not yet been met – even by a 12-year mission as robustly supported as OIB.

7.2.1. Land ice

With both the successful launch of ICESat-2 and OIB's measurement overlap with it, OIB achieved its primary scientific objective of continuing measurements of elevation change in the most at-risk and fastest-changing regions of the Greenland and Antarctic ice sheets and Alaskan glaciers (Tables 1–3). From initial analyses of ICESat-2 data, we can now further pinpoint regions of ongoing concern (Smith et al., 2020). From its combination with earlier airborne campaigns, OIB directly helped build a long record of altimetric change that extends back to 1993 in Greenland and 2002 in West Antarctica and the Antarctic Peninsula. This consolidated knowledge can be used to target finer-resolution airborne surveys to study the origin of the observed elevation change, which inevitably requires other instruments in addition to altimeters, as OIB demonstrated consistently.

With progressive improvements in satellite altimetry over recent decades, the largest remaining uncertainty in the total ice-sheet mass balance arises from uncertainty in surface mass balance and firn densification rates (Smith et al., 2020). Additional investigation of OIB snow radar data could drive improvements to global and regional climate models and further constrain estimates of ice-sheet contribution to sea-level rise from altimetry. Snow accumulation is the dominant source of mass gain for both ice sheets, yet this key boundary condition remains under-constrained, especially across vast swaths of East Antarctica (Lenaerts et al., 2019). Because of its large area, small relative changes in modeled snowfall there can lead to large absolute changes in total mass balance (Rignot et al., 2019). Snow radar data collected during the final OIB Antarctic campaign could help constrain both global and regional climate model performance there, following methods demonstrated elsewhere (e.g., Medley et al., 2013). Besides validating modeled multi-annual mean snow-accumulation rates, the OIB snow radar dataset over Antarctica contains substantial information regarding the temporal variability in snow accumulation and rate of firn compaction, yet this information remains largely unexplored.

OIB's reach was extensive in the polar regions, particularly in Greenland and parts of West Antarctica, but major gaps remain within OIB's survey regions, particularly in measuring the boundary condition that often controls ongoing changes: bed topography. Thousands of kilometers of difficult-to-reach portions of the East Antarctic coastline – as well as the deep interior of both East and West Antarctica – remain under- or unexplored, most Canadian ice caps and outlet glaciers are only sparsely surveyed, and the overwhelming majority of Alaskan glaciers have never been surveyed. A major outcome from OIB and related efforts (e.g., OMG) is that future airborne campaigns aiming to map subglacial topography at finer resolution can be more efficient, given a clearer path toward selecting the best radar sounder for the target environment. With ever-improving satellite measurements of surface velocity, identification of poorly constrained regions using mass conservation can guide future surveys to areas where finer resolution is required to constrain local mass flux. We note the success of across-flow surveys in constraining the mass flux within deeply incised subglacial troughs. Through OIB, it was better recognized that successful radar sounding of an outlet glacier sometimes requires dense, regular survey grids, because a single survey line subject to substantial off-nadir clutter can lead to incorrect identification of the ice–bed reflection. Further, to understand or project glacier retreat/advance, it is essential to characterize bed topography over broad regions surrounding ice fronts and grounding zones.

Ice–ocean interactions play a major role in the evolution of both the Greenland and Antarctic ice sheets, but progress in understanding and modeling thereof remains limited by a lack of detailed knowledge of bathymetry at grounding zones and beneath ice shelves, along with sub-ice-shelf ocean properties (e.g., temperature, salinity). Whereas much progress has been made in Greenland and parts of West Antarctica, vast sectors of the East Antarctic continental shelf are either unsurveyed or under-surveyed. Few have been studied intensively with an instrument suite of the scope that OIB typically brought to bear. Further effort to document physical conditions along the periphery of Antarctica is needed, and achieving this goal will require airborne campaigns and instrument suites informed by OIB's legacy. In that context, it will become increasingly important to match large-scale airborne campaigns to the needs of an even broader community of scientists than those needs met through OIB, a community that includes glaciologists, climatologists, oceanographers and Earth system modelers.

The quality and breadth of the radiostratigraphy detected by OIB radar sounders provided new opportunities to map and interpret the spatial variation in the dynamics of the Greenland Ice Sheet, as recorded by the ice sheet itself. While the reach of the mission was less extensive in Antarctica, similar opportunities exist there, particularly by combining OIB radar data with that from other international campaigns (e.g., the AntArchitecture effort; Cavitte et al., 2016; Winter et al., 2017). Along with geometry, these data were further leveraged to resolve other englacial properties of fundamental glaciological interest (e.g., physical temperature, firn-aquifer extent and thickness). Newer instruments not deployed by OIB, such as a wideband radiometer (Yardim et al, 2021) or a multi-polarization ultrawideband radar sounder (Yan et al., 2020), could help better resolve from airborne platforms some englacial properties that are otherwise sparsely sampled *in situ*.

7.2.2. Sea ice

Ongoing efforts to fully exploit existing OIB data should be an essential near-future objective of the sea ice research community. Beyond that, new survey strategies, including new bases or aircraft, could produce OIB-level detail on freeboard, snow and ice thickness, surface roughness and melt ponds – especially in the eastern sector of the Arctic Ocean that was not surveyed during OIB. The same is true for sea ice in the Southern Ocean generally, because OIB could only survey a small fraction of the sea ice in this increasingly variable region (Shepherd et al., 2018). OIB conducted regular spring campaigns and occasional summer/fall campaigns, but repeat measurements through the year with an OIB-caliber instrument suite could provide invaluable insight into the time evolution of sea ice properties, especially snow thickness and fine-resolution sea ice topography and the distribution and properties of melt ponds, further extending the utility of airborne remote sensing in the evaluation of satellite data products beyond the previous assessments made with the springtime OIB campaigns. Future airborne mission planning could benefit from Observing System Simulation Experiments to more efficiently optimize data collection strategies.

Future work could also be done to improve retrievals of sea ice properties from airborne datasets. In particular, unambiguous detection of the air–snow interface from snow radar remains challenging (Rösel et al., in press), and ever-evolving system parameters between each campaign hampered development of robust retrieval algorithms and made their validation against *in situ* measurements more difficult. A future snow radar system with a smaller footprint may be needed to address the challenge of the air–snow interface, and further maturation the development of stable, operational snow radar may be needed to rigorously monitor and quantify uncertainty in the future evolution of snow thickness on sea ice.

In situ measurements of snow and ice density and thickness on both Arctic and Antarctic sea ice remain essential for validation of both airborne and satellite remote sensing of sea ice properties (e.g., Kwok et al., 2017). Such measurements are also essential to interpreting ongoing changes in the sea ice system. For example, interpreting data from Antarctic sea ice campaigns remains especially challenging due to the more complex properties of the snow–ice interface. Future airborne campaigns will undoubtedly continue to benefit from coincident *in situ* measurements.

As of this writing, CryoSat-2's orbit has now maneuvered so that its ground tracks will be better aligned both spatially and temporally with ICESat-2 as part of a campaign called CRYO2ICE (https://earth.esa.int/eogateway/missions/cryosat/cryo2ice). Once these satellites' orbits have increased spatial and temporal coincidence, airborne and ground validation of both CryoSat-2 and ICESat-2, similar to the validation experiments conducted by OIB over sea ice, will be essential to further interpret these coincident datasets and produce concurrent snow and sea ice thickness estimates.

As the sea ice cover of the Arctic Ocean continues to decline, the length of the melt season increases, and the date of fall freeze-up shifts later (Stammerjohn et al., 2012), ocean temperature, salinity, wave activity and the biogeochemical balance of the ocean in both the marginal ice and coastal zones are changing rapidly. Extending the OIB-caliber instrument suite to include the next generation of ocean remote sensing technologies will be needed to fully capture and understand changing sea ice and ocean conditions in both the Arctic and Southern Oceans. As the climate system continues to change, future airborne missions would also benefit from coincident measurements of atmospheric (e.g. clouds, aerosols, radiation) and sea ice properties (e.g. albedo, snow thickness, melt pond depth) to improve our presently limited understanding of sea ice–atmosphere interactions and their ongoing evolution. Airborne remote sensing is uniquely suited for such tasks because they acquire high-resolution, multi-sensor observations targeted at areas where the most rapid changes are occurring. Airborne systems can also continue to provide more rapid deployment, testing and calibration of new remote sensing technologies, as compared to satellite missions, which could prove essential for rapidly evolving sea ice systems.

Acknowledgments

We thank the innumerable pilots, aircraft mechanics and safety officers, ground-support personnel, instrument designers and operators, logisticians, embassies, airports, hoteliers, visitors, teachers, writers, videographers and media without whom OIB would not have been possible nor have reached the scientific and public audience that it did. Inter-agency and international collaborations were also essential to OIB's success (inter-agency: Cold Regions Research and Engineering Laboratory, Department of State, National Geospatial Intelligence Agency, National Oceanic and Atmospheric Administration, National Science Foundation and its U.S. Antarctic Program, UNAVCO, and U.S. Naval Academy; international: Alfred Wegener Institute for Polar and Marine Research, Australian Antarctic Division, Australian Bureau of Meteorology, British Antarctic Survey, Danish Meteorological Institute, Environment and Climate Change Canada, European Space Agency, Institut polaire français Paul-Émile Victor (French Polar Institute), Norwegian Polar Institute, and Technical University of Denmark). We thank the leadership at NASA – in particular R.T. Albertson, C. Dobson, C.M. Haffke, M.H. Freilich, K. Harbeck, J.A. Kaye, T. Markus, B.A. Tagg and C.E. Webb – for their relentless support of OIB. We thank the National Snow and Ice Data Center for their careful archiving and distribution of OIB data, including the data shown in this review that are available at https://nsidc.org/data/icebridge/. We thank Associate Editor E. Rohling, reviewers R. Forsberg and C. Haas for constructive comments. Finally, we thank the innumerable scientists who studied OIB data and in doing so advanced scientific understanding of Earth's polar regions.

Author contributions

All authors provided substantive feedback to drafts of this manuscript, in most cases multiple sections based on their respective experiences as part of OIB, so we describe here only their primary contributions to this article. JAM, LNB and BM conceived and led the development of this review, with support from AAP, JPH, JGS, ELDM, CMH and JEW. MS, JGS, SM and JKY drafted the ATM instrument descriptions. MAH and JBB drafted the LVIS description. CFL drafted the UAF Riegl description. FRM, JDP, CJL and SPG drafted the CReSIS instrument descriptions. EJR drafted the WISE description. MT drafted the UAF HF radar sounder description. MSC and JWH drafted the ARES description. KJT and CDL drafted the AIRGrav, iMAR/DgS and Scintrex CS-3 instrument descriptions. DAY and JSG drafted the UTIG instrument descriptions. RTD drafted the DMS description. REB, JRC, BMC, MAF, JSG, JWH, KCJ, LSK, CFL, TAN, SMJN, EJR, MRS, BES, JGS, MS, DAY and TPW drafted and reviewed land-ice outcomes. AAP, NTK, EB-W, EMB, SLF, RK, SM, JAR-M, MS and JPH drafted and reviewed sea-ice outcomes.

Glossary

Acronym	Description
AGL	Above Ground Level
AIM	Arctic Ice Mapping
ALAMO	Airborne LiDAR with Mapping Optics
ARES	Arizona Radio Echo Sounder
ATM	Airborne Topographic Mapper
CAMBOT	Continuous Airborne Mapping by Optical Translator
CAS	Commercial Aircraft Services
CReSIS	Center for Remote Sensing of Ice Sheets
CryoVEx	CryoSat-2 Validation Experiment
DEM	Digital Elevation Model
DMS	Digital Mapping System
ESA	European Space Agency
FLIR	Forward Looking Infrared
FMCW	Frequency-Modulated Continuous Waveform
FOV	Field of View
GLAS	Geosciences Laser Altimeter System
GLONASS	Globalnaya Navigatsionnaya Sputnikovaya Sistema
GNSS	Global Navigation Satellite System
GPS	Global Positioning System
HF	High Frequency

HiCARS	High Capability Radar Sounder
ICECAP	Investigating the Cryospheric Evolution of the Central Antarctic Plate
ICESat	Ice, Cloud, and Land Elevation Satellite
ICESat-2	Ice, Cloud, and Land Elevation Satellite 2
INS	Inertial Navigation System
INTERMAGNET	International Real-time Magnetic Observatory Network
LVIS	Land, Vegetation and Ice Sensor
MCoRDS	Multi-channel Coherent Radar Depth Sounder
MPF	Melt Pond Fraction
NASA	National Aeronautics and Space Administration
NI	National Instruments
NOAA	National Oceanic and Atmospheric Administration
NSIDC	National Snow and Ice Data Center
OIB	Operation IceBridge
OMG	Oceans Melting Greenland
PARCA	Program for Arctic Regional Climate Assessment
PARIS	Pathfinder Advanced Radar Ice Sounder
PCL	Photon Counting LiDAR
PPP	Precise Point Positioning
PRF	Pulse Repetition Frequency
PSO	Project Science Office
RCM	Regional Climate Model
RF	Radio Frequency
Rx	Receiver
SILDAMS	Sea-Ice Lead Detection Algorithm using Minimal Signal
SNR	Signal-to-Noise Ratio
ST	Science Team
SWIR	Short-Wave Infrared
Tx	Transmitter
UAF	University of Alaska Fairbanks
USA	United States of America
UTIG	The University of Texas at Austin’s Institute for Geophysics
VNIR	Visible and Near-Infrared
WISE	Warm Ice Sounding Explorer

References

Abshire, J. B., Sun, X., Riris, H., Sirota, J. M., McGarry, J. F., Palm, S., et al. (2005). Geoscience laser altimeter system (GLAS) on the ICESat mission: on-orbit measurement performance, *Geophysical Research Letters*. *32*(21). https://doi.org/10.1029/2005GL024028

Arctic Climate Impact Assessment (2004). Impacts of a Warming Arctic: Arctic Climate Impact Assessment, Cambridge Univ. Press. https://acia.amap.no/

Adusumilli, S., Fricker, H. A., Siegfried, M. R., Padman, L., Paolo, F. S., & Ligtenberg, S. R. (2018), Variable basal melt rates of Antarctic Peninsula ice shelves, 1994–2016. *Geophysical Research Letters*, *45*(9), 4086–4095. https://doi.org/10.1002/2017GL076652

Agosta, C., Amory, C., Kittel, C., Orsi, A., Favier, V., Gallée, H., et al. (2019). Estimation of the Antarctic surface mass balance using the regional climate model MAR (1979–2015) and identification of dominant processes. *The Cryosphere*, *13*(1), 281–296. https://doi.org/10.5194/tc-13-281-2019

Aitken, A. R. A., Roberts, J. L., van Ommen, T. D., Young, D. A., Golledge, N. R., Greenbaum, J. S., et al. (2016a). Repeated large-scale retreat and advance of Totten Glacier indicated by inland bed erosion. *Nature*, *533*(7603), 385–389. https://doi.org/10.1038/nature17447

Aitken, A. R. A., Betts, P. G., Young, D. A., Blankenship, D. D., Roberts, J. L. & Siegert, M. J. (2016b). The Australo-Antarctic Columbia to Gondwana transition. *Gondwana Research*, *29*, 136–152. https://doi.org/10.1016/j.gr.2014.10.019

Allard, R. A., Farrell, S. L., Hebert, D. A., Johnston, W. F., Li, L., Kurtz, N. T., et al. (2018). Utilizing CryoSat-2 sea ice thickness to initialize a coupled ice-ocean modeling system. *Advances in Space Research*, *62*(6), 1265–1280. https://doi.org/10.1016/j.asr.2017.12.030

Alley, K. E., Scambos, T. A., Siegfried, M. R., & Fricker, H. A. (2016). Impacts of warm water on Antarctic ice shelf stability through basal channel formation. *Nature Geoscience*, *9*(4), 290–293. https://doi.org/10.1038/ngeo2675

An, L., E. J. Rignot, S. Elieff, M. Morlighem, R. Millan, J. Mouginot, et al. (2017). Bed elevation of Jakobshavn Isbrae, West Greenland, from high-resolution airborne gravity and other data. *Geophysical Research Letters*, *19*(141), 1134–9. https://doi.org/10.1002/2017GL073245

An, L., Rignot, E., Chauche, N., Holland, D. M., Holland, D., Jakobsson, et al. (2019). Bathymetry of Southeast Greenland From Oceans Melting Greenland (OMG) Data. *Geophysical Research Letters*, *46*(20), 11197–11205. https://doi.org/10.1029/2019GL083953

Andrews, L. C., Hoffman, M. J., Neumann, T. A., Catania, G. A., Lüthi, M. P., Hawley, R., et al. (2018). Seasonal Evolution of the Subglacial Hydrologic System Modified by Supraglacial Lake Drainage in Western Greenland. *Journal of Geophysical Research: Earth Surface*, *109*, F03005–18. https://doi.org/10.1029/2017JF004585

Arendt, A. A., Echelmeyer, K., Harrison, W. D., Lingle, C. S., & Valentine, V. B. (2002). Rapid wastage of Alaska glaciers and their contribution to rising sea level. *Science*, *297*(5580), 382–386. https://doi.org/10.1126/science.1072497

Argyle, M., Ferguson, S., Sander, L., & Sander, S. (2000). AIRGrav results: A comparison of airborne gravity data with GSC test site data. *The Leading Edge*, *19*, 1134–1138. https://doi.org/10.1190/1.1438494

Armitage, T. W., & Ridout, A. L. (2015). Arctic sea ice freeboard from AltiKa and comparison with CryoSat-2 and Operation IceBridge. *Geophysical Research Letters*, *42*(16), 6724–6731. https://doi.org/10.1002/2015GL064823

Arya, S. P. S. (1973). Contribution of form drag on pressure ridges to the air stress on Arctic ice. *Journal of Geophysical Research, 78*(30), 7092–7099. https://doi.org/10.1029/JC078i030p07092

Aschwanden, A., Fahnestock, M. A., & Truffer, M. (2016). Complex Greenland outlet glacier flow captured. *Nature Communications*, *7*. https://doi.org/10.1038/ncomms10524

Aschwanden, A., Fahnestock, M. A., Truffer, M., Brinkerhoff, D. J., Hock, R., Khroulev, C., et al. (2019). Contribution of the Greenland Ice Sheet to sea level over the next millennium, *Science Advances*, *5*(6), eaav9396. https://doi.org/10.1126/sciadv.aav9396

Baldwin, D. J., Bamber, J. L., & Payne, A. J. (2003), Using internal layers from the Greenland ice sheet, identified from radio-echo sounding data, with numerical models. *Annals of Glaciology*, *37*(1), 325–330. https://doi.org/10.3189/172756403781815438

Bamber, J. L., Griggs, J. A., Hurkmans, R. T. W. L., Dowdeswell, J. A., Gogineni, S. P., Howat, I., et al. (2013a) A new bed elevation dataset for Greenland *The Cryosphere*, *7*(2), 499–510. https://doi.org/10.5194/tc-7-499-2013

Bamber, J. L., Siegert, M. J., Griggs, J. A., & Marshall, S. J. (2013b). Paleofluvial mega-canyon beneath the central Greenland ice sheet. *Science*, *341*, 997–999. https://doi.org/10.1126/science.1238072

Barletta, V. R., Bevis, M., Smith, B.E., Wilson, T., Brown, A., Bordoni, A., et al. (2018). Observed rapid bedrock uplift in Amundsen Sea Embayment promotes ice-sheet stability. *Science*, *360*(6395), 1335–1339. https://doi.org/10.1126/science.aao1447

Bell, R. E. & Watts, A. B. (1986). Evaluation of the BGM-3 sea gravity meter system onboard R/V Conrad. *Geophysics*, *51*(7), 1480–1493. https://doi.org/10.1190/1.1442196

Bell, R. E., Tinto, K. J., Das, I., Wolovick, M. J., Chu, W., Creyts, T. T., et al. (2014). Deformation, warming and softening of Greenland's ice by refreezing meltwater. *Nature Geoscience*, *7*(7), 497–502. https://doi.org/10.1038/ngeo2179

Benson, C. S. (1996). Stratigraphic studies in the snow and firn of the Greenland ice sheet. *CRREL (SIPRE) Research Report*, *70*, US Army Cold Regions Research and Engineering Laboratory, Hanover, New Hampshire

Berthier, E., Larsen, C., Durkin, W. J., Willis, M. J., & Pritchard, M. E. (2018). Brief communication: Unabated wastage of the Juneau and Stikine icefields (southeast Alaska) in the early 21st century. *The Cryosphere*, *12(*4), 1523–1530. https://doi.org/10.5194/tc-12-1523-2018

Bertrand, K. J. (1967). A look at Operation Highjump twenty years later. *Antarctic Journal of the United States*, *2*(1), 5–12.

Blair, J., Rabine, D., & Hofton, M. (1999). The laser vegetation imaging sensor (LVIS): A medium-altitude, digitization-only, airborne laser altimeter for mapping vegetation and topography. *ISPRS Journal Photogrammetry and Remote Sensing*, *54*, 115–122. https://doi.org/10.1016/S0924-2716(99)00002-7

Blanchard-Wrigglesworth, E., Farrell, S. L., Newman, T. & Bitz, C. M. (2015). Snow cover on Arctic sea ice in observations and an Earth System Model. *Geophysical Research Letters*, *42*, 10,342–10,348. https://doi.org/10.1002/2015GL066049

Blanchard-Wrigglesworth, E., Webster, M. A., Farrell, S. L., & Bitz, C. M. (2018). Reconstruction of snow on Arctic sea ice. *Journal of Geophysical Research: Oceans, 123*, 3588–3602. https://doi.org/10.1002/2017JC012264

Bodart, J. A., Bingham, R. G., Ashmore, D. W., Karlsson, N. B., Hein, A. S., & Vaughan, D. G. (in press). Age-depth stratigraphy of Pine Island Glacier inferred from airborne radar and ice-core chronology. *Journal of Geophysical Research: Earth Surface*. https://doi.org/10.1029/2020JF005927

Boghosian, A., Tinto, K. J., Cochran, J. R., Porter, D., Elieff, S., Burton, B. L., & R. E. Bell (2015). Resolving bathymetry from airborne gravity along Greenland Fjords. *Journal of Geophysical Research: Solid Earth*, *120*. https://doi.org/10.1002/2015JB012129

Bons, P. D., Jansen, D., Mundel, F., Bauer, C. C., Binder, T., Eisen, O. et al. (2016). Converging flow and anisotropy cause large-scale folding in Greenland's ice sheet. *Nature Communications*, *7*. https://doi.org/10.1038/ncomms11427

Bowling, J. S., Livingstone, S. J., Sole, A. J., & Chu, W. (2019). Distribution and dynamics of Greenland subglacial lakes. *Nature Communications*, *10*(1). https://doi.org/10.1038/s41467-019-10821-w

Box, J. E. & Ski, K. (2007). Remote sounding of Greenland supraglacial melt lakes: implications for subglacial hydraulics. *Journal of Glaciology*, *53*, 257–265. https://doi.org/10.3189/172756507782202883

Brancato, V., Rignot, E., Milillo, P., Morglihem, M., Mouginot, J., An, L., et al. (2020). Grounding Line Retreat of Denman Glacier, East Antarctica, Measured With COSMO-SkyMed Radar Interferometry Data. *Geophysical Research Letters*, *47*(7). https://doi.org/10.1029/2019GL086291

Brucker, L., & Markus, T. (2013). Arctic-scale assessment of satellite passive microwave-derived snow depth on sea ice using Operation IceBridge airborne data. *Journal of Geophysical Research: Oceans*, *118*, 2892–2905. https://doi.org/10.1002/jgrc.20228

Brunt, K. M., Hawley, R., Lutz, E. R., Studinger, M., Sonntag, J. G., Hofton, M. A., et al. (2017), Assessment of NASA airborne laser altimetry data using ground-based GPS data near Summit Station, Greenland. *The Cryosphere*, *11*(2), 681–692. https://doi.org/10.5194/tc-11-681-2017

Brunt, K. M., Neumann, T. A., & Smith, B. E. (2019). Assessment of ICESat-2 Ice Sheet Surface Heights, Based on Comparisons Over the Interior of the Antarctic Ice Sheet. *Geophysical Research Letters*, *46*(22), 13072–13078. https://doi.org/10.1029/2019GL084886

Buckley, E. M., Farrell, S. L., Duncan, K., Connor, L. N., Kuhn, J. M., & Dominguez, R. T. (2020). Classification of Sea Ice Summer Melt Features in High-resolution IceBridge Imagery. *Journal of Geophysical Research: Oceans*, *125*, e2019JC015738. https://doi.org/10.1029/2019JC015738

Catania, G. A., Stearns, L. A., Sutherland, D. A., Fried, M. J., Bartholomaus, T. C., Morlighem, M., et al. (2018). Geometric Controls on Tidewater Glacier Retreat in Central Western Greenland. *Journal of Geophysical Research: Earth Surface*, *123*(8), 2024–2038. https://doi.org/10.1029/2017JF004499

Catania, G. A., Stearns, L. A., Moon, T. A., Enderlin, E. M., & Jackson, R. H. (2020). Future Evolution of Greenland's Marine-Terminating Outlet Glaciers. *Journal of Geophysical Research: Earth Surface*, *125*, e2018JF004873. https://doi.org/10.1029/2018JF004873

Cavitte, M. G. P., Blankenship, D. D., Young, D. A., Schroeder, D. M., Parrenin, F., LeMeur, E., et al. (2016). Deep radiostratigraphy of the East Antarctic plateau: connecting the Dome C and Vostok ice core sites. *Journal of Glaciology*, *62*(232), 323–334. https://doi.org/10.1017/jog.2016.11

Chen, Z., Liu, J., Song, M., Yang, Q., & Xu, S. (2017). Impacts of assimilating satellite sea ice concentration and thickness on Arctic sea ice prediction in the NCEP Climate Forecast System. *Journal of Climate*, *30*(21), 8429–8446. https://doi.org/10.1175/JCLI-D-17-0093.1

Chu, W., Schroeder, D. M., Seroussi, H., Creyts, T. T., Palmer, S. J., & Bell, R. E. (2016). Extensive winter subglacial water storage beneath the Greenland Ice Sheet. *Geophysical Research Letters*, *43*. https://doi.org/10.1002/2016GL071538

Chu, W., Schroeder, D. M., Seroussi, H., Creyts, T. T., & Bell, R. E. (2018). Complex Basal Thermal Transition Near the Onset of Petermann Glacier, Greenland. *Journal of Geophysical Research: Earth Surface*, *123*. https://doi.org/10.1029/2017JF004561

Chu, W., Schroeder, D. M., & Siegfried, M. R. (2018). Retrieval of Englacial Firn Aquifer Thickness From Ice-Penetrating Radar Sounding in Southeastern Greenland. *Geophysical Research Letters*, *45*, 11,770–11,778. https://doi.org/10.1029/2018GL079751

Ciracì, E., Velicogna, I., & Sutterley, T. (2018). Mass Balance of Novaya Zemlya Archipelago, Russian High Arctic, Using Time-Variable Gravity from GRACE and Altimetry Data from ICESat and CryoSat-2. *Remote Sensing*, *10*, 1817. https://doi.org/10.3390/rs10111817

Cochran, J. R., & Bell, R. E. (2012). Inversion of IceBridge gravity data for continental shelf bathymetry beneath the Larsen Ice Shelf, Antarctica. *Journal of Glaciology*, *58*(209), 540–552. https://doi.org/10.3189/2012JoG11J033

Cochran, J. R., Tinto, K. J., & Bell, R. E. (2015). Abbot Ice Shelf, structure of the Amundsen Sea continental margin and the southern boundary of the Bellingshausen Plate seaward of West Antarctica. *Geochemistry, Geophysics, Geosystems*, *16*(5), 1421–1438. https://doi.org/10.1002/2014GC005570

Cochran, J. R., Tinto, K. J., & Bell, R. E. (2020). Detailed Bathymetry of the Continental Shelf Beneath the Getz Ice Shelf, West Antarctica. *Journal of Geophysical Research: Earth Surface*, *125*, e2019JF005493. https://doi.org/10.1029/2019JF005493

Cole, S. T., Toole, J. M., Lele, R., Timmermans, M.-L., Gallaher, S. G., Stanton, T. P., et al. (2017). Ice and ocean velocity in the Arctic marginal ice zone: Ice roughness and momentum transfer. *Elementa Science of the Anthropocene*, *5*. https://doi.org/10.1525/elementa.241

Colgan, W. T., Abdalati, W., Citterio, M., Csatho, B., Fettweis, X., Luthcke, S. B., et al. (2015). Hybrid glacier Inventory, Gravimetry and Altimetry (HIGA) mass balance product for Greenland and the Canadian Arctic. *Remote Sensing of the Environment*, *168*(C), 24–39. https://doi.org/10.1016/j.rse.2015.06.016

Colgan, W. T., Machguth, H., MacFerrin, M., Colgan, J. D., van As, D., & MacGregor, J. A. (2016). The abandoned ice sheet base at Camp Century, Greenland, in a warming climate. *Geophysical Research Letters*, *43*. https://doi.org/10.1002/2016GL069688

Comiso, J. C., Parkinson, C. L., Gersten, R., & Stock, L. (2008) Accelerated decline in the Arctic sea ice cover. *Geophysical Research Letters*, *35*(1). https://doi.org/10.1029/2007GL031972

Connor, L. C., Farrell, S. L., McAdoo, D. C., Krabill, W. B., & Manizade, S. (2013). Validating ICESat over thick sea ice in the northern Canada Basin. *IEEE Transactions on Geoscience and Remote Sensing*, *51*(4), 2188-2200. https://doi.org/10.1109/TGRS.2012.2211603

Constantino, R. R., Tinto, K. J., Bell, R. E., Porter, D. F., & Jordan, T. A. (2020). Seafloor depth of George VI Sound, Antarctic Peninsula, from inversion of aerogravity data. *Geophysical Research Letters*, *47*. https://doi.org/10.1029/2020GL088654

Conway, H., Smith, B., Vaswani, P., Matsuoka, K., Rignot, E., & Claus, P. (2009). A low-frequency ice-penetrating radar system adapted for use from an airplane: Test results from Bering and Malaspina Glaciers, Alaska, USA. *Annals of Glaciology*, *50*(51), 93–97. https://doi.org/10.3189/172756409789097487

Csatho, B., Schenk, A. F., van der Veen, C. J., Babonis, G. S., Duncan, K., Rezvanbehbahani, S., et al. (2014). Laser altimetry reveals complex pattern of Greenland Ice Sheet dynamics. *Proceedings of the National Academy of Sciences*, *111*(52), 18478–18483. https://doi.org/10.1073/pnas.1411680112

Cuffey, K. M., & Paterson, W. S. B. (2010). *The Physics of Glaciers*, 4th ed., 693 pp., Butterworth-Heinemann, Burlington, Mass.

Dattler, M. E., Lenaerts, J. T. M., & Medley, B. (2019). Significant Spatial Variability in Radar-Derived West Antarctic Accumulation Linked to Surface Winds and Topography. *Geophysical Research Letters*, *46*, 13126–13134. https://doi.org/10.1029/2019GL085363

de la Peña, S., Howat, I. M., Nienow, P. W., van den Broeke, M. R., Mosley-Thompson, E., Price, S. F., et al. (2015). Changes in the firn structure of the western Greenland Ice Sheet caused by recent warming. *The Cryosphere*, *9*, 1203–1211. https://doi.org/10.5194/tc-9-1203-2015

Dow, C. F., Lee, W. S., Greenbaum, J. S., Greene, C. A., Blankenship, D. D., Poinar, K., et al. (2018). Basal channels drive active surface hydrology and transverse ice shelf fracture. *Science Advances*, *4*(6), eaao7212. https://doi.org/10.1126/sciadv.aao7212

Duncan, K., Farrell, S. L., Connor, L. N., Richter-Menge, J. & Dominguez, R. (2018). High-resolution airborne observations of sea ice pressure-ridge sail height. *Annals of Glaciology*, *59*(76), 137–147. https://doi.org/10.1017/aog.2018.2

Duncan, K., Farrell, S. L., Hutchings, J., Richter-Menge, J. (2020). Late Winter Observations of Sea Ice Pressure Ridge Sail Height. *IEEE Geoscience and Remote Sensing Letters*. https://doi.org/10.1109/LGRS.2020.3004724.

Echelmeyer, K., Clarke, T. S., & Harrison, W. D. (1991). Surficial glaciology of Jakobshavn Isbræ, West Greenland 1. Surface-morphology. *Journal of Glaciology*, *37*(127), 368–382. https://doi.org/10.3189/S0022143000005803

Enderlin, E. M., Hamilton, G., O'Neel, S., Bartholomaus, T. C., Morlighem, M., & Holt, J. W. (2016). An Empirical Approach for Estimating Stress-Coupling Lengths for Marine-Terminating Glaciers. *Frontiers in Earth Science*, *4*(104). https://doi.org/10.3389/feart.2016.00104

Fahnestock, M. A., Abdalati, W., Luo, S., & Gogineni, S. P. (2001a). Internal layer tracing and age-depth-accumulation relationships for the northern Greenland ice sheet. *Journal of Geophysical Research, 106*(D24), 33789–33797. https://doi.org/10.1029/2001JD900200

Fahnestock, M. A., Abdalati, W., Joughin, I. R., Brozena, J., & Gogineni, S. P. (2001b). High geothermal heat flow, basal melt, and the origin of rapid ice flow in central Greenland. *Science*, *294*(5550), 2338–2342. https://doi.org/10.1126/science.1065370

Farrell, S. L., Markus, T., Kwok, R., Connor, L. (2011). Laser Altimetry Sampling Strategies over Sea Ice. *Annals of Glaciology*, *52*(57), 69-76. https://doi.org/10.3189/172756411795931660

Farrell, S. L., Kurtz, N., Connor, L. N., Elder, B. C., Leuschen, C., Markus, T., et al. (2012). A first assessment of IceBridge snow and ice thickness data over Arctic sea ice. *IEEE Transactions on Geoscience and Remote Sensing*, *50*(6), 2098–2111. https://doi.org/10.1109/TGRS.2011.2170843

Farrell, S. L., Brunt, K. M., Ruth, J. M., Kuhn, J. M., Connor, L. N. & Walsh, K. M. (2015). Sea Ice Freeboard Retrieval using Digital Photon-counting Laser Altimetry. *Annals of Glaciology*, *56*(69), 167–174. https://doi.org/10.3189/2015AoG69A686

Farrell, S. L., Duncan, K., Buckley, E. M., Richter-Menge, J., & Li, R. (2020). Mapping Sea Ice Surface Topography in High Fidelity with ICESat-2. *Geophysical Research Letters*, *47*, e2020GL090708. https://doi.org/10.1029/2020GL090708

Favier, V., Agosta, C., Parouty, S., Durand, G., Delaygue, G., Gallée, H., et al. (2013). An updated and quality controlled surface mass balance dataset for Antarctica. *The Cryosphere*, *7*, 583–597. https://doi.org/10.5194/tc-7-583-2013

Felikson, D., Catania, G., Bartholomaus, T. C., Morlighem, M. & Noël, B. P. Y. (2020). Steep glacier bed knickpoints mitigate inland thinning in Greenland. *Geophysical Research Letters*, *47*. https://doi.org/10.1029/2020gl090112

Florentine, C., Harper, J. T., Johnson, J. V., & Meierbachtol, T. (2018). Radiostratigraphy Reflects the Present-Day, Internal Ice Flow Field in the Ablation Zone of Western Greenland, *Frontiers in Earth Science*, *6*. https://doi.org/10.3389/feart.2018.00044

Forster, R., Box., J. E., van den Broeke, M. R., Miège, C., Burgess, E. W., van Angelen, J. H. et al. (2014). Extensive liquid meltwater storage in firn within the Greenland ice sheet. *Nature Geoscience*, *7*(2), 95–98. https://doi.org/10.1038/ngeo2043

Frederick, B. C., Young, D. A., Blankenship, D. D., Richter, T. G., Kempf, S. D., Ferraccioli, F. & Siegert, M. J. (2016). Distribution of subglacial sediments across the Wilkes Subglacial Basin, East Antarctica. *Journal of Geophysical Research: Earth Surface*, *121*, 790–813. https://doi.org/10.1002/2015JF003760

Fretwell, P., Pritchard, H. D., Vaughan, D. G., Bamber, J. L., Barrand, N. E., Bell, R., et al. (2013). Bedmap2: improved ice bed, surface and thickness datasets for Antarctica. *The Cryosphere*, *7*(1), 375–393. https://doi.org/10.5194/tc-7-375-2013

Fricker, H. A., Carter, S. P., Bell, R. E., & Scambos, T. (2014). Active lakes of Recovery Ice Stream, East Antarctica: a bedrock-controlled subglacial hydrological system. *Journal of Glaciology*, *60*(223), 1015–1030. https://doi.org/10.3189/2014JoG14J063

Friedl, P., Seehaus, T. C., Wendt, A., Braun, M. H., & Höppner, K. (2018). Recent dynamic changes on Fleming Glacier after the disintegration of Wordie Ice Shelf, Antarctic Peninsula. *The Cryosphere*, *12*(4), 1347–1365. https://doi.org/10.5194/tc-12-1347-2018

Gabell, A., Tuckett, H., & Olson, D. (2004). The GT-1A mobile gravimeter. In *Airborne Gravity 2004–Abstracts from the ASEG-PESA Airborne Gravity 2004 Workshop: Geoscience Australia Record*, *18*, 55–61

Gardner, A. S., Moholdt, G., Arendt, A., & Wouters, B. (2012). Accelerated contributions of Canada's Baffin and Bylot Island glaciers to sea level rise over the past half century. *The Cryosphere*, *6*(5), 1103–1125. https://doi.org/10.5194/tc-6-1103-2012

Giles, K. A., Laxon, S. W., Wingham, D. J., Wallis, D. W., Krabill, W. B., Leuschen, C. J., et al. (2007). Combined airborne laser and radar altimeter measurements over the Fram Strait in May 2002. *Remote Sensing of the Environment*, *111*(2), 182–194. https://doi.org/10.1016/j.rse.2007.02.037

Giles, K. A., Laxon, S. W., & Ridout, A. L. (2008). Circumpolar thinning of Arctic sea ice following the 2007 record ice extent minimum. *Geophysical Research Letters*, *35*, L22502. https://doi.org/10.1029/2008GL035710

Gogineni, S. P., Chuah, T., Allen, C., Jezek, K. C. & Moore, R. K. (1998). An improved coherent radar depth sounder. *Journal of Glaciology*, *44*(148), 659–669. https://doi.org/10.1017/S0022143000002161

Gogineni, S. P., Tammana, D., Braaten, D. A., Leuschen, C. J., Akins, T. L., Legarsky, J. et al. (2001). Coherent radar ice thickness measurements over the Greenland ice sheet. *Journal of Geophysical Research, 106*(D24), 33761–33772. https://doi.org/10.1029/2001JD900183

Gogineni, S. P., Braaten, D., Allen, C., Paden, J., Akins, T., Kanagaratnam, P., et al. (2007). Polar Radar for Ice Sheet Measurements (PRISM). *Remote Sensing of the Environment*, *111*, 204–211. https://doi.org/10.1016/j.rse.2007.01.022

Gomez-Garcia, D., Leuschen C., Rodriguez-Morales, F., Yan, J.B., & Gogineni, P. (2014). Linear chirp generator based on direct digital synthesis and frequency multiplication for airborne FMCW snow probing radar. *Proceedings of the IEEE International Microwave Symposium*. https://doi.org/10.1109/MWSYM.2014.6848668

Greenbaum, J. S., Blankenship, D. D., Young, D. A., Richter, T. G., Roberts, J. L., Aitken, A. R. A., et al. (2015). Ocean access to a cavity beneath Totten Glacier in East Antarctica. *Nature Geoscience*, *8*, 294–298. https://doi.org/10.1038/ngeo2388

Groh, A., Ewert, H., Rosenau, R., Fagiolini, E., Gruber, C., Floricioiu, D., et al. (2014). Mass, volume and velocity of the Antarctic Ice Sheet: present-day changes and error effects. *Surveys in Geophysics*, *35*(6), 1481–1505. https://doi.org/10.1007/s10712-014-9286-y

Gudmandsen, P. E. (1975). Layer echoes in polar ice sheets. *Journal of Glaciology*, *15*(73), 95–101, https://doi.org/10.3189/S0022143000034304

Guerreiro, K., Fleury, S., Zakharova, E., Remy, F., & Kouraev, A. (2016). Potential for estimation of snow depth on Arctic sea ice from CryoSat-2 and SARAL/AltiKa missions. *Remote Sensing of Environment*, *186*, 339–349. https://doi.org/10.1016/j.rse.2016.07.013

Haas, C., Pfaffling, A., Hendricks, S., Rabenstein, L., Etienne, J.-L., & Rigor, I. (2008). Reduced ice thickness in Arctic Transpolar Drift favors rapid ice retreat. *Geophysical Research Letters*, *35*, L17501, https://doi.org/10.1029/ 2008GL034457

Hamilton, A. K. (2016), Ice-ocean interactions in Milne Fiord. *Ph.D. thesis*, *University of British Columbia*. https://open.library.ubc.ca/cIRcle/collections/ubctheses/24/items/1.0314106

Harpold, R., Yungel, J., Linkswiler, M., & Studinger, M. (2016). Intra-scan intersection method for the determination of pointing biases of an airborne altimeter. *International Journal of Remote Sensing*, *37*(3), 648-668. https://doi.org/10.1080/01431161.2015.1137989

Hawley, R. L., Courville, Z. R., Kehrl, L. M., Lutz, E. R., Osterberg, E. C., Overly, T. B., & Wong, G. J. (2014). Recent accumulation variability in northwest Greenland from ground-penetrating radar and shallow cores along the Greenland Inland Traverse. *Journal of Glaciology*, *60*(220), 375–382, 10:10.3189/2014JoG13J141

Helm, V., Humbert, A., & Miller, H. (2014). Elevation and elevation change of Greenland and Antarctica derived from CryoSat-2. *The Cryosphere*, *8*(4), 1539–1559. https://doi.org/10.5194/tc-8-1539-2014

Hofton, M., Blair, J. B., Minster, J. B., Ridgway, J. R., Williams, N. P., Bufton, J.L. & Rabine, D. L. (2000), An airborne scanning laser altimetry survey of Long Valley, California. *International Journal of Remote Sensing*, *21*(12), 2413-2437. https://doi.org/10.1080/014311600050030547

Hofton, M., Blair, J., Luthcke, S., & Rabine, D. (2008). Assessing the performance of 20–25 m footprint waveform lidar data collected in ICESat data corridors in Greenland. *Geophysical Research Letters*, *35,* L24501. https://doi.org/10.1029/2008GL035774

Hofton, M., Luthcke, S. & Blair, J. B. (2013). Estimation of ICESat intercampaign elevation biases from comparison of lidar data in East Antarctica. *Geophysical Research Letters*, *40*(21), 5698–5703. https://doi.org/10.1002/2013GL057652

Holland, D., Thomas, R. H., de Young, B., Ribergaard, M. H., & Lyberth, B. (2008). Acceleration of Jakobshavn Isbræ triggered by warm subsurface ocean waters, *Nature Geoscience*, *1*(10), 659–664. https://doi.org/10.1038/ngeo316

Holschuh, N., Christianson, K. A., Paden, J. D., Alley, R. B., & Anandakrishnan, S. (2020). Linking postglacial landscapes to glacier dynamics using swath radar at Thwaites Glacier, Antarctica. *Geology*, *48*(3), 268–272. https://doi.org/10.1130/G46772.1

Holt, J. W., Blankenship, D. D., Morse, D. L., Young, D. A., Peters, M. E., Kempf, S. D., et al. (2006). New boundary conditions for the West Antarctic Ice Sheet: Subglacial topography of the Thwaites and Smith glacier catchments. *Geophysical Research Letters*, *33*, L09502. https://doi.org/10.1029/2005GL025561

Holt, B., Johnson, M. P., Perkovic-Martin, D., & Panzer, B. (2015). Snow depth on Arctic sea ice derived from radar: In situ comparisons and time series analysis. *Journal of Geophysical Research: Oceans*, *120*(6), 4260–4287. https://doi.org/10.1002/2015JC010815

Holt, J., Truffer, M., Larsen, C., Christofferson, M., & Tober, B. (2019). Glaciers on the Brink: New Alaskan Ice thickness Constraints from Operation IceBridge Airborne Radar Sounding. *AGU Fall Meeting 2019*, C43B-07

Howat, I. M., Jezek, K., Studinger, M., MacGregor, J. A., Paden, J., Floricioiu, D., et al., (2012). Rift in Antarctic glacier: A unique chance to study ice shelf retreat. *Eos*, *93*(8), 77–88. https://doi.org/10.1029/2012EO080001

Howat, I. M., Porter, C., Smith, B. E., Noh, M. J., & Morin, P. (2019), The Reference Elevation Model of Antarctica, *The Cryosphere*, *13*, 665–674. https://doi.org/10.5194/tc-13-665-2019.

IMBIE Team (2020). Mass balance of the Greenland Ice Sheet from 1992 to 2018. *Nature*, *579*(7798), 233–239. https://doi.org/10.1038/s41586-019-1855-2

Jamieson, S. S. R., Ross, N., Greenbaum, J. S., Young, D. A., Aitken, A. R. A., Roberts, J. L., Blankenship, D. D., et al. (2016). An extensive subglacial lake and canyon system in Princess Elizabeth Land, East Antarctica. *Geology*, *44*(2), 87–90. https://doi.org/10.1130/G37220.1

Jezek, K. C., Gogineni, S. P., Wu, X., Rodriguez, E., Rodriguez-Morales, F., Hoch, A., et al. (2011). Two-Frequency Radar Experiments for Sounding Glacier Ice and Mapping the Topography of the Glacier Bed. *IEEE Transactions on Geoscience and Remote Sensing*, *49*(3), 920–929. https://doi.org/10.1109/TGRS.2010.2071387

Jezek, K. C., Wu, X., Paden, J. D., & Leuschen, C. J. (2013). Radar mapping of Isunnguata Sermia, Greenland. *Journal of Glaciology*, *59*(218), 1135–1146. https://doi.org/10.3189/2013JoG12J248

Johnson, A. J., Larsen, C. F., Murphy, N., Arendt, A. A., & Zirnheld, S. L. (2013). Mass balance in the Glacier Bay area of Alaska, USA, and British Columbia, Canada, 1995-2011, using airborne laser altimetry. *Journal of Glaciology*, *59*(216), 632–648. https://doi.org/10.3189/2013JoG12J101

Jordan, R., Picardi, G., Plaut, J., Wheeler, K., Kirchner, D., Safaeinili, A., et al. (2009), The Mars express MARSIS sounder instrument. *Planetary and Space Science*, *57*, 1975–1986. https://doi.org/10.1016/j.pss.2009.09.016

Jordan, T. M., Cooper, M. A., Schroeder, D. M., Williams, C. N., Paden, J. D., Siegert, M. J., & Bamber, J. L. (2017). Self-affine subglacial roughness: consequences for radar scattering and basal water discrimination in northern Greenland. *The Cryosphere*, *11*(3), 1247–1264. https://doi.org/10.5194/tc-11-1247-2017

Jordan, T. M., Williams, C. N., Schroeder, D. M., Martos, Y. M., Cooper, M. A., Siegert, M. J., et al. (2018). A constraint upon the basal water distribution and thermal state of the Greenland Ice Sheet from radar bed echoes. *The Cryosphere*, *12*(9), 2831–2854. https://doi.org/10.5194/tc-12-2831-2018

Joughin, I., Smith, B. E., & Holland, D. M. (2010). Sensitivity of 21st century sea level to ocean-induced thinning of Pine Island Glacier, Antarctica. *Geophysical Research Letters*, *37*, L20502. https://doi.org/10.1029/2010GL044819

Joughin, I., Smith, B. E., & Medley, B. (2014). Marine Ice Sheet Collapse Potentially Under Way for the Thwaites Glacier Basin, West Antarctica. *Science*, *344*(6185), 735–738. https://doi.org/10.1126/science.1249055

Joughin, I., Smith, B. E., & Schoof, C. G. (2019). Regularized Coulomb Friction Laws for Ice Sheet Sliding: Application to Pine Island Glacier, Antarctica. *Geophysical Research Letters*, 46, 4764–4771. https://doi.org/10.1029/2019GL082526

Joughin, I., Shean, D. E., Smith, B. E., & Floricioiu, D. (2020). A decade of variability on Jakobshavn Isbrae: ocean temperatures pace speed through influence on mélange rigidity. *The Cryosphere*, 14, 211–227. https://doi.org/10.5194/tc-14-211-2020

Kanagaratnam, P., Gogineni, S. P., Gundestrup, N. S., & Larsen, L. B. (2001). High-resolution radar mapping of internal layers at the North Greenland Ice Core Project. *Journal of Geophysical Research, 106*(D24), 33799–33811. https://doi.org/10.1029/2001JD900191

Kanagaratnam, P., Gogineni, S. P., Ramasami, V., & Braaten, D. A. (2004). A Wideband Radar for High-Resolution Mapping of Near-Surface Internal Layers in Glacial Ice. *IEEE Transactions on Geoscience and Remote Sensing*, *42*(3), 483–490. https://doi.org/10.1109/TGRS.2004.823451

Kanagaratnam, P., Markus, T., Lytle, V., Heavey, B., Jansen, P., Prescott, G., & Gogineni, S. (2007). Ultra-wideband radar measurements of thickness of snow over sea ice. *IEEE Transactions on Geoscience and Remote Sensing*, *45*(9), 2715–2724. https://doi.org/10.1109/TGRS.2007.900673

Karlsson, N. B., Dahl-Jensen, D., Gogineni, S. P., & Paden, J. D. (2013). Tracing the depth of the Holocene ice in North Greenland from radio-echo sounding data. *Annals of Glaciology*, *54*(64), 44–50. https://doi.org/10.3189/2013AoG64A057

Karlsson, N. B., Eisen, O., Dahl-Jensen, D., Freitag, J., Kipfstuhl, S., Lewis, C. C., et al. (2016). Accumulation Rates during 1311–2011 CE in North-Central Greenland Derived from Air-Borne Radar Data. *Frontiers in Earth Science*, *4*, D15106–18. https://doi.org/10.3389/feart.2016.00097

Kehrl, L. M., Joughin, I. R., Shean, D. E., Floricioiu, D., & Krieger, L. (2017). Seasonal and interannual variabilities in terminus position, glacier velocity, and surface elevation at Helheim and Kangerlussuaq Glaciers from 2008 to 2016. *Journal of Geophysical Research: Earth Surface*, *122*. https://doi.org/10.1002/2016JF004133

Khan, S. A., Kjær, K. H., Bevis, M., Bamber, J. L., Wahr, J., Kjeldsen, K. K., et al. (2014), Sustained mass loss of the northeast Greenland ice sheet triggered by regional warming. *Nature Climate Change*, *4*, 222–229. https://doi.org/10.1038/nclimate2161

Khan, S. A., Sasgen, I., Bevis, M., van Dam, T., Bamber, J. L., Wahr, J., et al. (2016). Geodetic measurements reveal similarities between post-Last Glacial Maximum and present-day mass loss from the Greenland ice sheet. *Science Advances*, *2*(9), e1600931–e1600931. https://doi.org/10.1126/sciadv.1600931

Khazendar, A., Rignot, E. J., Schroeder, D. M., Seroussi, H., Schodlok, M. P., Scheuchl, B., et al. (2016), Rapid submarine ice melting in the grounding zones of ice shelves in West Antarctica. *Nature Communications*, *7*. https://doi.org/10.1038/ncomms13243

Khazendar, A., Fenty, I. G., Carroll, D., Gardner, A., Lee, C. M., Fukumori, I., et al. (2019). Interruption of two decades of Jakobshavn Isbrae acceleration and thinning as regional ocean cools. *Nature Geoscience*, *12*, 277–283. https://doi.org/10.1038/41561-019-0329-3

King, J., Howell, S., Derksen, C., Rutter, N., Toose, P., Beckers, J. F., et al. (2015), Evaluation of Operation IceBridge quick-look snow depth estimates on sea ice. *Geophysical Research Letters*, *42*(21), 9302–9310. https://doi.org/10.1002/2015GL066389

Koenig, L. S., Studinger, M., Martin, S., & Sonntag, J. G. (2010). Polar Airborne Observations Fill Gap in Satellite Data. *Eos*, *91*(38), 333–334. https://doi.org/10.1029/2010EO380002

Koenig, L. S., Ivanoff, A., Alexander, P. M., MacGregor, J. A., Fettweis, X., Panzer, B., et al. (2016). Annual Greenland accumulation rates (2009–2012) from airborne snow radar. *The Cryosphere*, *10*, 1739–1752. https://doi.org/10.5194/tc-10-1739-2016

Krabill, W. B., Thomas, R. H., Martin, C. F., Swift, R. N., & Frederick, E. B. (1995). Accuracy of airborne laser altimetry over the Greenland ice sheet. *International Journal of Remote Sensing*, *16*(7), 1211–1222. https://doi.org/10.1080/01431169508954472

Krabill, W. B., Abdalati, W., Frederick, E. B., Manizade, S. S., Martin, C., Sonntag, J. G., et al. (2000), Greenland ice sheet: High-elevation balance and peripheral thinning. *Science*, *289*(5478), 428–430. https://doi.org/10.1126/science.289.5478.428

Krabill, W. B., Abdalati, W., Frederick, E. B., Manizade, S. S., Martin, C. F., Sonntag, J. G., et al. (2002), Aircraft laser altimetry measurement of elevation changes of the Greenland Ice Sheet: technique and accuracy assessment. *Journal of Geodynamics*, *34*(3-4), 357–376. https://doi.org/10.1016/S0264-3707(02)00040-6

Kuipers Munneke, P., McGrath, D., Medley, B., Luckman, A., Bevan, S., Kulessa, B., et al. (2017), Observationally constrained surface mass balance of Larsen C ice shelf, Antarctica. *The Cryosphere*, *11*, 2411–2426. https://doi.org/10.5194/tc-11-2411-2017

Kurtz, N. T., Markus, T., Cavalieri, D. J., Sparling, L. C., Krabill, W. B., Gasiewski, A. J., & Sonntag, J. G., (2009). Estimation of sea ice thickness distributions through the combination of snow depth and satellite laser altimetry data. *Journal of Geophysical Research, 114*, C10007. https://doi.org/10.1029/2009JC005292

Kurtz, N. T., & Farrell, S. L. (2011). Large-scale surveys of snow depth on Arctic sea ice from Operation IceBridge. *Geophysical Research Letters*, *38*, L20505. https://doi.org/10.1029/2011GL049216

Kurtz, N. T., & Markus, T. (2012). Satellite observations of Antarctic sea ice thickness and volume. *Journal of Geophysical Research: Oceans*, *117*(C8). https://doi.org/10.1029/2012JC008141

Kurtz, N. T., Farrell, S. L., Studinger, M., Galin, N., Harbeck, J. P., Lindsay, R., et al. (2013). Sea ice thickness, freeboard, and snow depth products from Operation IceBridge airborne data. *The Cryosphere*, *7*, 1035–1056. https://doi.org/10.5194/tc-7-1035-2013

Kurtz, N. T., Galin, N., & Studinger, M. (2014). An improved CryoSat-2 sea ice freeboard retrieval algorithm through the use of waveform fitting. *The Cryosphere*, *8*, 1217–1237. https://doi.org/10.5194/tc-8-1217-2014

Kurtz, N., Studinger, M., Harbeck, J. P., Onana, V. D., & Yi, D. (2015). IceBridge L4 Sea Ice Freeboard, Snow Depth, and Thickness, Version 1. Boulder, Colorado USA, NASA National Snow and Ice Data Center Distributed Active Archive Center. https://doi.org/10.5067/G519SHCKWQV6

Kwok, R., Schweiger, A., Rothrock, D. A., Pang, S., & Kottmeier, C. (1998). Sea ice motion from satellite passive microwave imagery assessed with ERS SAR and buoy motions. *Journal of Geophysical Research: Oceans*, *103*(C4), 8191–8214. https://doi.org/10.1029/97JC03334

Kwok, R., & Cunningham, G. (2008). ICESat over Arctic sea ice: Estimation of snow depth and ice thickness. *Journal of Geophysical Research: Oceans, 113*, C08010. https://doi.org/10.1029/2008JC004753

Kwok, R., & Rothrock, D. A. (2009). Decline in Arctic sea ice thickness from submarine and ICESat records: 1958-2008. *Geophysical Research Letters*, *36*(15). https://doi.org/10.1029/2009GL039035

Kwok, R., Cunningham, G. F., Wensnahan, M., Rigor, I., Zwally, H. J., & Yi, D. (2009). Thinning and volume loss of the Arctic Ocean sea ice cover: 2003-2008. *Journal of Geophysical Research: Oceans, 114*, C07005. https://doi.org/10.1029/2009JC005312

Kwok, R., Panzer, B., Leuschen, C., Pang, S., Markus, T, Holt, B., & Gogineni, S. (2011). Airborne surveys of snow depth over Arctic sea ice. *Journal of Geophysical Research: Oceans*, *116*(C11). https://doi.org/10.1029/2011JC007371

Kwok, R., Cunningham, G. F., Manizade, S. S., & Krabill, W. B. (2012). Arctic sea ice freeboard from IceBridge acquisitions in 2009: Estimates and comparisons with ICESat. *Journal of Geophysical Research: Oceans*, *117*(C2). https://doi.org/10.1029/2011JC007654

Kwok, R. (2014). Declassified high-resolution visible imagery for Arctic sea ice investigations: An overview. *Remote Sensing of the Environment*, *142*, 44–56. https://doi.org/10.1016/j.rse.2013.11.015.

Kwok, R., & Maksym, T. (2014). Snow depth of the Weddell and Bellingshausen sea ice covers from IceBridge surveys in 2010 and 2011: An examination. *Journal of Geophysical Research: Oceans*, *119*(7), 4141–4167. https://doi.org/10.1002/2014JC009943

Kwok, R. (2015). Sea ice convergence along the Arctic coasts of Greenland and the Canadian Arctic Archipelago: Variability and extremes (1992–2014). *Geophysical Research Letters*, *42*(18), 7598–7605. https://doi.org/10.1002/2015GL065462

Kwok, R., & Cunningham, G. F. (2015). Variability of Arctic sea ice thickness and volume from CryoSat-2. *Philosophical Transactions of the Royal Society A*, *373*(2045). https://doi.org/10.1098/rsta.2014.0157

Kwok, R., Kurtz, N. T., Brucker, L., Ivanoff, A., Newman, T., Farrell, S. L., et al. (2017). Intercomparison of snow depth retrievals over Arctic sea ice from radar data acquired by Operation IceBridge. *The Cryosphere*, *11*(6), 2571–2593. https://doi.org/10.5194/tc-11-2571-2017

Kwok, R., & Markus, T. (2018). Potential basin-scale estimates of Arctic snow depth with sea ice freeboards from CryoSat-2 and ICESat-2: An exploratory analysis. *Advances in Space Research*, *62*(6), 1243–1250. https://doi.org/10.1016/j.asr.2017.09.007

Kwok, R., & Kacimi, S. (2018). Three years of sea ice freeboard, snow depth, and ice thickness of the Weddell Sea from Operation IceBridge and CryoSat-2. *The Cryosphere*, *12*(8), 2789–2801, 10.5194/tc-12-2789-2018

Kwok, R., Kacimi, S., Markus, T., Kurtz, N. T., Studinger, M., Sonntag, J. G., et al. (2019). ICESat-2 Surface Height and Sea Ice Freeboard Assessed With ATM Lidar Acquisitions From Operation IceBridge. *Geophysical Research Letters*, *46*, 2019GL084976–9. https://doi.org/10.1029/2019GL084976

Kwok, R., Kacimi, S., Webster, M. A., Kurtz, N. T., & Petty, A. A. (2020). Arctic snow depth and sea ice thickness from ICESat-2 and CryoSat-2 freeboards: A first examination. *Journal of Geophysical Research: Oceans*, *125*, e2019JC016008. https://doi.org/10.1029/2019JC016008

Landy, J. C., Ehn, J. K., & Barber, D. G. (2015). Albedo feedback enhanced by smoother Arctic sea ice. *Geophysical Research Letters*, *42*(24), 10,714–10,720. https://doi.org/10.1002/2015GL066712

Landy, J. A., Petty, A., Tsamados, M. C. & Stroeve, J. (2020). Sea ice roughness overlooked as a key source of uncertainty in Cryosat-2 ice freeboard retrievals. *Journal of Geophysical Research: Oceans*. https://doi.org/10.1029/2019JC015820

Larsen, C. F., Burgess, E. W., Arendt, A. A., O'Neel, S., Johnson, A. J., & Keinholz, C. (2015). Surface melt dominates Alaska glacier mass balance. *Geophysical Research Letters*, *42*. https://doi.org/10.1002/2015GL064349

Law, R., Arnold, N., Benedek, C., Tedesco, M., Banwell, A., & Willis, I. (2020). Over-winter persistence of supraglacial lakes on the Greenland Ice Sheet: results and insights from a new model. *Journal of Glaciology*, *66*(257), 362–372. https://doi.org/10.1017/jog.2020.7

Laxon, S. W., Giles, K. A., Ridout, A. L., Wingham, D. J., Willatt, R., Cullen, R., et al. (2013). CryoSat Estimates of Arctic Sea Ice Volume. *Geophysical Research Letters, 40*(4), 732–737. https://doi.org/10.1002/grl.50193

Legarsky, J. J., Gogineni, P., & Akins, T. L. (2001). Focused synthetic-aperture radar processing of ice-sounder data collected over the Greenland ice sheet. *IEEE Transactions on Geoscience and Remote Sensing*, *39*(10), 2109–2117

Legarsky, J., & Gao, X. (2006). Internal Layer Tracing and Age–Depth Relationship From the Ice Divide Toward Jakobshavn, Greenland. *IEEE Geoscience and Remote Sensing Letters*, *3*(4), 471–475. https://doi.org/10.1109/LGRS.2006.877749

Lenaerts, J. T., van den Broeke, M. R., van de Berg, W. J., van Meijgaard, W. J., & Kuipers Munneke, P. (2012). A new, high-resolution surface mass balance map of Antarctica (1979–2010) based on regional atmospheric climate modeling. *Geophysical Research Letters*, *39*(4). https://doi.org/10.1029/2011GL050713

Lenaerts, J. T., Ligtenberg, S. R., Medley, B., Van de Berg, W. J., Konrad, H., Nicolas, J. P., et al. (2018), Climate and surface mass balance of coastal West Antarctica resolved by regional climate modelling. *Annals of Glaciology*, *59*(76), 29–41. https://doi.org/10.1017/aog.2017.42

Lenaerts, J. T. M., Medley, B., van den Broeke, M. R., & Wouters, B. (2019). Observing and Modeling Ice Sheet Surface Mass Balance. *Reviews of Geophysics*, *57*(2), 376–420. https://doi.org/10.1029/2018RG000622

Lewis, C., Gogineni, S., Rodriguez-Morales, F., Panzer, B., Stumpf, T., Paden, J., & Leuschen, C. (2015). Airborne fine-resolution UHF radar: an approach to the study of englacial reflections, firn compaction and ice attenuation rates. *Journal of Glaciology*, *61*(225), 89–100. https://doi.org/10.3189/2015JoG14J089

Lewis, G., Osterberg, E., Hawley, R., Whitmore, B., Marshall, H.-P., & Box, J. (2017). Regional Greenland accumulation variability from Operation IceBridge airborne accumulation radar. *The Cryosphere*, *11*(2), 773–788. https://doi.org/10.5194/tc-11-773-2017

Leysinger-Vieli, G. J. M. C., Martin, C., Hindmarsh, R. C. A., & Lüthi, M. P. (2018). Basal freeze-on generates complex ice-sheet stratigraphy. *Nature Communications*, *9*(1), 1–13. https://doi.org/10.1038/s41467-018-07083-3

Li, J., Paden, J. D., Leuschen, C. J., Rodriguez-Morales, F., Hale, R. D., Arnold, E., et al. (2013), High-Altitude Radar Measurements of Ice Thickness Over the Antarctic and Greenland Ice Sheets as a Part of Operation IceBridge. *IEEE Transactions on Geoscience and Remote Sensing*, *51*(2), 742–754. https://doi.org/10.1109/TGRS.2012.2203822

Lilien, D. A., Joughin, I. R., Smith, B. E., & Shean, D. E. (2018). Changes in flow of Crosson and Dotson ice shelves, West Antarctica, in response to elevated melt. *The Cryosphere*, *12*, 1415–1431. https://doi.org/10.5194/tc-12-1415-2018

Lindsay, R., Haas, C., Hendricks, S., Hunkeler, P., Kurtz, N., Paden, J., et al. (2012). Seasonal forecasts of Arctic sea ice initialized with observations of ice thickness. *Geophysical Research Letters*, *39*(21). https://doi.org/10.1029/2012GL053576

Lindsay, R., & Schweiger, A. (2015). Arctic sea ice thickness loss determined using subsurface, aircraft, and satellite observations. *The Cryosphere*, *9*, 269–283. https://doi.org/10.5194/tc-9-269-2015

Livingstone, S. J., Chu, W., Ely, J. C., & Kingslake, J. (2017). Paleofluvial and subglacial channel networks beneath Humboldt Glacier, Greenland. *Geology*. https://doi.org/10.1130/G38860.1

Maaß, N., Kaleshke, L., Tian-Kunze, X., & Drusch, M. (2013). Snow thickness retrieval over thick Arctic sea ice using SMOS satellite data. *The Cryosphere*, *7*, 1971–1989. https://doi.org/10.5194/tc-7-1971-2013

MacFerrin, M., Machguth, H., van As, D., Charalampidis, C., Stevens, C. M., Heilig, A., et al. (2019). Rapid expansion of Greenland's low-permeability ice slabs. *Nature*, *573*(7774), 403–407. https://doi.org/10.1038/s41586-019-1550-3

MacGregor, J. A., Fahnestock, M. A., Catania, G. A., Paden, J. D., Gogineni, S. P., Young, S. K., et al. (2015a), Radiostratigraphy and age structure of the Greenland Ice Sheet. *Journal of Geophysical Research: Earth Surface*, *120*(2), 212–241. https://doi.org/10.1002/2014JF003215

MacGregor, J. A. Li, J., Paden, J. D., Catania, G. A., Clow, G. D., Fahnestock, M. A., et al. (2015b). Radar attenuation and temperature within the Greenland Ice Sheet. *Journal of Geophysical Research: Earth Surface*, *120*(6), 983–1008. https://doi.org/10.1002/2014JF003418

MacGregor, J. A., W. T. Colgan, M. A. Fahnestock, M. Morlighem, G. A. Catania, J. D. Paden, & S. P. Gogineni (2016a). Holocene deceleration of the Greenland Ice Sheet. *Science*, *351*(6273), 590–593. https://doi.org/10.1126/science.aab1702

MacGregor, J. A., Fahnestock, M. A., Catania, G. A., Aschwanden, A. Clow, G. D., Colgan, W. T., et al. (2016b), A synthesis of the basal thermal state of the Greenland Ice Sheet. *Journal of Geophysical Research: Earth Surface*, *121*(7), 1328–1350. https://doi.org/10.1002/2015JF003803

MacGregor, J. A., Bottke Jr, W. F., Fahnestock, M. A., Harbeck, J. P., Kjær, K. H., Paden, J. D., et al. (2019). A Possible Second Large Subglacial Impact Crater in Northwest Greenland. *Geophysical Research Letters*, *46*, E12S09–9. https://doi.org/10.1029/2018GL078126

MacKie, E. J., Schroeder, D. M., Caers, J., Siegfried, M. R., & Scheidt, C. (2020). Antarctic Topographic Realizations and Geostatistical Modeling Used to Map Subglacial Lakes. *Journal of Geophysical Research: Earth Surface*, *125*, e2019JF005420. https://doi.org/10.1029/2019JF005420

Markus, T., Neumann, T., Martino, A., Abdalati, W., Brunt, K., Csatho, B. et al. (2017). The Ice, Cloud, and land Elevation Satellite-2 (ICESat-2): Science requirements, concept, and implementation. *Remote Sensing of the Environment*, *190*, 260–273. https://doi.org/10.1016/j.rse.2016.12.029

Martin, C. F., Krabill, W. B., Manizade, S. S., Russell, R. L., Sonntag, J. G., Swift, R. N., & Yungel, J. K. (2012). Airborne Topographic Mapper Calibration Procedures and Accuracy Assessment. *NASA Technical Report* TM-2012-215891, 32 pp., NASA Center for AeroSpace Information, Hanover, MD

Martin-Español, A., Bamber, J., & Zammit-Mangion, A. (2017). Constraining the mass balance of East Antarctica. *Geophysical Research Letters*, *44*(9), 4168–4175. https://doi.org/10.1002/2017GL072937

Massom, R. A., Eicken, H., Hass, C., Jeffries, M., Drinkwater, M., Sturm, M., et al. (2001). Snow on Antarctic sea ice. *Reviews of Geophysics*, *39*(3), 413-445. https://doi.org/10.1029/2000RG000085

Maykut, G. A., & Untersteiner, N. (1971). Some results from a time-dependent thermodynamic model of sea ice. *Journal of Geophysical Research, 76*, 1550-1575. https://doi.org/10.1029/JC076i006p01550

McAdoo, D. C., Farrell, S. L., Laxon, S. W., Ridout, A. L., Zwally, H. J., & Yi, D. (2013). Gravity of the Arctic Ocean from satellite data with validations using airborne gravimetry: oceanographic implications. *Journal of Geophysical Research: Oceans, 118*, 917–930. https://doi.org/10.1002/jgrc.20080

Medley, B., Joughin, I., Das, S. B., Steig, E. J., Conway, H. Gogineni, S., et al. (2013). Airborne-radar and ice-core observations of annual snow accumulation over Thwaites Glacier, West Antarctica confirm the spatiotemporal variability of global and regional atmospheric models. *Geophysical Research Letters*, *40*, 3649–3654. https://doi.org/10.1002/grl.50706

Medley, B., Joughin, I., Smith, B. E., Steig, E. J., Conway, H. Gogineni, S., et al. (2014). Constraining the recent mass balance of Pine Island and Thwaites glaciers, West Antarctica, with airborne observations of snow accumulation. *The Cryosphere*, *8*, 1375–1392. https://doi.org/10.5194/tc-8-1375-2014

Medley, B., Ligtenberg, S. R. M., Joughin, I., van den Broeke, M. R., Gogineni, S., & Nowicki, S. (2015). Antarctic firn compaction rates from repeat-track airborne radar data: I. Methods. *Annals of Glaciology*, *56*(70), 155–166. https://doi.org/10.3189/2015AoG70A204

Medrzycka, D., Copland, L., Van Wychen, W. & Burgess, D. (2019). Seven decades of uninterrupted advance of Good Friday Glacier, Axel Heiberg Island, Arctic Canada. *Journal of Glaciology*, *65*(251), 440–452. https://doi.org/10.1017/jog.2019.21

Miège, C., Forster, R. R., Brucker, L., Koenig, L. S., Solomon, D. K., Paden, J. D., et al. (2016). Spatial extent and temporal variability of Greenland firn aquifers detected by ground and airborne radars. *Journal of Geophysical Research: Earth Surface*, *121*. https://doi.org/10.1002/2016JF003869

Millan, R., Rignot, E. J., Bernier, V., Morlighem, M., & Dutrieux, P. (2017). Bathymetry of the Amundsen Sea Embayment sector of West Antarctica from Operation IceBridge gravity and other data. *Geophysical Research Letters*, *44*. https://doi.org/10.1002/2016GL072071

Millan, R., Rignot, E. J., Mouginot, J., Wood, M., Bjørk, A. A., & Morlighem, M. (2018). Vulnerability of Southeast Greenland Glaciers to Warm Atlantic Water From Operation IceBridge and Ocean Melting Greenland Data. *Geophysical Research Letters*, *45*. https://doi.org/10.1002/2017GL076561

Millan, R., St Laurent, P., Rignot, E. J., Morlighem, M., Mouginot, J., & Scheuchl, B. (2020). Constraining an Ocean Model Under Getz Ice Shelf, Antarctica, Using A Gravity-Derived Bathymetry. *Geophysical Research Letters*, *47*(13), 51–11. https://doi.org/10.1029/2019GL086522

Miller, J. Z., Long, D. G., Jezek, K. C., Johnson, J. T., Brodzik, M. J., Shuman, C. A., et al. (2020). Brief communication: Mapping Greenland's perennial firn aquifers using enhanced-resolution L-band brightness temperature image time series. *The Cryosphere*, *14*, 2809–2817. https://doi.org/10.5194/tc-14-2809-2020

Montgomery, L., Koenig, L., & Alexander, P. (2018). The SUMup dataset: compiled measurements of surface mass balance components over ice sheets and sea ice with analysis over Greenland. *Earth System Science Data*, *10*(4), 1959–1959. https://doi.org/doi:10.5194/essd-10-1959-2018

Montgomery, L., Koenig, L., Lenaerts, J. T., & Munneke, P. K. (2020). Accumulation rates (2009–2017) in Southeast Greenland derived from airborne snow radar and comparison with regional climate models. *Annals of Glaciology*. https://doi.org/10.1017/aog.2020.8

Morlighem, M., Rignot, E. J., Seroussi, H., Larour, E. Y., Ben Dhia, H., & Aubry, D. (2011). A mass conservation approach for mapping glacier ice thickness. *Geophysical Research Letters*, *38*. https://doi.org/10.1029/2011GL048659

Morlighem, M., Rignot, E. J., Mouginot, J., Seroussi, H., & Larour, E. Y. (2014). Deeply incised submarine glacial valleys beneath the Greenland ice sheet. *Nature Geoscience*, *7*(6), 418–422. https://doi.org/10.1038/ngeo2167

Morlighem, M., Williams, C. N., Rignot, E., An, L., Arndt, J. E., Bamber, J. L., et al. (2017). BedMachine v3: Complete Bed Topography and Ocean Bathymetry Mapping of Greenland From Multibeam Echo Sounding Combined With Mass Conservation. *Geophysical Research Letters*, *44*(21), 11,051–11,061. https://doi.org/10.1002/2017GL074954

Morlighem, M., Rignot, E., Binder, T., Blankenship, D., Drews, R., Eagles, G., et al. (2019). Deep glacial troughs and stabilizing ridges unveiled beneath the margins of the Antarctic ice sheet. *Nature Geoscience*, *13*, 132–137. https://doi.org/10.1038/s41561-019-0510-8

Mortensen, J., Bendtsen, J., Motyka, R., Lennert, K., Truffer, M., Fahnestock, M., Rysgaard, S. (2013). On the seasonal freshwater stratification in the proximity of fast-flowing tidewater outlet glaciers in a sub-Arctic sill fjord. *Journal of Geophysical Research: Oceans*, *118*, 1382–1395. https://doi.org/10.1002/jgrc.20134

Mottram, R., Hansen, N., Kittel, C., van Wessem, M., Agosta, C., Amory, C., et al. (in press). What is the Surface Mass Balance of Antarctica? An Intercomparison of Regional Climate Model Estimates. *The Cryosphere*. https://doi.org/10.5194/tc-2019-333

Mouginot, J., Rignot, E., Gim, Y., Kirchner, D., Le Meur, E. (2014). Low-frequency radar sounding of ice in East Antarctica and southern Greenland. *Annals of Glaciology*, *55*(67), 138–146. https://doi.org/10.3189/2014AoG67A089

Mouginot, J., Rignot, E. J., Scheuchl, B., Fenty, I., Khazendar, A., Morlighem, M., et al. (2015). Fast retreat of Zachariæ Isstrøm, northeast Greenland. *Science*, *350*(6266), 1357–1361. https://doi.org/10.1126/science.aac7111

Mouginot, J., A. A. Bjørk, R. Millan, B. Scheuchl, & E. J. Rignot (2018). Insights on the Surge Behavior of Storstrømmen and L. Bistrup Brae, Northeast Greenland, Over the Last Century, *Geophysical Research Letters*, *45*. https://doi.org/10.1029/2018GL079052

Mouginot, J., Rignot, E. J., Bjørk, A. A., van den Broeke, M. R., Millan, R., Morlighem, M., et al. (2019). Forty-six years of Greenland Ice Sheet mass balance from 1972 to 2018. *Proceedings of the National Academy of Sciences*, *116*(19), 9239–9244. https://doi.org/10.7280/D1MM37

Münchow, A., Padman, L., Washam, P., & Nicholls, K. W. (2016). The Ice Shelf of Petermann Gletscher, North Greenland, and Its Connection to the Arctic and Atlantic Oceans. *Oceanography*, *29*(4), 84–95. https://doi.org/10.5670/oceanog.2016.101

Muto, A., Anandakrishnan, S., & Alley, R. B. (2013). Subglacial bathymetry and sediment layer distribution beneath the Pine Island Glacier ice shelf, West Antarctica, modeled using aerogravity and autonomous underwater vehicle data. *Annals of Glaciology*, *54*(64), 27–32. https://doi.org/10.3189/2013AoG64A110

Neumann, T. A., Martino, A. J., Markus, T., Bae, S., Bock, M. R., Brenner, A. C. et al. (2019). The Ice, Cloud, and Land Elevation Satellite – 2 mission: A global geolocated photon product derived from the Advanced Topographic Laser Altimeter System *Remote Sensing of the Environment*, *233*, 111325. https://doi.org/10.1016/j.rse.2019.111325

Newman, T., Farrell, S. L., Richter-Menge, J., Connor, L. N., Kurtz, N. T., Elder, B. C., & McAdoo, D. (2014). Assessment of radar-derived snow depth over Arctic sea ice. *Journal of Geophysical Research, 119*, 8578– 8602. https://doi.org/10.1002/2014JC010284

Nielsen, L. T., Karlsson, N. B., & Hvidberg, C. (2015). Large-scale reconstruction of accumulation rates in northern Greenland from radar data. *Annals of Glaciology*, *56*(70), 70–78. https://doi.org/10.3189/2015AoG70A062

Nilsson, J., Sandberg Sørensen, L., Barletta, V. R., & Forsberg, R. (2015). Mass changes in Arctic ice caps and glaciers: implications of regionalizing elevation changes. *The Cryosphere*, *9*(1), 139–150. https://doi.org/10.5194/tc-9-139-2015

Noël, B., van de Berg, W. J., Lhermitte, S., Wouters, B., Machguth, H., Howat, I. M., et al. (2017). A tipping point in refreezing accelerates mass loss of Greenland's glaciers and ice caps. *Nature Communications*, *8*(1), 1–8. https://doi.org/10.1038/ncomms14730

Nolin, A. W., & Mar, E. (2019). Arctic Sea Ice Surface Roughness Estimated from Multi-Angular Reflectance Satellite Imagery. *Remote Sensing*, *11*(1). https://doi.org/10.3390/rs11010050

Onana, V. D., Kurtz, N. T., Farrell, S. L., Koenig, L. S., Studinger, M., & Harbeck, J. P. (2013). A Sea-Ice Lead Detection Algorithm for Use With High-Resolution Airborne Visible Imagery. *IEEE Transactions on Geoscience and Remote Sensing*, *51*, 38–56. https://doi.org/10.1109/TGRS.2012.2202666

Oswald, G. K. A., Rezvanbehbahani, S., & Stearns, L. A. (2018). Radar evidence of ponded subglacial water in Greenland. *Journal of Glaciology*, *64*(247)*,* 711–729. https://doi.org/10.1017/jog.2018.60

Paden, J. D., Akins, T. L., Dunson, D., Allen, C., & Gogineni, S. P. (2010). Ice-sheet bed 3-D tomography. *Journal of Glaciology*, *56*(195), 3–11. https://doi.org/10.3189/002214310791190811

Palmer, S. J., Dowdeswell, J. A., Christoffersen, P., Young, D. A., Blankenship, D. D., Greenbaum, J. S., et al. (2013). Greenland subglacial lakes detected by radar. *Geophysical Research Letters*, *40*(23), 6154–6159. https://doi.org/10.1002/2013GL058383

Panton, C., & Karlsson, N. B. (2015). Automated mapping of near bed radio-echo layer disruptions in the Greenland Ice Sheet. *Earth and Planetary Science Letters*, *432*(C), 323–331. https://doi.org/10.1016/j.epsl.2015.10.024

Panzer, B., Gomez-Garcia, D., Leuschen, C., Paden, J., Rodriguez-Morales, F., Patel, A., et al. (2013). An ultra-wideband, microwave radar for measuring snow thickness on sea ice and mapping near-surface internal layers in polar firn. *Journal of Glaciology*, *59*(214). https://doi.org/10.3189/2013JoG12J128

Parizek, B. R., Christianson, K., Anandakrishnan, S., Alley, R. B., Walker, R. T., Edwards, R. A., et al. (2013). Dynamic (in) stability of Thwaites Glacier, West Antarctica. *Journal of Geophysical Research: Earth Surface*, *118*(2), 638–655. https://doi.org/10.1002/jgrf.20044

Patel, A. (2009). Signal Generation for FMCW Ultra-Wideband Radar. *MsC. Thesis*, The University of Kansas

Paxman, G. J. R., Austermann, J., & Tinto, K. J., (2021). A fault-bounded palaeo-lake basin preserved beneath the Greenland Ice Sheet. *Earth and Planetary Science Letters*, *553*. https://doi.org/10.1016/j.epsl.2020.116647

Perovich, D. K., Meier, W., Tschudi, M., Farrell, S., Gerland, S. & Hendricks, S. (2015). Sea ice, in Arctic Report Card 2015. http://arctic.noaa.gov/Report-Card/Report-Card-2015/ArtMID/5037/ArticleID/217/Sea-Ice

Perovich, D. K., Meier, W., Tschudi, M., Farrell, S., Hendricks, S., Gerland, S., et al. (2017). Sea ice, in Arctic Report Card 2017, http://www.arctic.noaa.gov/Report-Card/Report-Card-2017/ArtMID/7798/ArticleID/699/Sea-Ice

Peters, M. E., Blankenship, D. D., & Morse, D. L. (2005). Analysis techniques for coherent airborne radar sounding: Application to West Antarctic ice streams. *Journal of Geophysical Research, 110*(B6), B06303. https://doi.org/10.1029/2004JB003222

Petty, A. A., Tsamados, M. C., Kurtz, N. K., Farrell, S. L., Newman, T., Harbeck, J. P., et al. (2016). Characterizing Arctic sea ice topography using high-resolution IceBridge data. *The Cryosphere*, *10*(3), 1161–1179. https://doi.org/10.5194/tc-10-1161-2016

Petty, A. A., Tsamados, M. C., & Kurtz, N. T. (2017). Atmospheric form drag coefficients over Arctic sea ice using remotely sensed ice topography data, Spring 2009–2015. *Journal of Geophysical Research: Earth Surface*, *122*(8), 1472–1490. https://doi.org/10.1002/2017JF004209

Petty, A. A., Webster, M., Boisvert, L., & Markus, T. (2018). The NASA Eulerian Snow on Sea Ice Model (NESOSIM) v1.0: initial model development and analysis. *Geoscientific Model Development*, *11*, 4577–4602. https://doi.org/10.5194/gmd-11-4577-2018

Polashenski, C., Perovich, D., & Courville, Z. (2012). The mechanisms of sea ice melt pond formation and evolution. *Journal of Geophysical Research: Oceans*, *117*(C1), C01001. https://doi.org/10.1029/2011JC007231

Porter, C., Morin, P., Howat, I., Noh, M.-J., Bates, B., Peterman, K., et al. (2018). ArcticDEM Release 7. https://doi.org/10.7910/DVN/OHHUKH

Porter, D. F., Tinto, K. J., Boghosian, A., Cochran, J. R., Bell, R. E., Mazinade, S., & Sonntag, J. (2014). Bathymetric Controls On Observed Tidewater Glacier Retreat In Northwest Greenland. *Earth and Planetary Science Letters*, *401*, 40–46. https://doi.org/10.1016/j.epsl.2014.05.058

Porter, D. F., Tinto, K. J., Boghosian, A. L., Csatho, B., Bell, R. E., & Cochran, J. R. (2018). Identifying Spatial Variability in Greenland's Outlet Glacier Response to Ocean Heat. *Frontiers in Earth Science*, *6*, F01005–13. https://doi.org/10.3389/feart.2018.00090

Pritchard, H. D., Arthern, R. J., Vaughan, D. G., & Edwards, L. (2009). Extensive dynamic thinning on the margins of the Greenland and Antarctic ice sheets. *Nature*, *461*(7266), 971–975. https://doi.org/10.1038/nature08471

Raney, R. K., Leuschen, C. J., & Jose, M. (2008). Pathfinder Advanced Radar Ice Sounder: PARIS. *IGARSS 2008*. https://doi.org/10.1109/IGARSS.2008.4779354

Richardson, C., Aarholt, E., Hamran, S. E., Holmlund, P., & Isaksson, E. (1997). Spatial distribution of snow in western Dronning Maud Land, East Antarctica, mapped by a ground-based snow radar. *Journal of Geophysical Research, 102*(B9), 20343–20353

Rignot, E. J., & Jacobs, S. S. (2002). Rapid Bottom Melting Widespread near Antarctic Ice Sheet Grounding Lines. *Science*, *296*(5575), 2020–2023. https://doi.org/10.1126/science.1070942

Rignot, E., Mouginot, J., Larsen, C. F., Gim, Y., & Kirchner, D. (2013). Low-frequency radar sounding of temperate ice masses in Southern Alaska. *Geophysical Research Letters*, *40*(20), 5399–5405. https://doi.org/10.1002/2013GL057452

Rignot, E. J., Mouginot, J., Morlighem, M., Seroussi, H., & Scheuchl, B. (2014). Widespread, rapid grounding line retreat of Pine Island, Thwaites, Smith, and Kohler glaciers, West Antarctica, from 1992 to 2011. *Geophysical Research Letters*, *41*, 1–8. https://doi.org/10.1002/2014GL060140

Rignot, E. J., Fenty, I., Xu, Y., & Cai, C. (2015). Undercutting of marine-terminating glaciers in West Greenland. *Geophysical Research Letters*, *42*(14), 5909-5917. https://doi.org/10.1002/2015GL064236

Rignot, E. J., Fenty, I., Xu, Y., Cai, C., Velicogna, I., Cofaigh, C. Ó, et al. (2016). Bathymetry data reveal glaciers vulnerable to ice-ocean interaction in Uummannaq and Vaigat glacial fjords, West Greenland. *Geophysical Research Letters*, *43*(6), 2667-2674. https://doi.org/10.1002/2016GL067832

Rignot, E. J., Mouginot, J., Scheuchl, B., van den Broeke, M. R., van Wessem, M. J., & Morlighem, M. (2019). Four decades of Antarctic Ice Sheet mass balance from 1979–2017. *Proceedings of the National Academy of Sciences*, *116*(4), 1095–1103. https://doi.org/10.1073/pnas.1812883116

Richter-Menge, J. A., & Farrell, S. L. (2013). Arctic sea ice conditions in Spring 2009–2013 prior to melt. *Geophysical Research Letters*, *40*(22), 5888–5893. https://doi.org/10.1002/2013GL058011

Robin, G. de Q., Drewry, D. J., & Meldrum, D. T. (1977). International studies of ice sheet and bedrock. *Philosophical Transactions of the Royal Society of London Series B*, *279*(963), 185–196. https://doi.org/10.1098/rstb.1977.0081

Rodríguez-Morales, F., Gogineni, S., Leuschen, C. J., Paden, J. D., Li, J., Lewis, C. C., et al. (2013). Advanced Multifrequency Radar Instrumentation for Polar Research. *IEEE Transactions on Geoscience and Remote Sensing*, *52*(5), 2824–2842. https://doi.org/10.1109/TGRS.2013.2266415

Rodriguez-Morales, F., Leuschen, C., Carabajal, C., Paden, J., Wolf, J. A., Garrison, S., & McDaniel, J., (2020). An Improved UWB Microwave Radar for Very Long-Range Measurements of Snow Cover, *IEEE Transactions on Instruments and Measurement*, *69*(10), 7761–7772. https://doi.org/10.1109/TIM.2020.2982813

Rösel, A., Farrell, S. L., Nandan, V., Richter-Menge, J., Spreen, G., Divine, et al. (in press). Implications of surface flooding on airborne thickness measurements of snow on sea ice, *The Cryosphere*, https://doi.org/10.5194/tc-2020-168

Rostosky, P., Spreen, G., Farrell, S. L., Frost, T., Heygster, G., & Melsheimer, C. (2018). Snow depth retrieval on Arctic sea ice from passive microwave radiometers - Improvements and extensions to multiyear ice using lower frequencies. *Journal of Geophysical Research: Oceans*, *123*, 7120–7138. https://doi.org/10.1029/2018JC014028

Rott, H., Abdel Jaber, W., Wuite, J., Scheiblauer, S., Floricioiu, D., Van Wessem, J. M., et al. (2018). Changing pattern of ice flow and mass balance for glaciers discharging into the Larsen A and B embayments, Antarctic Peninsula, 2011 to 2016. *The Cryosphere*, *12*(4), 1273–1291. https://doi.org/10.5194/tc-12-1273-2018

Rutishauser, A., Blankenship, D. D., Sharp, M. J., Skidmore, M. L., Greenbaum, J. S., Grima, C., et al. (2018). Discovery of a hypersaline subglacial lake complex beneath Devon Ice Cap, Canadian Arctic. *Science Advances*, *4*(4). https://doi.org/10.1126/sciadv.aar4353

Sallila, H., Farrell, S. L., McCurry, J., & Rinne, E. (2019). Assessment of contemporary satellite sea ice thickness products for Arctic sea ice. *The Cryosphere*, *13*(4). https://doi.org/10.5194/tc-13-1187-2019

Sasgen, I., Martin-Espanol, A., Horvath, A., Klemann, V., Petrie, E. J., Wouters, B., et al. (2018). Altimetry, gravimetry, GPS and viscoelastic modeling data for the joint inversion for glacial isostatic adjustment in Antarctica (ESA STSE Project REGINA). *Earth System Science Data*, *10*, 493–523. https://doi.org/10.5194/essd-10-493-2018

Schaffer, J., Kanzow, T., Appen, W.-J., Albedyll, L., Arndt, J. E., & Roberts, D. H. (2020). Bathymetry constrains ocean heat supply to Greenland's largest glacier tongue. *Nature Geoscience*, *338*, 1–8. https://doi.org/10.1038/s41561-019-0529-x

Schaffer, N., Copland, L., Zdanowicz, C., Burgess, D. & Nilsson, J. (2020). Revised Estimates of Recent Mass Loss Rates for Penny Ice Cap, Baffin Island, Based on 2005–2014 Elevation Changes Modified for Firn Densification. *Journal of Geophysical Research: Earth Surface*, *124*. https://doi.org/10.1029/JF005440

Schodlok, M. P., Menemenlis, D., Rignot, E., & Studinger, M. (2012). Sensitivity of the ice-shelf/ocean system to the sub-ice-shelf cavity shape measured by NASA IceBridge in Pine Island Glacier, West Antarctica. *Annals of Glaciology*, *53*(60), 156–162. https://doi.org/10.3189/2012AoG60A073

Schröder, L., Horwath, M., Dietrich, R., Helm, V., Van Den Broeke, M. R., & Ligtenberg, S. R. (2019). Four decades of Antarctic surface elevation changes from multi-mission satellite altimetry. *The Cryosphere*, *13*, 427–449. https://doi.org/10.5194/tc-13-427-2019

Schroeder, D. M., Dowdeswell, J. A., Siegert, M. J., Bingham, R. G., Chu, W., MacKie, E. J., et al. (2019). Multidecadal observations of the Antarctic ice sheet from restored analog radar records. *Proceedings of the National Academy of Sciences*, *153*, 201821646–7. https://doi.org/10.1073/pnas.1821646116
Schutz, B. E., Zwally, H. J., Shuman, C. A., Hancock, D., & DiMarzio, J. P. (2005). Overview of the ICESat Mission. *Geophysical Research Letters*, *32*(21), L21S01. https://doi.org/10.1029/2005GL024009
Seroussi, H., Morlighem, M., Rignot, E. J., Larour, E. Y., Aubry, D., Ben Dhia, H., & Kristensen, S. S. (2011). Ice flux divergence anomalies on 79north Glacier, Greenland. *Geophysical Research Letters*, *38*. https://doi.org/10.1029/2011GL047338
Selmes, N., Murray, T., & James, T. D. (2011). Fast draining lakes on the Greenland Ice Sheet. *Geophysical Research Letters*, *38*, L15501. https://doi.org/10.1029/2011GL047872
Shepherd, A., Fricker, H. A. & Farrell, S. L. (2018). Trends and Connections Across the Antarctic Cryosphere. *Nature*, *558*, 223–232. https://doi.org/10.1038/s41586-018-0171-6
Shu, S., Liu, H., Frappart, F., Huang, Y., Wang, S., Hinkel, K. M., et al. (2018). Estimation of snow accumulation over frozen Arctic lakes using repeat ICESat laser altimetry observations – A case study in northern Alaska. *Remote Sensing of the Environment*, *216*, 529–543. https://doi.org/10.1016/j.rse.2018.07.018
Siegfried, M. R., & Fricker, H. A. (2018). Thirteen years of subglacial lake activity in Antarctica from multi-mission satellite altimetry. *Annals of Glaciology*, *59*(76), 42–55. https://doi.org/10.1017/aog.2017.36
Sime, L. C., Karlsson, N. B., Paden, J. D., & Gogineni, S. P. (2014). Isochronous information in a Greenland ice sheet radio echo sounding data set. *Geophysical Research Letters*, *41*. https://doi.org/10.1002/2013GL057928
Slater, T., Shepherd, A., McMillan, M., Muir, A., Gilbert, L., Hogg, A. E., et al. (2018). A new digital elevation model of Antarctica derived from CryoSat-2 altimetry. *The Cryosphere*, *12*, 1551–1562. https://doi.org/10.5194/tc-12-1551-2018
Smith, B.E., Gourmelen, N., Huth, A. & Joughin, I. (2017) Connected subglacial lake drainage beneath Thwaites Glacier, West Antarctica. *The Cryosphere*, *11*, 451–467. https://doi.org/10.5194/tc-11-451-2017
Smith, B., Fricker, H. A., Gardner, A. S., Medley, B., Nilsson, J., Paolo, F. S., et al. (2020). Pervasive ice sheet mass loss reflects competing ocean and atmosphere processes. *Science*, *368*(6496), 1239–1242. https://doi.org/10.1126/science.aaz5845
Soso, M. G., Larsen, C. F., Tober, B. S., Christoffersen, M., Fahnestock, M., Holt, J. W., & Truffer, M. (2021), Quo vadis, Alsek? Climate-driven glacier treat may change the course of a major river outlet in southern Alaska. *Geomorphology*, *384*. https://doi.org/10.1016/j.geomorph.2021.107701
Spikes, V. B., Hamilton, G. S., Arcone, S. A., Kaspari, S., & Mayewski, P. A. (2004). Variability in accumulation rates from GPR profiling on the West Antarctic plateau. *Annals of Glaciology*, *39*, 238–244. https://doi.org/10.3189/172756404781814393
Stammerjohn, S., Massom, R., Rind, D., and Martinson, D. (2012), Regions of rapid sea ice change: An inter-hemispheric seasonal comparison. *Geophysical Research Letters*, *39*, L06501, https://doi.org/10.1029/2012GL050874
Stammerjohn, S., & Maksym, T. (2017). Gaining (and losing) Antarctic sea ice: variability, trends and mechanisms. In *Sea Ice,* 261–289. https://doi.org/10.1002/9781118778371.ch10
Straneo, F., Curry, R. G., Sutherland, D. A., Hamilton, G., Cenedese, C., Våge, K., & Stearns, L. A. (2011). Impact of fjord dynamics and glacial runoff on the circulation near Helheim Glacier. *Nature Geoscience*, *4*(5), 322–327. https://doi.org/10.1038/ngeo1109
Stroeve, J., Barrett, A., Serreze, M., & Schweiger, A. (2014). Using records from submarine, aircraft and satellites to evaluate climate model simulations of Arctic sea ice thickness. *The Cryosphere*, *8*(5). https://doi.org/10.5194/tc-8-1839-2014
Studinger, M., Bell, R. E., & Frearson, N. (2008). Comparison of AIRGrav and GT-1A Airborne Gravimeters for Research Applications. *Geophysics*, *73*. https://doi.org/10.1190/1.2969664

Sutterley, T. C., Velicogna, I., Csatho, B., van den Broeke, M. R., Rezvanbehbahani, S., & Babonis, G. S. (2014a). Evaluating Greenland glacial isostatic adjustment corrections using GRACE, altimetry and surface mass balance data. *Environmental Research Letters*, *9*(1), 014004. https://doi.org/10.1088/1748-9326/9/1/014004

Sutterley, T. C., Velicogna, I., Rignot, E., Mouginot, J., Flament, T., Van Den Broeke, M. R., et al. (2014b). Mass loss of the Amundsen Sea Embayment of West Antarctica from four independent techniques. *Geophysical Research Letters*, *41*, 8421–8428. https://doi.org/10.1002/2014GL061940

Sutterley, T. C., Velicogna, I., Fettweis, X., Rignot, E. J., Noel, B., & van den Broeke, M. R. (2018). Evaluation of Reconstructions of Snow/Ice Melt in Greenland by Regional Atmospheric Climate Models Using Laser Altimetry Data. *Geophysical Research Letters*, *45*, 8324–8333. https://doi.org/10.1029/2018GL078645

Sutterley, T. C., Markus, T., Neumann, T. A., van den Broeke, M. R., van Wessem, J. M., & Ligtenberg, S. R. M. (2019). Antarctic ice shelf thickness change from multimission lidar mapping. *The Cryosphere*, *13*, 1801–1817. https://doi.org/10.5194/tc-13-1801-2019

Tedesco, M., Abdalati, W., & Zwally, H. J. (2007). Persistent surface snowmelt over Antarctica (1987–2006) from 19.35 GHz brightness temperatures. *Geophysical Research Letters*, *34*. https://doi.org/10.1029/2007GL031199

Thomas, R. H. (2001). Program for Arctic Regional Climate Assessment (PARCA): Goals, key findings, and future directions. *Journal of Geophysical Research, 106*(D24), 33691–33705. https://doi.org/10.1029/2001JD900042

Thomas, R., Rignot, E., Casassa, G., Kanagaratnam, P., Acuña, C., Akins, T., et al. (2004). Accelerated sea-level rise from West Antarctica. *Science*, *306*(5694), 255–258. https://doi.org/10.1126/science.1099650

Tilling, R. L., Ridout, A., & Shepherd, A. (2018). Estimating Arctic sea ice thickness and volume using CryoSat-2 radar altimeter data. *Advances in Space Research*, *62*(6), 1203–1225. https://doi.org/10.1016/j.asr.2017.10.051

Tinto, K. J., & Bell, R. E. (2011). Progressive unpinning of Thwaites Glacier from newly identified offshore ridge: Constraints from aerogravity. *Geophysical Research Letters*, *38*, L20503. https://doi.org/10.1029/2011GL049026

Tinto, K. J., Bell, R. E., Cochran, J. R., & Münchow, A. (2015). Bathymetry in Petermann fjord from Operation IceBridge aerogravity. *Earth and Planetary Science Letters*, *422*(C), 58–66. https://doi.org/10.1016/j.epsl.2015.04.009

Truffer, M. (2014). Ice Thickness Measurements on the Harding Icefield, Kenai Peninsula, Alaska. *Natural Resource Data Series*, NPS/KEFJ/NRDS—2014/655, National Park Service, Fort Collins, Colorado

Truffer, M., Holt, J., Larsen, C., & Fahnestock, M. (2016). High resolution bed topography for the Malaspina Glacier lobe. *AGU Fall Meeting 2016*, C13C-0836

Trusel, L. D., Frey, K. E., Das, S. B., Munneke, P. K., & Van Den Broeke, M. R. (2013). Satellite-based estimates of Antarctic surface meltwater fluxes. *Geophysical Research Letters*, *40*, 6148–6153. https://doi.org/10.1002/2013GL058138

Trüssel, B. L., Motyka, R. J., Truffer, M., & Larsen, C. F. (2017). Rapid thinning of lake-calving Yakutat Glacier and the collapse of the Yakutat Icefield, southeast Alaska, USA. *Journal of Glaciology*, *59*(213), 149–161. https://doi.org/10.3189/2013J0G12J081

Tsamados, M., Feltham, D. L., Schroeder, D., Flocco, D., Farrell, S. L., Kurtz, N., et al. (2014). Impact of variable atmospheric and oceanic form drag on simulations of Arctic sea ice. *Journal of Physical Oceanography*, *44*, 1329–1353. https://doi.org/10.1175/JPO-D-13-0215.1

van de Berg, W. J., & Medley, B. (2016). Brief Communication: Upper-air relaxation in RACMO2 significantly improves modelled interannual surface mass balance variability in Antarctica, *The Cryosphere*, *10*, 459–463. https://doi.org/10.5194/tc-10-459-2016 van Wessem, J. M., Jan Van De Berg, W., Noël, B. P., Van Meijgaard, E., Amory, C., Birnbaum, G., et al. (2018). Modelling the climate and surface mass balance of polar ice sheets using RACMO2: Part 2: Antarctica (1979-2016). *The Cryosphere*, *12*(4), 1479–1498. https://doi.org/10.5194/tc-12-1479-2018

Van Wychen, W., Burgess, D. O., Gray, L., Copland, L., Sharp, M., Dowdeswell, J. A. & Benham, T. J. (2013). Glacier velocities and dynamic ice discharge from the Queen Elizabeth Islands, Nunavut, Canada. *Geophysical Research Letters*, *41*, 484–490. https://doi.org/10.1002/2013GL058558

Van Wychen, W., Davis, J., Burgess, D. O., Copland, L., Gray, L., Sharp, M., & Mortimer, C. (2016). Characterizing interannual variability of glacier dynamics and dynamic discharge (1999–2015) for the ice masses of Ellesmere and Axel Heiberg Islands, Nunavut, Canada. *Journal of Geophysical Research: Earth Surface*, *121*, 39–63. https://doi.org/10.1002/2015JF003708

Van Wychen, W., Burgess, D., Kochtitzky, W., Nikolic, N., Copland, L., & Gray, L. (2020). RADARSAT-2 derived glacier velocities and dynamic discharge estimates for the Canadian High Arctic: 2015–2020. *Canadian Journal of Remote Sensing*, *46*(6). https://doi.org/10.1080/07038992.2020.1859359

Velicogna, I., & Wahr, J. (2006). Acceleration of Greenland ice mass loss in spring 2004. *Nature*, *443*(7109), 329–331. https://doi.org/10.1038/nature05168

Wadhams, P., & Horne, R. J. (1980). An analysis of ice profiles obtained by submarine sonar in the Beaufort Sea. *Journal of Glaciology*, *25*, 401–424, https://doi.org/10.3189/S0022143000015264

Walker, C. C., & Gardner, A. S. (2017). Rapid drawdown of Antarctica's Wordie Ice Shelf glaciers in response to ENSO/Southern Annular Mode-driven warming in the Southern Ocean. *Earth and Planetary Science Letters*, *476*, 100–110. https://doi.org/10.1016/j.epsl.2017.08.005

Wang, X., Xie, H., Ke, Y., Ackley, S. F., & Liu, L. (2013). A method to automatically determine sea level for referencing snow freeboards and computing sea ice thicknesses from NASA IceBridge airborne LIDAR. *Remote Sensing of the Environment*, *131*, 160–172. https://doi.org/10.1016/j.rse.2012.12.022

Wang, X., Guan, F., Liu, J., Xie, H., & Ackley, S. (2016). An improved approach of total freeboard retrieval with IceBridge Airborne Topographic Mapper (ATM) elevation and Digital Mapping System (DMS) images. *Remote Sensing of the Environment*, *184*, 582–594. https://doi.org/10.1016/j.rse.2016.08.002

Warren, S. G., Rigor, I. G., Untersteiner, N., Radionov, V. F., Bryazgin, N. N., Aleksandrov, Y. I., & Colony, R. (1999). Snow Depth on Arctic Sea Ice. *Journal of Climate*, *12*(6), 1814–1829. https://doi.org/10.1175/1520-0442(1999)012

Webb, C. E., Zwally, H. J. & Abdalati, W. (2013). The Ice, Cloud, and land Elevation Satellite (ICESat) Summary Mission Timeline and Performance Relative to Pre-Launch Mission Success Criteria. *NASA Technical Report*, 20130014062, https://ntrs.nasa.gov/search.jsp?R=20130014062

Webster, M. A., Rigor, I. G., Nghiem, S. V., Kurtz, N. T., Farrell, S. L., Perovich, D. K., & Sturm, M. (2014). Interdecadal changes in snow depth on Arctic sea ice. *Journal of Geophysical Research: Oceans*, *119*(8), 5395–5406. https://doi.org/10.1002/2014JC009985

Webster, M. A., Rigor, I. G., Perovich, D. K., Richter-Menge, J. A., Polashenski, C. M., & Light, B. (2015). Seasonal evolution of melt ponds on Arctic sea ice. *Journal of Geophysical Research: Oceans*, *120*(9), 5968–5982. https://doi.org/10.1002/2015JC011030

Webster, M. A., Gerland, S., Holland, M., Hunke, E., Kwok, R., Lecomte, O., et all. (2018). Snow in the changing sea-ice systems. *Nature Climate Change*, *8*, 946–953. https://doi.org/10.1038/s41558-018-0286-7

Wei, W., Blankenship, D. D., Greenbaum, J. S., Gourmelen, N., Dow, C. F., Richter, T. G., et al. (2020). Getz Ice Shelf melt enhanced by freshwater discharge from beneath the West Antarctic Ice Sheet. *The Cryosphere*, *14*, 1399–1408. https://doi.org/10.5194/tc-14-1399-2020.

Whillans, I. M. (1976). Radio-echo layers and the recent stability of the West Antarctic ice sheet. *Nature*, *264*(5582), 152–155. https://doi.org/10.1038/264152a0

Willis, M. J., Herried, B. G., Bevis, M. G., & Bell, R. E. (2015). Recharge of a subglacial lake by surface meltwater in northeast Greenland. *Nature*, *518*, 223–227. https://doi.org/10.1038/nature14116

Wingham, D. J., Ridout, A. J., Scharroo, R., Arthern, R. J., & Shum, C. K. (1998). Antarctic elevation change from 1992 to 1996. *Science*, *282*(5388), 456–458. https://doi.org/10.1126/science.282.5388.456

Winter, A., Steinhage, D., Arnold, E., Blankenship, D. D., Cavitte, M. G. P., Corr, H. F. J., et al. (2017). Comparison of measurements from different radio-echo sounding systems and synchronization with the ice core at Dome C, Antarctica. *The Cryosphere*, *11*(1), 653–668. https://doi.org/10.5194/tc-11-653-2017

Wolovick, M. J., Creyts, T. T., Buck, W. R., & Bell, R. E. (2014). Traveling slippery patches produce thickness-scale folds in ice sheets. *Geophysical Research Letters*, *41*(24), 8895–8901. https://doi.org/10.1002/2014GL062248

Wright, A. P., Young, D. A., Bamber, J. L., Dowdeswell, J. A., Payne, A. J., Blankenship, D. D., & Siegert, M. J. (2014). Subglacial hydrological connectivity within the Byrd Glacier catchment, East Antarctica. *Journal of Glaciology*, *60*(220), 345–352. https://doi.org/10.3189/2014JoG13J014

Wright, N. C., & Polashenski, C. M. (2018). Open-source algorithm for detecting sea ice surface features in high-resolution optical imagery. *The Cryosphere*, *12*, 1307–1329. https://doi.org/10.5194/tc-12-1307-2018

Yan, J.-B., Gogineni, S., Rodriguez-Morales, F., Gomez-Garcia, D., Paden, J., Li, J., et al. (2017). Airborne measurements of snow thickness using ultrawide-band frequency-modulated-continuous-wave radars. *IEEE Geoscience and Remote Sensing Magazine*, *5*(2), 57-76. https://doi.org/10.1109/MGRS.2017.2663325

Yan, J.-B., Li, L., Nunn, J. A., Dahl-Jensen, D., O'Neill, C., Taylor, R. A., et al. (2020). Multiangle, frequency and polarization radar measurements of ice sheets. *IEEE Journal of Selected Topics in Applied Earth Observations and Remote Sensing*, *13*, 2070–2080. https://doi.org/10.1109/JSTARS.2020.2991682

Yardim, C., Johnson, J. T., Jezek, K. C., Andrews, M. J., Durand, M., Duan, Y., et al. (2021). Greenland Ice Sheet subsurface temperature estimation using ultrawideband microwave radiometry. *IEEE Transactions on Geoscience and Remote Sensing*. https://doi.org/10.1109/TGRS.2020.3043954

Yi, D., Harbeck, J. P., Manizade, S. S., Kurtz, N. T., Studinger, M., & Hofton, M. (2014). Arctic sea ice freeboard retrieval with waveform characteristics for NASA's Airborne Topographic Mapper (ATM) and Land, Vegetation, and Ice Sensor (LVIS). *IEEE Transactions on Geoscience and Remote Sensing*, *53*(3), 1403-1410. https://doi.org/10.1109/TGRS.2014.2339737

Yi, D., Kurtz, N., Harbeck, J., Kwok, R., Hendricks, S. & Ricker, R. (2019). Comparing Coincident Elevation and Freeboard From IceBridge and Five Different CryoSat-2 Retrackers. *IEEE Transactions on Geoscience and Remote Sensing*, *57*(2), 1219–1229. https://doi.org/10.1109/TGRS.2018.2865257

Young, D. A., Kempf, S. D., Blankenship, D. D., Holt, J. W., & Morse, D. L. (2008). New airborne laser altimetry over the Thwaites Glacier Catchment, West Antarctica. *Geochemistry, Geophysics, Geosystems*, *9*(6), Q06006. https://doi.org/10.1029/2007GC001935

Young, D. A., Wright, A. P., Roberts, J. L., Warner, R. C., Young, N. W., Greenbaum, J. S., et al. (2011). A dynamic early East Antarctic Ice Sheet suggested by ice covered fjord landscapes. *Nature*, *474*, 72–75. https://doi.org/10.1038/nature10114

Young, D. A., Lindzey, L. E., Blankenship, D. D., Greenbaum, J. S., de Gorordo, A. G., Kempf, et al. (2015). Land-ice elevation changes from photon counting swath altimetry: First applications over the Antarctic ice sheet. *Journal of Glaciology*, *61*(225), 17–28. https://doi.org/10.3189/2015JoG14J048

Young, D. A., Schroeder, D. M., Blankenship, D. D., Kempf, S. D., & Quartini, E. (2016). The distribution of basal water between Antarctic subglacial lakes from radar sounding. *Philosophical Transactions of the Royal Society A: Mathematical, Physical and Engineering Sciences*, *374*(2059), 20140297–21. https://doi.org/10.1098/rsta.2014.0297

Appendix A: OIB programmatic goals, science goals and questions

Table A1: Programmatic goals

OIB programmatic goals.

#	Programmatic goal
P1	Make airborne altimetry measurements over the ice sheets and sea ice to extend and improve the record of observations begun by ICESat.
P2	Link the measurements made by historical airborne laser altimeters, ICESat, ICESat-2 and CryoSat-2 to allow accurate inter-comparison and production of a long-term, ice altimetry record.
P3	Monitor key, rapidly changing areas of ice in the Arctic and Antarctic to maintain a long-term observation record.
P4	Provide key observational data to improve our understanding of ice dynamics, and better constrain predictive models of sea level rise and sea ice cover conditions.

Table A2: Science goals

OIB science goals. Parentheses refer to programmatic goals (Table A1).

#	Science goal
G1	Document volume changes over the aircraft-accessible portions of the Greenland and Antarctic ice sheets during the period between the ICESat and ICESat-2 missions. A particular focus will be to document rapid changes. OIB will answer: How have the ice-sheet volumes within areas accessible by aircraft changed during this period? (P1,P2)
G2	Document glacier and ice-shelf thickness, ice-shelf bathymetry, snow accumulation-rate variability and other geophysical properties to better interpret volume changes measured with laser altimetry and to enable more realistic simulations of ice-sheet flow and mass balance with numerical models. OIB will help answer: How are the ice sheets likely to change in the future? (P3,P4)
G3	Document spatial and interannual changes in the mean sea ice thickness and the thickness distribution in the Arctic and Southern Oceans in the period between ICESat and ICESat-2, in support of climatological analyses and assessments.
G4	Improve sea ice thickness retrieval algorithms by advancing technologies for measuring sea ice surface elevation, freeboard and snow thickness distributions on sea ice in the Arctic and Southern Oceans.

Table A3: Science questions

OIB science questions. Parentheses refer to science goals (Table A2).

#	Science question
Land ice	
IQ1	Where are glaciers continuing to thin and where are they thickening? (G1)
IQ2	What are the major forces and mechanisms causing the ice sheets to lose mass and change velocity, and how are these processes changing over time? (G2) • How do ice sheet/glacier surface topography, bed topography, ice shelves/tongues, and grounding-line configurations affect ice dynamics? • How far inland are the effects of coastal thinning transmitted and by what physical processes? • How far downstream do changing processes near the ice divide affect ice-sheet evolution?

IQ3	How do the oceans, sea ice, and ice sheets interact, and how do these interactions ultimately influence ice-sheet behavior? (G2) ● How does the bathymetry beneath Arctic fjords and Antarctic ice shelves influence ocean/ice sheet interactions and ice-sheet/glacier flow dynamics?
IQ4	What are yearly snow accumulation/melt rates over the ice sheets? (G1) ● How do changing accumulation rates (and hence near surface densities and firn structure) impact altimetry measurements? ● What are the surface-melt flow patterns and how do they change with time?
Sea ice	
SQ1	How are the physical characteristics of Arctic and Antarctic sea ice changing? (G3)
SQ2	What level of accuracy in ice thickness observations is desirable for climate or operational forecasts? (G3)
SQ3	What is the optimal temporal and spatial sampling strategy for extensive airborne observations of Arctic and Antarctic sea ice? (G4) ● How can sea ice data from OIB airborne platforms be most effectively combined with data from *in situ*, submarine and satellite platforms? ● Are there sea ice physical characteristics or locations that should be specifically monitored to best aid in the future observation of ice thickness with ICESat-2?
SQ4	What is the optimal instrument configuration to measure the following sea ice properties remotely: sea ice freeboard, snow thickness, sea ice thickness, surface roughness and sea ice/lead distributions? (G4)
SQ5	What is the relationship between sea ice surface roughness and the thickness of any overlying snow? (G4)